Towards quantum computing using nitrogen vacancy centers: optimising photon collection

Zhin Fong Mai

A thesis presented for the degree of

Doctor of Philosophy

Department of Materials

University of Oxford

Mansfield college

Supervisor: Prof. Jason Smith

October 2024

1 Abstract

Nitrogen vacancy centres in diamond have shown strong potential for use as qubits in quantum computing. However, nitrogen vacancy centres have a low percentage of overall emission emitted through the Zero Phonon Line (ZPL). In addition, the fabrication of NV centres with controlled positioning is limited. This thesis presents the ZPL linewidth characterisation of NV centres fabricated using laser writing and laser diffusion. Only one out of the six NV centres characterised showed a <100 MHz average single scan linewidth, which suggests that the laser diffusion process needs to improved. The low ZPL emission can be enhanced by cavity coupling to Fabry-Pérot microcavities. Fabry-Pérot microcavities are susceptible to vibrations, which will decouple the cavity from the NV centre and reduce the photon enhancement. A cavity stabilisation system based on cavity fringe stabilisation is implemented, and the results of the stability are presented. The Fabry-Pérot microcavity can be stabilised with 0.13 nm using fringe stabilisation. High collection efficiency of the emission is also desired for maximising the entanglement rate and is reduced by optical aberrations. For NV centres in bulk diamond, using Solid Immersion Lenses (SILs) removes the spherical aberration that is introduced when collecting NV emission through a planar interface. This thesis presents the results of modelling the aberrations for NV centres cavity coupled to a Fabry-Pérot microcavity and for hemispherical SILs on diamond. The wavefronts of the aberrations introduced by the planar mirror of the microcavity and the aberrations introduced by the positioning error of the SIL are modelled numerically. A deformable mirror is implemented into a confocal microscope to monitor the aberrations of the photonic devices and the results are compared with the numerical model. For Fabry-Pérot microcavities, the intensity loss caused by the aberrations introduced by the planar mirror was predicted to be less than 10 % due to the thin mirror substrate and low numerical aperture of the cavity mode. This prediction was consistent with the experimental results where an effective 3 % increase in light collection was observed with aberration correction. For the SILs, the model predicts that the collection efficiency is more sensitive to the lateral positioning of the SIL relative to the NV centre than the axial positioning error.

2 Acknowledgements

This thesis would not have been possible without the support of the Photonic Nanomaterials Group. In particular: Sam Johnson, Shannon Nicley, Laiyi Weng, Shazeaa Ishmael, Jiangrui Qian, Yumeng Yin, Cassie Song, Brandon Severin and Shamil Mirkhanov, who have all been great to work with and learn from. Additionally, I would like to express my gratitude to Andrew Kirkpatrick. I thank him for being such a great friend to me and for making me a better person. There is also Amit Dhawan, who has been there as a mentor and friend guiding me through some of the lows of research and showing me the standard of optics. In addition, Xingrui Cheng and Gareth Jones, for helping me with my final experiments.

There are members of the department who have been essential to my success: Paul Warren, Ashley Brown, Mike Stanley, Francis Dunleavey and Greg Cook who have helped setup equipment in the labs. I would like to thank Chris Salamone and Gail Leckie from Mansfield College for their support during some difficult times. I would like to thank Adrian Taylor for helping me with funding for my final months of research. I would like to thank Patrick Salter for providing me with advice on my theory and experiments. I would also like to thank our collaborators at Warwick: Gavin Morley, Collin Stephen, and Joe Gore for annealing the samples. I thank EPSRC for funding this project. I would like to express my appreciation to my supervisor, Jason Smith, for his ongoing support, patience, and for maintaining a positive outlook when I was struggling.

I would like to thank my friends Shengda Pu and Juan Velásquez for joining me outside the lab. Finally, I would like to thank my parents, Michael and Mandy, for their support throughout my life, as well as the rest of my family. I thank you all for being a part of my life.

Contents

1 **Abstract** i

2 **Acknowledgements** ii

3 **Abbreviations** xv

4 **Introduction and Literature review** 1

- 4.1 Introduction . . . 1
- 4.2 Measurement-based quantum computing . . . 3
- 4.3 Diamond Nitrogen Vacancy (NV) centre . . . 6
- 4.4 Diamond processing . . . 10
- 4.5 NV fabrication . . . 11
- 4.6 Optical microcavities . . . 12
- 4.7 Fabry-Pérot microcavity . . . 14
- 4.8 Cavity locking . . . 16
- 4.9 Resonance fluorescence . . . 17
- 4.10 Solid Immersion Lenses . . . 18
- 4.11 Conclusion . . . 20

5 **Theoretical Background** 23

- 5.1 Introduction . . . 23
- 5.2 Optical Resonators . . . 23
- 5.3 Gaussian Beam Optics . . . 26
- 5.4 Cavity Quantum Electrodynamics . . . 29
- 5.5 Free space spontaneous emission . . . 32
- 5.6 Cavity coupled emission . . . 33
- 5.7 Distributed Bragg Reflectors . . . 34

5.8 Aberration Theory 36
  5.8.1 Introduction 36
  5.8.2 Zernike Polynomials 36
  5.8.3 Aberration function focusing through a planar interface 39

6 Experimental Methods **42**
6.1 Adaptive Optics 42
6.2 Laser Scanning Confocal Microscopy 42
6.3 Cavity Coupling Assembly 47
6.4 Cavity Fringe Stabilisation 49
6.5 Power Saturation measurement 51
6.6 Hanbury Brown Twiss measurement 51
6.7 Optically Detected Magnetic Resonance 53
6.8 Photoluminescence Excitation Spectroscopy 54

7 Photoluminescence spectroscopy of the MHz diffused NV centres **58**
7.1 Introduction 58
7.2 Results 59
7.3 Discussion 63
7.4 Conclusion 66

8 Cavity Locking **67**
8.1 Introduction 67
8.2 Cavity locking performance 67
8.3 Cavity coupled continuous wave ODMR 67
8.4 Discussion 71
8.5 Conclusion 73

9 Aberration corrected cavity coupling 74

- 9.1 Introduction 74
- 9.2 Modelling the spherical aberration within the microcavity 75
  - 9.2.1 Introduction 75
  - 9.2.2 Cavity mode formation and emission 75
  - 9.2.3 Spherical aberration through the mirror substrate and collection 78
- 9.3 Microcavity aberration 78
  - 9.3.1 Power saturation measurement 78
  - 9.3.2 Cavity multi mode measurement 81
  - 9.3.3 Effects of aberration correction on higher order modes 88
  - 9.3.4 Effects of aberration correction on rotated cavity modes 91
- 9.4 Discussion 95
- 9.5 Conclusion 98

10 Aberrations in solid immersion lenses 99

- 10.1 Introduction 99
- 10.2 Aberrations from axially displaced emitters 99
- 10.3 Aberrations from laterally displaced emitters 104
- 10.4 Monolithic SIL 109
- 10.5 Discussion 110
- 10.6 Conclusion 114

11 Conclusions and Outlook 115

- 11.1 Conclusion 115
- 11.2 Future Work 117

12 References 119

List of Figures

1 Graph describing the number of computational operations required for prime number factorisation using a classical algorithm and Shor's algorithm. Figure from source [5] 2

2 Schematic of the measurement-based entanglement process. Reproduced from source [14]. The beamsplitter has the effect of splitting the photons into two components, where one component is transmitted through the beamsplitter towards one photodetector and the other is reflected towards the other photodetector. When the photons arrive from both NV centres simultaneously, they are split by the beamsplitter and split photons from one NV centre interact with the split photons from the other. The photons interfere constructively/destructively so only one photon arrives at either photon detector. When this occurs, the photons are entangled and since the fluorescence is spin state dependent, the spins are also entangled. 4

3 Schematic structure of the NV centre in a diamond lattice (a), the electronic structure of the NV$^-$(b) and the optical spectrum of NV$^-$ at room temperature and 4 K. Direct excitation and radiative transitions are shown by the solid vertical double arrows and the non-radiative transitions are shown by the dashed arrows. The electronic structure is reproduced from source [24]. 7

4 Plot of relaxation(T$_1$) and decoherence(T$_2$) times vs temperature for different spin qubit systems. Image reproduced from source [42]. 9

5 (a)Graphic of a planar-concave Fabry-Pérot microcavity with Bragg mirrors. (b) Optical spectrum of an NV centre before and after cavity coupling. Spectrum reproduced from source [72]. 15

6 Schematics of the emission path of the rays through a Planar interface, Hemispherical SIL and Aplanatic SIL. The dashed line cone represents the region of rays that is collected by the objective lens. 18

7 Schematic of a planar-planar cavity with mirrors of reflectivity R_1 and R_2 and a standing wave with $q = 2$. 24

8 Cavity transmission spectrum for a 1D cavity in terms of numbers of wavelengths q. The reflectivity changes the transmission linewidth, $\delta\lambda$ and the minimum transmission of the cavity. 25

9 Intensity and phase profiles of the Hermite-Gaussian modes up to l+m = 3. The profiles are labelled by the transverse mode indices in lm format. 30

10 Optical spectrum of an NV centre coupled to a microcavity supporting multiple cavity modes. The broad emission of the NV PSB acts like a broadband photon source that is filtered by the higher-order cavity modes. The inset images show the possible Hermite-Gaussian mode profiles that can be associated with each peak for a constant longitudinal mode index q. For higher values of l+m, the peak may consist of multiple higher-order modes. 31

11 Point spread function of focused laser beam under the affect of each aberration listed in table 1 along with the phase profile of the aberration in the inset. The amplitude of aberration applied is $+\lambda/4$ waves and the plots are normalised to the maximum intensity of a diffraction-limited spot. 38

12 Schematic of ray path change when focusing with only the focusing medium n_1 against focusing in a different medium n_2. d is the length from the refractive mismatch interface to the point of focus. 39

13 Normalised intensity profile of collected light, when collecting light from an emitter in the diamond. For the calculation, the numerical aperture used is $NA = 0.82$, the refractive index used are $n_1 = 1$ and $n_2 = 2.4$ and the wavelength used is $\lambda = 640\ nm$ 41

14 (a) Schematic of the deformable mirror, (b) optical image of the Boston Micromachines Multi-3.5-DM and (c) graphic of the actuator grid of the DM. Schematic reproduced from source [114]. Dark pixels represent inactive actuators and the circle represents the active area being used. The red circle is the effective back aperture of the objective lens that is exposed on the DM. The effective diameter is 3.76 mm. 43

15 Optical layout of the confocal imaging system using a Deformable Mirror. Figure produced by Amit Dhawan. 45

16 Optical images of the FSM(a) and the DM conjugate to the FSM (b). Some of the features on the FSM circled in red can be seen when imaging the DM if the FSM and the DM are conjugate to each other and both are illuminated. . . 46

17 CAD schematic of the cavity coupling assembly with the attocube piezo labelled and the objective lens. Insert image of zoomed-in area of the mirror cavity region and an image of the concave mirror array plinth. The assembly allows for remote in situ alignment of the concave mirror for cavity coupling and tuning. 49

18 a) Schematic of the the fringe formation in the cavity. The wedge angle in the cavity produces interference fringes in transmission when the cavity is illuminated. b) Cavity image showing 2 fringes formed from the wedge interference. The red arrow shows the direction of fringe movement when the cavity length changes. 50

19 Schematic of the HBT measurement used. The collected light is split by a fibre beam splitter and coupled to two single-photon counting modules. The photon detection is then logged by a time tagger, which will measure and log the time difference between detection from both detectors. 52

20 Schematic of the PCB trace loop antenna with the planar mirror on top and a zoomed in image of the patterned grid on the mirror The PCB is made with Rogers 4350B and interfaced with a 50 Ω SMP PCB connector. The loop was designed with a 1.6 mm diameter and 0.5 mm loop thickness. 54

21 a) Electrical schematic of the ODMR system. All connections between each device were made using SMA cables except for the semi-rigid cable (Thorlabs SMGF6). b) Schematic of the microcavity assembly with the loop antenna. . . 55

22 Schematic of the photoluminescence spectroscopy setup. The thin lines represent wired connections and the thick coloured lines represent optical paths. The optical paths going towards the confocal microscope are fibre-coupled to deliver the optics through optical fibres. The 637 nm optics, SPAD collection optics and hardware control/data acquisition programming were developed by me. The 532 nm laser optics was aligned by Gareth Jones. Some of the graphics used are from the ComponentLibrary by Alexander Franzen. 57

23 Diagram of NV fabrication procedures using ion/electron irradiation with thermal anneal and laser writing and diffusion. The laser writing process for vacancy generation involves applying a single pulse to generate the vacancy and the diffusion process involves applying multiple laser pulses with a lower power than the vacancy generation pulse to diffuse the vacancy to a local nitrogen atom. . 58

24 Confocal images of laser-diffused NVs in sites A and B. The NVs that showed peaks in the PLE scans are labelled. 59

25 PLE single scans of NV ZPL for B3 (a) and B6 (b) respectively with Voigt functions fitted to the peaks, and the histogram (c) of the average ZPL linewidth from the single scans performed on each NV centre. The objective power of the 637 nm tunable laser used for the scans was 40 nW and 50 nW respectively. . 61

26 Determination of the total linewidth of the ZPL for the B3 NV centre. The single sweep scans that show peaks (a) are added together (b) and the overall peak is fitted to extract the total linewidth. The total linewidths of each NV characterised are presented in the histogram (c). 62

27 Power saturation measurement of the B3 ZPL. 63

28 Empirical cumulative distribution function of the NV ZPL single scan linewidths of the MHz laser written and diffused NV centres. 64

29 (a) Rate of a peak presence per sweep for different objective powers. (b) PLE single line scan showing photo-ionisation occurring during the sweep. This leads to a peak fit that underestimates the actual linewidth. Sweep was performed with 500 nW objective power. 66

30 Optical spectrum of the cavity modes taken 10 s and 10 min after the start of the cavity locking. The modes are formed with a 4 µm RoC concave mirror. The inset plot shows the longitudinal mode at around 669 nm. 68

31 Plots of cavity drift against time for varying microwave power (a), microwave frequency (b) and microwave sweep rate (c). The dynamic frequency sweep range is 2.6 GHz-3.0 GHz. Each plot contains three subplots representing the start of the microwave delivery, applying the cavity locking after 5 minutes and removing the microwaves and locking to the cavity. 69

32 Maximum displacement introduced to the cavity by delivering continuous microwaves at different frequencies 70

33 Screenshot showing a plot of the CW ODMR sweep for a cavity-coupled 100 nm Nanodiamond containing 1000s NV centres (FND biotech brFND-100). The plot was averaged over 100 scans and was taken using Qudi.[126] The position and FWHM of the signal are shown in the inset. The ODMR linewidth is expected to be broader due to the ensemble of NVs present and its linewidth is consistent with those reported in the literature.[125] 71

34 Diagram of how collection efficiency is determined. The pinhole diameter is set to match the diameter of the diffraction-limited spot. 74

35 Schematic description to modelling the effect of aberrations to the cavity emission 75

36 Diagram of the light collection by the objective lens from a point source emitter and a cavity mode. 76

37 FDTD simulation of the normalised far field intensity profile of the cavity mode emission through the planar mirror direction for hemispherical cavities with different radii of curvature. The cavity length was set to $q = 3$ and DBR mirror reflectivity $R_1 = 99.8\%, R_2 = 99.99\%$. 77

38 Normalised collected intensity profile against the numerical aperture of the cavity mode emission with spherical aberration introduced by the mirror substrate. Profiles are evaluated at $\lambda = 637\ nm$ and with different substrate thicknesses with $n_2 = 1.5$. The shaded region covers the NA of the cavities available for this study. This model was scripted in MATLAB by me. 79

39 Power saturation and spectrum of a $5\mu m$ RoC hemispherical cavity before and after applying aberration correction. Power saturation plots are fitted using Equation 6.2 80

40 Spectrum of a multi-mode $25\ \mu m$ RoC hemispherical microcavity with a longitudinal mode index q=18 and primarily coupled to the TEM$_{00}$ mode. The *(l+m)*$_{even}$ modes are coupled stronger than the *(l+m)*$_{odd}$ modes. The spectra were taken for 30 s at varying amplitudes of primary spherical aberration applied to the deformable mirror. The amplitude of primary spherical aberration was ± 0.4 radians from the reference amplitude determined by the open-loop aberration correction. The total transverse mode index of the peaks are labelled above the peak. 81

41 Amplitudes of the Zernike aberrations fitted to the TEM$_{lm}$ wavefronts. The plots are grouped by the sum of their transverse mode index (l+m). 83

42 Bar plots of the intensity of the cavity mode peaks under the effects of spherical aberration, astigmatism and coma of different amplitudes. The cavity is coupled using a $25\ \mu m$ RoC concave mirror. Peak intensities are normalised to the midpoint amplitude. 84

43 Bar charts of the relative peak intensities of the cavity modes for different amplitudes of the Zernike polynomial applied to the deformable mirror for the $25\ \mu m$ multimode cavity, which is strongly coupled to a TEM_{01} mode. Peak intensities are normalised to the intensity obtained using the reference amplitude. 86

44 Intensity profiles of the TEM_{01} mode under the effects of aberrations applied to the wavefront. The theoretical applied aberration profiles are shown in the inset of each Figure. For comparison, the phase profile for the TEM_{01} mode is shown in the inset of the figures for the central column. 89

45 Bar plots of the normalised intensity of the upper leftmost brightest lobe circled of the cavity modes under the effects of aberrations with different amplitudes. The lobe intensity that is collected by the pinhole is circled in red. 90

46 Bar plots of the collected intensity of the cavity modes under the effects of aberrations with different amplitudes when the light is collected in the centre of the cavity mode. 92

47 Bar plots of the normalised intensity of the lobe circled in red of the cavity modes rotated 45°clockwise under the effects of aberrations with different amplitudes. 93

48 Bar plots of the normalised intensity collected in the centre of the cavity modes rotated 45°clockwise under the effects of aberrations with different amplitudes. 94

49 Rings of the apertures exposed on the deformable mirror for different values of NA. The aperture of maximum NA is $\text{NA}_{obj} = 0.82$ is shown by the green ring and the red rings show the possible apertures of the cavity modes. 97

50 Schematic of the confocal system collecting light from a NV centre under a SIL. 99

51 Ray (a) and Geometric (b) schematics of the ray paths focusing into a SIL at the point D along the optical axis z. The ray paths l_1 and l_2 represent the rays focusing in free space and in the SIL respectively. The refractive index of the SIL is n_2 and a radius r. 101

52 Graph of amplitudes of the rotationally symmetric aberrations for emitters displaced from the centre of the SIL (d=0) to the surface (d=r). Amplitudes are calculated for a $5\mu m$ diamond SIL ($n_2 = 2.4$) focused in free space ($n_1 = 1$) with $\lambda = 640nm$ 102

53 Intensity profile for the collected intensity from the SIL focused at a point source axially displaced from the centre of the SIL. The losses associated with defocus aberration have been removed. 103

54 Schematics for determining the aberration function for (a,c) axially or (b,d) laterally displaced emitters on the SIL in 2D (a,b) and 3D (c,d). The contour lines represent the phase differences for the rays towards the emitter for different angles relative to the optical axis. The dashed lines represent the aberrated and non aberrated rays to the emitter for a ray 40° from the optical axis. The shaded area represents the cone of rays that are used to determine the aberration profile. 105

55 Schematic of a segment of a SIL showing the maximum possible limit of a ray being refracted from the point source. Any ray angle beyond this limit will not be collected by the numerical aperture shown as shaded within the NA cone. . . 106

56 Plots of the components of the radially symmetric (a) and non radially symmetric (b) Zernike polynomials for the aberration wavefront for emitters displaced laterally across the SIL. The SIL modelled was a $5\mu m$ radius diamond ($n_2 = 2.4$) SIL focused through air ($n_1 = 1$) using a NA=0.82 objective lens. 108

57 Intensity plots of the modelled intensity vs displacement from the centre of the SIL described in polar coordinates (d, η). Each plot represents a different angle of displacement relative to the optical axis where $\eta = 90^\circ$ represents lateral displacement and $\eta = 0^\circ$ represents axial displacement. The schematic shown in the graph shows the direction of the emitter displacement relative to the optical axis. 109

58 Confocal xy (a) and xz (b) scans of the NV centre in the monolithic SIL site B2, along with a SEM image (c) and HBT characterisation of the NV under the SIL (d). The xy scan was taken using a beam scanning system with a NA=0.9 air objective lens and the xz scan was taken with a stage scanning system using a NA=1.25 oil objective lens. The SEM image was taken by Shazeaa Ishmael. The HBT plot was fitted using Equation 6.5. 111

59 Plots amplitude of the radially (a) and non-radially (b) symmetric Zernike polynomials fitted to the aberrated wavefront of the SIL for emitters displaced at a length d from the centre of the SIL and at a 38°angle relative to the optical axis ($\eta = 38^\circ$). The dashed vertical line indicates the displacement of the emitter in the monolithic SIL. 112

60 Aberration amplitude sweep on the SIL sample. 113

61 Schematic of a hybrid cavity. This cavity consists of a diamond membrane with laser-written NV centres being placed on a planar DBR mirror, a micro-SIL with a DBR coating to form the cavity and gold striplines to address spin control and Stark shifting of the NV ZPL. 118

3 Abbreviations

AR **A**nti **R**eflection

CVD **C**hemical **V**apour **D**eposition

CW **C**ontinous **W**ave

DM **D**eformable **M**irror

FSM **F**ast **S**teering **M**irror

FDTD **F**inite **D**ifference **T**ime **D**omain

FIB **F**ocus **I**on **B**eam

FWHM **F**ull **W**idth **H**alf **M**aximum

HBT **H**anbury **B**rown and **T**wiss

HPHT **H**igh **P**ressure **H**igh **T**emperature

MW **M**icro**W**ave

NV **N**itrogen **V**acancy center

NA **N**umerical **A**perture

ODMR **O**ptically **D**etected **M**agnetic **R**esonance

PSB **P**honon **S**ide **B**and

PLE **P**hotoluminescence **E**xcitation spectroscopy

PDH **P**ound **D**rever **H**all

RIE **R**eactive **I**on **E**tching

SPAD **S**ingle **P**hoton **A**valanche **D**etector

SIL **S**olid **I**mmersion **L**ens

ZPL **Z**ero **P**honon **L**ine

4 Introduction and Literature review

4.1 Introduction

Moore's law states that the number of transistors in an integrated circuit will double roughly every two years.[1] However, the transistor sizes are reaching the nm scale converging to the size of an atom. With the increasing number of electronic devices and Moore's law reaching its limit, the total energy consumption of electronic devices will continue to increase. One solution is to move towards quantum computation. Quantum computing uses qubits that utilise quantum mechanical effects such as superposition and entanglement. Qubits are two-level quantum systems, such as: photon polarisation, spin state of an electron or nuclei, and the excited-ground state of an atom.[2] Superposition allows the qubits to be in states between 0 and 1 in addition to being in standard bit states, 0 and 1. The superposition allows quantum computers being able access more states than a classical computer could for computation. Early examples that show the potential of quantum computation are Shor's algorithm[3] and Deutsch-Jozsa algorithm.[4] Shor's algorithm is a quantum algorithm for prime number factorisation and the performance of Shor's algorithm is compared to the best classical algorithm in Figure 1. Figure 1 compares the number of operations required for prime number factorisation of a number using the number field sieve algorithm and Shor's algorithm.[3] The classical algorithm scales exponentially with the number of digits, whilst Shor's algorithm scales asymptotically with the number of digits ,showing the potential of quantum computing solving problems quickly when the problem becomes more complex.[3] For developing a quantum computer, the

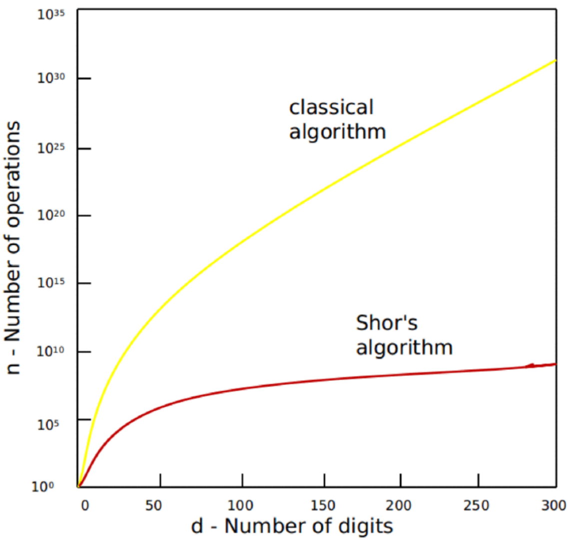

Figure 1: Graph describing the number of computational operations required for prime number factorisation using a classical algorithm and Shor's algorithm. Figure from source [5]

.

properties of ideal qubits are listed by the Divincenzo criterion.[2] The criterion states that the ideal qubit system should have the following characteristics: a physical scalable system with well characterised qubits; the ability to initialise the qubit state; long decoherence times compared to the gate operation time; a universal set of quantum gates and a qubit specific measurement capability. Divincenzo also states two additional desirable features for quantum communication: the ability to interconvert stationary and "flying" qubits and to transmit flying qubits between specified locations. The "flying" qubits generally refer to photon states.

There are a number of qubit systems that are being explored such as: trapped ion[6], quantum dot[7], superconducting[8], group IV vacancy centres in diamond (GeV[9], SiV[10], SnV[11], PbV[12]) and the Nitrogen Vacancy (NV) centre in diamond which is a main focus of this thesis.

For qubits in solid state hosts such as diamond, the host helps isolate the qubit from the environment, minimising decoherence. Diamond has a wide bandgap (5.5 eV) so any interactions with the defect will not interact with the diamond environment, a low spin orbit environment to minimise decoherence and a low nuclear spin environment.[13] This makes diamond an ideal host for defect centres for quantum computing. Along with the properties of NV centres, Weber et al have created a criterion of properties that defect centres and hosts should have for quantum computing.[13] The Weber criterion states that that the defect centre should have the following properties: to have a bound state that is paramagnetic, long lived with a energy splitting between at least two spin sub-levels; an optical pumping that polarises the qubit state; luminescence from qubit state transitions that varies by qubit sublevel; an optical transition that does not interact with the host and bound states that are separated sufficiently that to avoid transitions by thermal excitation.[13] For defect hosts, the Weber criterion states that the ideal host should have: a wide band gap; small spin-orbit coupling; availability as high quality bulk/thin-film single crystals; consist of elements with zero nuclear spin.[13]

In this introduction and literature review, the scheme for quantum computing using NV centres in diamond will be discussed along with the recent progress. Then the properties of the NV centre will be introduced along with the developments in diamond processing and NV fabrication. The applications of microcavities and solid immersion lenses for NV centres will then be discussed.

4.2 Measurement-based quantum computing

The quantum computing scheme discussed in this literature review focuses on measurement-based quantum computing using the electron spin of NV centres in diamond.[14] There are other examples of quantum computing schemes using NV centres such as coupling NV centres with superconducting qubits[15] or vibrational modes of carbon nanotubes.[16] Measurement-based quantum computing relies on using the photon emission of an optically active qubit, such as quantum dots or defect centres, to indirectly probe its quantum state and to remotely entangle the qubits. This schematic is shown in Figure 2. The process of generating entanglement in NV centres follows this procedure:

1. Generate a $|+\rangle = (|0\rangle + |1\rangle)$ superposition state on both NV centres using microwave excitation

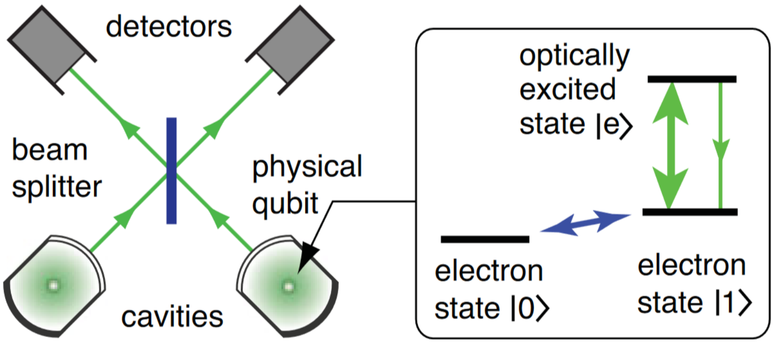

Figure 2: Schematic of the measurement-based entanglement process. Reproduced from source [14]. The beamsplitter has the effect of splitting the photons into two components, where one component is transmitted through the beamsplitter towards one photodetector and the other is reflected towards the other photodetector. When the photons arrive from both NV centres simultaneously, they are split by the beamsplitter and split photons from one NV centre interact with the split photons from the other. The photons interfere constructively/destructively so only one photon arrives at either photon detector. When this occurs, the photons are entangled and since the fluorescence is spin state dependent, the spins are also entangled.

2. Optically excite the $|1\rangle$ state to the $|e\rangle$ state so the NV centres are now in a $(|0\rangle + |e\rangle)$ state
3. The $|e\rangle$ state will relax and emit a photon
4. The photons from both NV centres will enter the beam splitter and interfere at the beam splitter
5. When a single photon is detected at either detector, entanglement is achieved

The entanglement can be extended to more NV centres by repeating the process between an entangled NV centre and the non entangled NV centre. This shows an advantage of measurement-based quantum computing that entanglement can be generated remotely and has been demonstrated for NV centres where entanglement has been performed between 3 m, 1280 m and 10 km.[17,18,19] The electron spin state of the NV can also be coupled to local nuclear spins such as the nitrogen atom and the ^{13}C isotopes present in the diamond.[20] The nuclear spins can be used as memory qubits and for quantum gates[21] and has been demonstrated with eight ^{13}C nuclear spins and the ^{14}N in the NV centre to form a ten qubit register.[22] The remote entanglement using NV centres and local entanglement with nuclear spins demonstrates the strong potential for scalability, as the total number of qubits available is not only limited to the number of qubits per system but also to the number of systems available for entanglement.[14,23] The entanglement efficiency of measurement-based quantum computing scales quadratically with the efficiency η of detecting a photon at the detectors.[24]

$$\eta = \eta_{ex}\eta_{em}\eta_{co}\eta_{tr}\eta_{det} \tag{4.1}$$

Where η_{ex} is the excitation probability of the emitter, η_{em} is the emission probability, η_{co} is the collection efficiency of the emission, η_{tr} is the probability of transmission to the detector and η_{det} is the detection efficiency of the detector. The excitation probability and emission probability will be discussed later in the literature review to discuss these parameters within the scope of NV centres. The collection efficiency η_{co} is affected by the ability to collect the photon emission and is reduced by the inability to capture all the spherical radiation from the NV centre and coupling losses to optical fibres. The collection efficiency can be optimised by working with high numerical aperture optics and minimising optical aberrations, which will reduce the coupling losses into the optical fibre. The transmission probability η_{tr}, is related to losses from photon transmission through optics and optical fibres which, can be minimised with anti reflective coatings and selecting optics with high transmission. The detection probability η_{det}, is related to the detection efficiency of the photon detector and can be maximised by using photon detectors with high detection efficiencies.

An alternative entanglement scheme is the extreme photon loss protocol where the entanglement efficiency scales linearly with η.[25,26] Nevertheless, it is important to maximise η to maximise the entanglement efficiency.

4.3 Diamond Nitrogen Vacancy (NV) centre

The defect structure of an NV centre is shown in Figure 3a. An NV centre can be described as a nitrogen substituted defect with an adjacent vacancy defect within the diamond and can be orientated along the <111> directions of the lattice.[27] The NV centre can be in a neutral (NV^0) or a negatively charged (NV^-) state, with the latter being the main interest. NV centres have also shown potential to be used for single photon sources, MASERs[28] and for sensing[29,30,31]. The electronic structure and optical spectrum of the NV centre are shown in Figures 3b and 3c respectively. The NV centre has a spin state dependent fluorescence where the excited states ^{3}E in spin states m_s=±1 will relax non-radiatively to the ground m_s=0 state through the singlet state whilst the excited m_s=0 state will radiatively relax back to the m_s=0 state.[13,14,24] The non-radiative transition also provides an optical initialisation of the spin state to m_s=0. The spin states can also be manipulated by applying a microwave field at around 2.88 GHz.[30] For the application of using NV centres as qubits, the spin dependent fluorescence can be utilised using direct spin conserving excitation of the ZPL with a 637 nm laser and controlling the spin state with microwaves.

The optical spectrum shows two distinct features which are the Zero-Phonon Line (ZPL) at 637 nm and the broad Phonon-Side Band (PSB) centred around 690 nm. For generating entanglement between NV centres, the photons emitted from the NV ZPL need to be indistinguishable in wavelength and linewidth.[17,18,24] The optical linewidth of NV ZPL is defined by the full width half maximum of the ZPL and is typically characterised using Photoluminescence spectroscopy. The optical linewidth is the Fourier transform representation of the excited state lifetime of the NV centre and the Fourier transform limit of the ZPL linewidth is 13 MHz. The excited state lifetime can be reduced by interactions with the host through phonons, strain and varying electric field interactions which leads to a broadening of the ZPL linewidth.[32,33]

At 293 K, the ZPL emission is weaker compared to the PSB emission and at lower temperatures, the ZPL emission becomes sharper and stronger whilst the PSB emission decreases. This is due to electron-phonon interactions, which broaden the ZPL linewidth at higher tem-

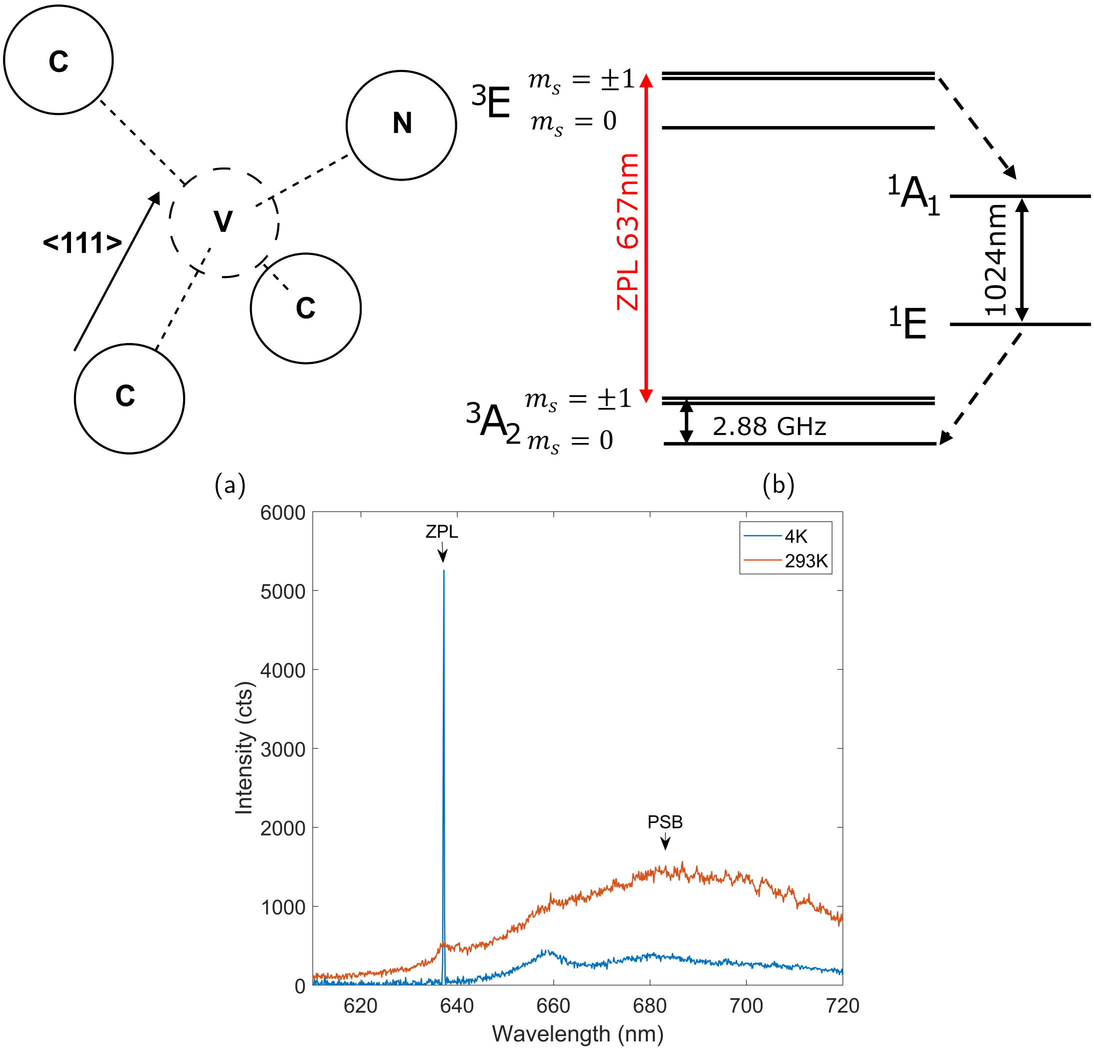

(a)

(b)

(c)

Figure 3: Schematic structure of the NV centre in a diamond lattice (a), the electronic structure of the NV$^-$(b) and the optical spectrum of NV$^-$ at room temperature and 4 K. Direct excitation and radiative transitions are shown by the solid vertical double arrows and the non-radiative transitions are shown by the dashed arrows. The electronic structure is reproduced from source [24].

peratures and this motivates the need to operate at lower temperatures. The electron-phonon interactions are associated with the temperature broadening are the dynamic Jahn-Teller effect and the coupling of symmetric photon modes.[34,35,36]

The electronic structure of the NV centre in diamond is also sensitive to strain, magnetic and electric fields which make them ideal as sensors.[30,31] Local strain and electric fields in the diamond will lift the degeneracy of the excited ^3E $m_s = \pm 1$ spin levels and create a linear splitting of the excited $m_s = \pm 1$ levels.[37,38] This sensitivity to the local environment also makes generating an array of NVs with identical optical properties difficult, as the ZPL emission from NV centres in different local environments is more distinguishable and this reduces the fidelity of the entanglement operation.[39] Various approaches have been used to address the ZPL distinguishability. The electronic structure can be controlled using the Stark effect allowing the ZPL transition wavelength to be matched with other NV centres.[17,40] This has been achieved by depositing gold strip lines near the NV defect to deliver a localised electric field to shift the ZPL emission.[40,17]. Other solutions involve converting the ZPL emission and performing entanglement at telecom wavelengths[41] or by applying frequency domain interferometry using Electro Optic Modulators (EOM) to convert the different ZPL wavelengths into a single wavelength to perform the entanglement.[10]

NVs also have longer spin decoherence times compared to other spin qubit systems at higher temperatures shown in Figure 4[42] and have achieved a decoherence time of 1.8 ms at room temperature.[31]

For generating entanglement using NV centres, the excitation probability η_{ex} is the probability of exciting the ZPL transition of the NV centre. The ZPL transition is affected by charge state switching and drift. The ZPL peak position can drift over multiple excitations of the ZPL. This is known as spectral diffusion and will reduce the excitation probability when a resonant laser at a constant wavelength is used for resonant excitation. Spectral diffusion of the ZPL peak can be mitigated by using Stark shifting the compensate the ZPL drift.[40] The NV centre can also be photo-ionised from the NV$^-$ state to the neutral NV^0 state during resonant

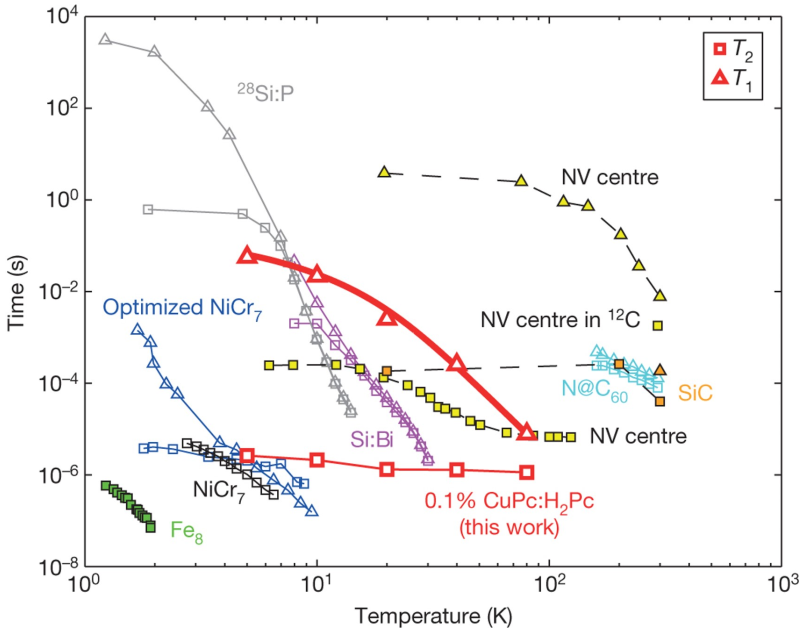

Figure 4: Plot of relaxation(T_1) and decoherence(T_2) times vs temperature for different spin qubit systems. Image reproduced from source [42].

excitation which will reduce the excitation probability. The photo-ionisation can be reduced by reducing the excitation power and by using a 532 nm pulse to repump the charge state back into the NV$^-$ state.[43,17]

The emission probability η_{em} is the probability that a suitable photon is emitted. For the NV centre, this is the fraction of emission that is emitted into the ZPL, which is given by the Debye-Waller factor of 4 %. Only 4 % of the photons are emitted as ZPL emission, whilst the rest is emitted in the PSB ,which will lead to a low emission probability for entanglement.[44] A solution to increase the ZPL emission is to couple the ZPL emission to optical microcavities to enhance the emission of the ZPL which will be discussed later in this literature review.

There are other potential colour centres in diamond that could be used as qubits such as the SiV and SnV centres. Group IV defects have inversion symmetry so they interact more weakly with the host.[33,45] Compared to NV centres, the group IV centres have a much higher Debye-Waller factor (70 %) but have a lower spin lifetime due to phonon interactions.[46] The phonon interactions can be suppressed by operating at mK temperatures[47] or by strain controlling the diamond environment.[48,49]

4.4 Diamond processing

The forms of diamonds used to host NV centres range from bulk diamond to the nanometre scale forms such as nanodiamond and diamond membranes which are becoming the main interest. Diamonds can be fabricated using High Pressure High Temperature (HPHT) and Chemical Vapour Deposition (CVD). Important parameters to control during diamond fabrication include the strain, surface roughness, surface passivation, impurity concentration and isotope concentration. Strain within the diamond will lift the degeneracy of ^{3}E $m_s = \pm 1$ and reduce the indistinguishability of the ZPL transitions for entanglement.[37] Surface roughness causes scattering losses which will reduce photon collection.[50] The surface roughness can be reduced using inductively coupled plasma-reactive ion etching or focused ion beam milling, where 0.2 nm[51] and 0.29 nm[52] root mean squared (rms) surface roughness have been achieved. When exciting NV centres with nitrogen impurities within the focal volume of excitation, the nitrogen atoms can be photo-ionised, which creates a fluctuating electric field and causes the spectral drift of the NV ZPL. Using diamonds with low concentration nitrogen content (ppb) is desired to reduce the spectral diffusion.[40] Carbon isotopes have been shown to shorten the electron spin decoherence time, but as mentioned previously, the nuclear spins can be used as memory qubits.[31] The nuclear spin of ^{13}C has been used as a memory qubit where the nuclear spin decoherence time of around 8.2 ms at room temperature[53]. This is within the same order as the decoherence time for nitrogen.[54] Maurer et al have implemented two methods to increase the C^{13} decoherence time. The C^{13} nuclear spin can be decoupled from the electron spin by optically switching the charge state from NV$^-$ to NV^0 using a 532 nm laser.[53] This led to an increase in decoherence time of around 0.53 s. Further improvement has been demonstrated by applying a Mansfield-Rhim-Elleman-Vaughan (MREV) decoupling sequence which enables decoherence times to exceed 1 s at room temperature.[53,55] Another scheme using dynamic decoupling sequences has achieved a longer decoherence time on the ^{13}C nuclear spin of up to

25 s.[22]

4.5 NV fabrication

NV centres are naturally occurring defects within diamond but they can be also introduced into diamond using techniques such as: implementing defects during the CVD formation of diamond[27,31], ion implantation[56], electron irradiation[57] and laser writing[58,59]. The process of forming NV centres can be broken down into three stages: introducing nitrogen into the diamond; vacancy generation and vacancy diffusion. Ideal parameters to control during NV formation would be orientation, depth, position and the concentrations of defects.

The NV centres are typically formed into the diamond after CVD diamond growth but can also be formed during the diamond growth process. Preferential orientation of NV centres ($74 \pm 4\%$) in the (111) direction can be achieved using microwave plasma-assisted CVD.[27] The depth of NV formation can also be controlled during diamond growth by delta doping, where a nitrogen rich layer is deposited to confine the depth of NV formation.[60] The nitrogen atoms can be introduced post-fabrication of the diamond through ion implantation. During the ion implantation process, vacancies can be formed and the vacancies can then be diffused to the nitrogen atoms to form NV centres using thermal annealing.[61] There have been demonstrations of fabricating NV centres with <100 MHz ZPL linewidths using ion implantation of nitrogen and thermal annealing.[61,62] However, further studies show that NVs formed with implanted nitrogen atoms tend to have broader ZPL linewidths than NVs formed with native nitrogen atoms.[63] This was shown by implanting ^{15}N atoms to differentiate between the implanted and native nitrogen atoms in the diamond.[63] NV centres formed with native nitrogen atoms in the diamond can be fabricated using ion implantation with lighter atoms such as helium, to generate vacancies in the diamond and then thermally annealing the diamond to diffuse the vacancies towards the nitrogen atoms.[64] Lateral positioning of NV formation using ion implantation can be achieved using an atomic force microscopy tip with a hole as an aperture[65] or by using a focused ion beam.[64]

The other methods of vacancy generation include electron irradiation[57] and laser writing.[58] Electron irradiation can generate vacancies at millimetre depths, which is typically deep enough to form NV centres throughout the whole diamond.[66] Lateral confinement using electron irradiation can be achieved using a transmission electron microscope and has been combined with delta doping to provide lateral and depth control of the NV formation.[67] The ZPL linewidths of NVs formed using electron irradiation can be low. Ruf et al have achieved average NV ZPL linewidths of 39 MHz using electron irradiation to generate vacancies and thermal annealing to diffuse and minimise the lattice damage.[57,68] The laser writing process for vacancy generation enables the formation of vacancies at any position and depth within the sample. Chen et al have shown using laser writing and thermal annealing, formation of NV centres at 50 μm depths where three of the NV centres showed <20 MHz ZPL linewidths.[58]

An alternative to using thermal annealing for vacancy diffusion is laser diffusion. The power of laser writing pulses used for laser writing vacancies can be reduced to diffuse the vacancies towards nitrogen atoms to form NV centres.[59] NV centres have been formed with laser writing and diffusion in diamond with high nitrogen concentration (ppm) which will broaden the ZPL linewidth.[40,59] Laser writing requires high laser intensities to generate the vacancies and the use of adaptive optics to optimise laser power delivery to the sample by minimising the spot size. Alternative approaches to achieving the high intensity have been demonstrated using solid immersion lenses[69] and bullseye optical cavities.[70]

4.6 Optical microcavities

The low ZPL emission of the NV centre can be enhanced by coupling the NV to a microcavity. Microcavities consist of an enclosed structure that can confine photons within it. Depending on the cavity length, the microcavity allows only photons with specific frequencies to oscillate and remain within the cavity.[71] The allowed frequencies that can oscillate within the microcavity are given by the following formula.[32]

$$\omega_m = \frac{m\pi c}{nL} \tag{4.2}$$

Where ω_m is the supported frequency, m is the number of the antinodes, c is the speed of light, n is the refractive index of the cavity and L is the cavity length. Within the scope of this thesis, the cavity coupling strength regime is weak coupling. When NV centres are cavity coupled within this regime, the cavity can enhance the photon emission of the NV ZPL through Purcell enhancement and reduce the PSB emission. The Purcell enhancement describes the enhancement of photon density of states introduced by the optical cavity relative to the photon density of states in free space.[32] The extent of the enhancement is determined by the Purcell factor, F_p in Equation 4.3.[72,73]

$$F_p = \left[\frac{3}{4\pi^2}\left(\frac{\lambda}{n}\right)^3 \frac{Q}{V_m}\right]\left(\frac{|\mu\ .E|}{|\mu||E|}\right)^2 \frac{1}{1+4Q^2(\frac{\lambda}{\lambda_{cavity}}-1)^2} \tag{4.3}$$

Where λ is the wavelength of the emission, n is the refractive index, Q is the quality factor, V_m is the mode volume, μ is the dipole moment and E is the electric field.

The main parameters to maximise F_p are to have a large quality factor Q and a low mode volume V_m. The second bracketed term describes the orientation between the dipole and the electric field. The NV centre orientation along the <111> directions in the diamond host limits the alignment of the NV centre to the electric field. The third term factors the effect of detuning of the wavelength from the cavity wavelength.

There are many microcavity designs that have been coupled to NV centres such as: photonic crystal[73], bullseye[74], whispering gallery resonators[75] , microring[76] and Fabry-Pérot cavities[72]. However, most of the cavity designs are fixed structures that have limited tunability, so any error in the cavity design will detune the cavity off resonance with the NV ZPL and lower the Purcell factor. The tunability of whispering gallery resonators, photonic crystal cavities and Fabry-Pérot cavities has been shown. Whispering gallery resonators can be stretched using piezo-driven nano-positioners to achieve 0.6 nm tunability.[77] However, there has been no demonstration of tuning whispering gallery resonators with NV centres. For photonic crystal cavities, the cavities can be tuned by 5 nm from condensing gas in the cavity[78] and have been demonstrated with SiV centres.[79] However, this tuning process is slow.[80] Another issue is that most of the cavity structures require the NV centre to be near the surface, which will broaden the ZPL linewidth and introduce drift in the ZPL position.[81] Fabry-Pérot cavities can be tuned by adjusting the spacing between the cavity mirrors and can incorporate thicker diamond membranes, which will isolate the NV centres from the surface.

4.7 Fabry-Pérot microcavity

Fabry-Pérot cavities consist of two mirrors parallel to each other and the spacing between the mirrors can be adjusted to tune the cavity length. There are different configurations of mirrors that can be used such as planar-planar, planar-concave and concave-concave each with its own advantages and disadvantages. The planar-concave cavity is the configuration that is focussed on in this thesis and Figure 5a shows an image of a planar-concave cavity. The concave mirror will provide lateral confinement of the light within the cavity and a smaller radius of curvature (RoC) of the concave mirror provides a stronger confinement. The concave mirror profiles can be formed by Focused ion beam milling[82,72], laser ablation[83,84], chemical etching[85] and laser writing.[86] Figure 5b shows the effect of the cavity when coupled to an NV centre. When the cavity is resonant with the NV ZPL, the ZPL emission is enhanced while the PSB emission is suppressed. Fabry-Pérot microcavities may not be able to obtain higher Purcell factors compared to other cavity structures, but the main advantage of Fabry-Pérot microcavities is that the cavity wavelength can be tuned in situ and can be coupled to other NV centres that are located laterally across the planar mirror. The mirror coatings used for Fabry-Pérot microcavities are typically either metallic or dielectric. The choice of coating affects the cavity mode volume and mirror reflectivity R.[87] Dielectric coatings offer higher reflectivities ($R >$ 99 %) but the electric field can penetrate deeper into dielectric coatings, which limits

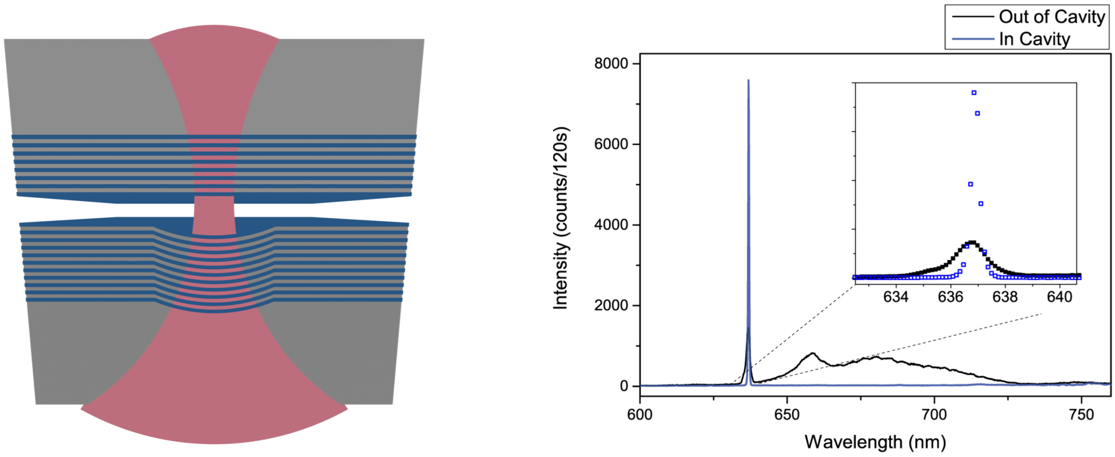

(a) (b)

Figure 5: (a)Graphic of a planar-concave Fabry-Pérot microcavity with Bragg mirrors. (b) Optical spectrum of an NV centre before and after cavity coupling. Spectrum reproduced from source [72].

the minimum cavity mode volume for shorter cavity lengths. Metallic mirrors limit the electric field penetration but offer lower reflectivities ($R = 95$ %).[88]

Fabry-Pérot cavities have been coupled to NV centres within nanodiamonds and diamond membranes. For nanodiamonds, a Purcell factor of F_p=10 and quality factor of $Q \simeq 3000$ have been achieved at 77 K using a concave mirror with a 7.6 µm RoC.[72,24] For a 0.77 µm thick diamond membrane, a Purcell factor of F_p=2 and quality factor of $Q = 58500$ have been achieved at 4 K using a 16 µm RoC concave mirror.[62] The low Purcell factor when coupling with a diamond membrane is associated to the cavity resonance coupling with an 'air-like mode', where the electric field is confined to the air gap within the cavity.[62,50] When a diamond membrane is cavity coupled, the electric field of the resonant cavity mode can be stronger in the diamond membrane ('diamond-like mode') or in the air gap ('air-like mode'). A stronger electric field in the diamond is preferred for stronger coupling to the NV centre and the electric field regime depends on the diamond membrane thickness relative to the cavity length.[50] A demonstration of cavity coupling to a bare diamond membrane with a 'diamond-like mode' has been shown with a quality factor of Q=120000 and a predicted Purcell factor of F_p=170.[84]

The ZPL linewidths of the NVs that were coupled were 296 GHz and 1 GHz for the nanodiamond and the diamond membrane respectively. The large ZPL linewidths are likely associated with the high surface area-to-volume ratio of the nanodiamonds and the close proximity to the diamond surface where surface defects may introduce strain and electric fields.[62] Using thicker diamond membranes to host NV centres away from the surface would help isolate the NVs from any defects or fields induced by the surface and produce NV centres with narrower linewidths. There is a compromise on the decision on the diamond thickness to host the NV centres. There is a trade off between having small/thin diamonds to minimise cavity mode volume and enhance the Purcell factor, against the contribution of surface defects broadening the ZPL as the diamond becomes smaller.[57] A maximum ZPL linewidth of < 100 MHz has been proposed by Ruf et al, which is based on the timing resolution of the photon detector limiting the photon indistinguishability.[89,90]

NVs with ZPL linewidths under 100 MHz have been achieved in a 3.4 μm thick diamond membrane using electron irradiation/thermal annealing to produce the NV centres and using dicing and reactive ion etching to thin the diamond.[57] An alternative process that may produce thinner diamond membranes of high quality is to use an additive process that has been demonstrated shown by Guo et al.[91] They create the membrane by initially creating a buried damaged layer the bulk diamond using He^+ implantation, growing the desired thickness of membrane with Plasma enhanced CVD and then removing the membrane by electrochemically etching the damaged layer.

4.8 Cavity locking

One of the difficulties in using Fabry-Pérot cavities is that they are susceptible to vibrations, which will decouple the cavity resonance from the NV ZPL and lead to a reduction in the Purcell factor.[81] This has been observed for a fibre based cavity coupled with NV centres in a diamond membrane, where the closed loop cryostat vibrations introduced decoupling. The vibrations broadened the linewidth of the cavity mode to 14 GHz - 50 GHz (0.48 nm - 1.78 nm).[92] The linewidth broadening could be minimised to 14 GHz (0.48 nm) by taking measurements during the period of the cryostat operation cycle with the least vibration. Further stabilisation could be achieved by implementing passive and active locking methods.

Passive stability methods which involve implementing components in the cryogenic system with high resonance frequencies and using vibration isolation has been implemented to achieve cavity stabilities of 25 pm.[93] Active locking methods such as Pound Drever Hall (PDH) cavity locking[94] or side-of-fringe locking of the cavity transmission[95] have been demonstrated. For fibre based Fabry-Pérot microcavities, cavity locking using PDH in a bath cryostat has achieved a 5 pm stability.[96] For side-of-fringe locking, cavity stabilities of 5.7 pm and 10.6 pm have been achieved with fibre based Fabry-Pérot microcavities in a closed-loop cryostat.[95] In this thesis, another cavity locking method using cavity fringe stabilisation will be investigated.

4.9 Resonance fluorescence

When performing entanglement with NV centres, the ZPL is excited resonantly and the ZPL emission is collected for entanglement. The backscattered light from the excitation laser must be filtered out to minimise noise in the entanglement process. This is achieved through cross-polarisation extinction and time gating the collection so detection occurs only after the excitation laser pulse has decayed.[17] For cross-polarisation extinction, it was found that the extinction ratio can be enhanced by having a reflecting surface between the two linear polarisers and having confocal light detection.[97] This analysis was further expanded by modelling the extinction ratio with an increasing number of mirrors between the polarisers, and it was found that the increasing reflections reduce the cross-polarisation extinction ratio.[98] This emphasises the importance of reducing reflections when designing and constructing the confocal microscope for resonance fluorescence. There has been a demonstration of resonant excitation within a Fabry-Pérot microcavity.[99] However, the cross extinction ratio was 10^4, limiting the ability to filter out the excitation laser light. Cavity-coupled resonance fluorescence was demonstrated by Yurgens et al., by using the cavity to enhance the excitation field within the cavity and achieving an

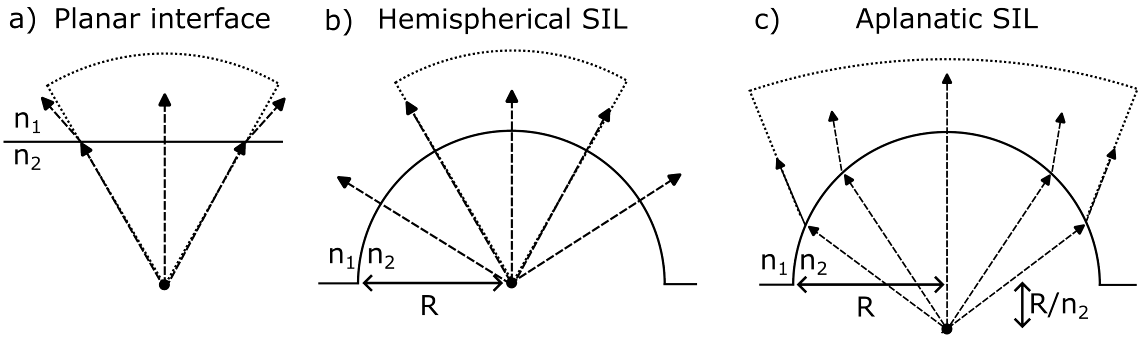

Figure 6: Schematics of the emission path of the rays through a Planar interface, Hemispherical SIL and Aplanatic SIL. The dashed line cone represents the region of rays that is collected by the objective lens.

extinction ratio of 10^5.[100] Yurgens et al. also mention that the need to time gate the NV centre fluorescence will relax as cavity coupling will reduce the NV fluorescence lifetime, becoming comparable to the excitation pulse as the Purcell factor increases.[100].

4.10 Solid Immersion Lenses

Using Solid Immersion Lenses (SIL) is a method for improving the collection efficiency, η_{co} for NV centres in bulk diamond and was used in the earlier demonstrations of entanglement using NV centres.[101,17] A comparison of the light rays leaving the emitter and refracting across the surfaces of a planar interface, hemispherical SIL and an aplanatic SIL are shown in Figure 6. When the rays from an emitter pass through a planar interface, depending on the refractive index mismatch, the rays can refract away from the perpendicular direction of the surface. When a lens is used to collect these rays, the refracted rays diverge away from the angle of collection of the lens represented by the cone. This results in less light being collected by the lens.

A SIL consists of a hemispherical cap with a radius R and refractive index n_2 which is centred laterally around an emitter. There are two regimes of operation for the SILs being hemispherical or aplanatic where the former is a main focus in this thesis. Hemispherical SILs are positioned so that the emitter is in the centre of the SIL, so light from an emitter leaves the surface at normal incidence of the SIL and more rays are collected by the lens compared to a planar interface. The SIL surface also ensures that focussed light used for emitter excitation does not experience refraction and aberration, so a smaller focussed spot size is formed and a more efficient excitation. The refractive index of the SIL should match the refractive index of the bulk material to minimise refraction and reflection between the interface of the bulk material and the SIL.[102] From Finite Different Time Domain (FDTD) modelling[103] and analytical modelling[102], it is expected that the amount of collected light from a hemispherical SIL would be at least 5 times higher compared to collecting light from a planar interface.

Aplanatic SILs are positioned so that the emitter is positioned at a distance R/n_2 below the centre of the SIL, where R is the radius of the SIL and n_2 is the refractive index of the SIL. In this condition, the light radiated from this position is refracted through the surface of the SIL, but in the direction perpendicular to the surface. This enhances the amount of rays that the lens would normally collect.

Diamond SILs can be fabricated by using Focused Ion Beam (FIB) milling to remove material from the hemispherical shape, where 5 µm radius SILS have been formed.[104,17,103] Light collection using 5 µm radius SILs has shown increases of 8 to 10 times the amount of light collected compared to light collected from NV light collected from a planar interface.[103] However, the ion beam can introduce local strain in the diamond, which could shift the NV ZPL[37] and can even cause the NV to disappear.[105]

There is also the additive method of placing a SIL on top of the diamond. Millimetre scale SILs made from diamond[106] and gallium phosphide[107] have been used to enhance light collection and show increases of 6 times and 9 times respectively. Micrometer-scale SILs made from gallium nitride have also been shown[108] where a 2 times increase has been demonstrated.

When the NV emission is collected and refocused into an optical fibre, any imperfections in the optics or misalignment along the optical path can introduce optical aberration. Optical aberrations describe the deviations of the optical wavefront with respect to the reference wavefront. The reference wavefront is planar for a collimated wavefront or spherical for a converging/diverging wavefront. Optical aberrations will increase the spot size and alter the spot shape of the refocused light leading to a lower collection efficiency into the optical fibre. Implementing SILs eliminates the optical aberration that would be introduced when light from an emitter passes through a planar interface.

Other sources of aberrations that can be introduced by the imperfections of the SILs. The aberrations introduced by the imperfections have been modelled for both hemispherical[109,110] and aplanatic[111] SILs. For the hemispherical SILs, Baba et al have described the aberration for the shape error, thickness error and air gap thickness for stick on SILs[109], and Lang et al have described the SIL aberrations using a polynomial expansion of spherical aberration as a basis to describe the third-order aberrations in the SIL.[110] The SIL aberration model by Lang et al shows a limitation on the use of third-order aberrations to describe the aberrations for higher values of numerical aperture. When the model is compared to ray tracing results, the model shows deviations in spherical aberration at higher numerical apertures.[110] High numerical aperture lenses are generally used for greater light collection, so aberrations from SIL imperfections need to be described accurately at higher values of numerical aperture to understand the significance of the SIL imperfections on collection efficiency.

4.11 Conclusion

An introduction to quantum computing and the progress of using NV centres as qubits is presented. Entanglement between NV centres has been shown in literature and memory qubits can be implemented by using the nuclear spin of local ^{13}C isotopes and the nitrogen atom of the NV centre, showing the scalability of a qubit system using NV centres.

The NV centre has a low Debye-Waller factor, where only 4 % of the overall NV emission is emitted as ZPL emission, which needs to be improved for a higher entanglement rate. Cavity-coupling NV centres can be used to enhance the ZPL emission through Purcell enhancement. Various microcavity structures have been coupled to NV centres but there are challenges with different designs, one of them being the cavity tunability which is limited for fixed structures.

The approach in this thesis is to use Fabry-Pérot microcavities, which can be tuned in situ to NV centres and have been coupled with NV centres in nanodiamond and diamond membranes.

Entanglement also requires indistinguishability of the ZPL emission between the NV centres. The ZPL linewidth and position are sensitive to the local strain and charge environment in the diamond host, which broadens the linewidth and shifts the ZPL position and this reduces the indistinguishability of ZPL between the NV centres. For the NV centres that were cavity coupled to Fabry-Pérot microcavities, the ZPL linewidths were broad (> 1 GHz) indicating that the diamond processing needs to be improved to lower the local strain and charge environment in the diamond. The ZPL indistinguishability can be improved by hosting NV centres in thicker diamond membranes, improving the diamond quality for thinner membranes or by using NV fabrication methods that minimise the damage to the diamond host such as electron irradiation and laser writing. ZPL linewidths of <100 MHz have been achieved in 3.4 μm thick diamond membranes using dicing and reactive ion etching to form the membrane.[57] High quality diamond has been achieved for thinner diamond membranes (50 - 250 nm) using a "smart-cut" and diamond overgrowth procedure.[91] Combining the high quality diamond membrane fabrication with laser writing and annealing could potentially generate arrays of NV centres in diamond membranes with narrow ZPL linewidths.

Another limitation of using Fabry-Pérot cavities is the cavity instability which decouples the cavity mode resonance from the NV ZPL and reduces Purcell enhancement. Strategies to stabilise the cavity involve implementing passive isolation, mechanical design to mitigate mechanical resonances and applying active cavity locking.

Another factor that affects the entanglement rate is the collection efficiency. Optical aberrations from focusing into a sample or from misalignment of optics can reduce the collection of light when the light is coupled to single-mode fibres. Using SILs is another method of enhancing the collection of NV photon emission by reducing the aberration from focusing into the diamond. However, errors in the relative positioning of the SIL with the emitter and shape error can introduce aberrations and reduce the photon collection efficiency. The positioning error of the SIL has been modelled using third-order aberrations but for higher numerical apertures, the model deviates from ray tracing results, becoming inaccurate for high numerical aperture light collection.

This thesis will explore different aspects of developing photonic devices using NV centres in diamond for quantum computing. Firstly, the results of ZPL linewidth characterisation of the first laser written and diffused NV centres in electronic grade diamond will be presented to benchmark the quality of NVs formed by laser diffusion. Secondly, the results of cavity stabilisation of Fabry-Pérot microcavities coupled to nanodiamonds using fringe locking will be presented to explore the feasibility of fringe locking for low temperature cavity coupling with NV centres. For the final study, the aberrations in Fabry-Pérot microcavities and SILs will be presented. For the Fabry-Pérot microcavity, a model is presented for spherical aberration as a function of the mirror substrate thickness and the numerical aperture of the cavity mode. Then the aberrations in the microcavity will be monitored using adaptive optics to apply aberration correction to compare the model results with. For SILs, a model describing the aberrations introduced when an emitter is displaced from the centre of the SIL. The aberration studies aim to explore how the design or imperfection of the photonic device affects the collection efficiency η_{col} and consequently, the entanglement rate.

5 Theoretical Background

5.1 Introduction

In this section, the theoretical background for optical cavities is presented. Then, the theory of Gaussian beam optics is presented to describe the cavity modes for hemispherical cavities, which are used in this thesis. The theory of cavity quantum electrodynamics is presented to describe the effects of cavity coupling to the NV centre and how the cavity coupling can enhance the emission of the NV centre through Purcell enhancement.

The theory for the Distributed Bragg Reflector (DBR) is presented for calculating the reflectivity of the mirrors used for cavity coupling. For optical aberrations, Zernike polynomials are introduced as a basis for describing optical aberrations. The Zernike polynomials will be used to describe the optical aberrations of the microcavity and the solid immersion lenses. The theory for describing the spherical aberration introduced when focusing through a planar interface with a high refractive index is also presented. These results are used for modelling the optical aberrations through the planar mirror of the hemispherical microcavity.

5.2 Optical Resonators

One of the simplest designs for a Fabry-Pérot resonator is with two planar mirrors with reflectivities R_1 and R_2 shown in Figure 7.

The resonant wavelength condition for the cavity occurs when the cavity length is equal to an integer number of half-wavelengths.

$$\lambda_{resonant} = \frac{2nd}{q} \tag{5.1}$$

Where d is the cavity length, n is the refractive index of the medium between the mirrors and q is the number of anti-nodes of the wave. The transmission through the cavity is given by

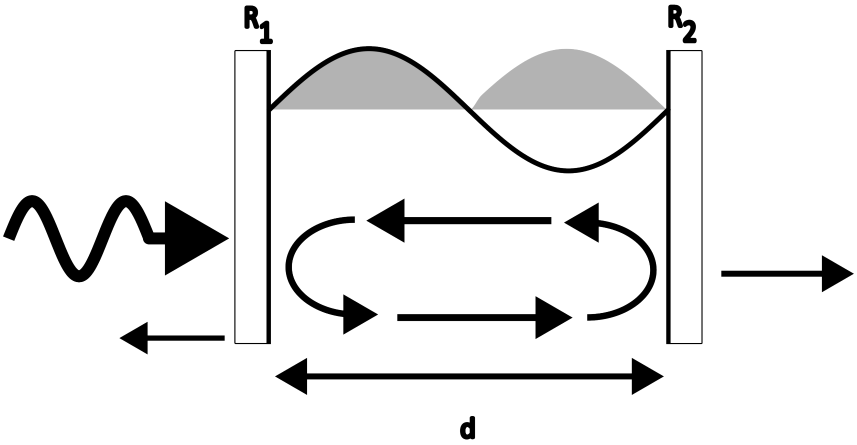

Figure 7: Schematic of a planar-planar cavity with mirrors of reflectivity R_1 and R_2 and a standing wave with $q = 2$.

Equation (5.2) and a transmission spectrum is shown in Figure 8.

$$T_{cavity} = \frac{1}{1 + \frac{4\mathcal{F}^2}{\pi^2} sin^2(\frac{2nd}{\lambda})} \tag{5.2}$$

Maxima in transmission occur at resonant wavelengths of the cavity. The width of the transmission peaks is related to the cavity finesse $\mathcal{F}$:

$$\mathcal{F} = \frac{2\pi}{\delta\lambda} = \frac{\Delta v}{\delta v} \tag{5.3}$$

Where $\delta\lambda$ and δv are the Full Width Half Maximum (FWHM) linewidth of the cavity mode in wavelength and frequency respectively and Δv is the frequency spacing between cavity modes. The cavity finesse is also related to the reflectivities of the mirrors R_1 and R_2.

$$\mathcal{F} = \frac{\pi(R_1 R_2)^{1/4}}{1 - \sqrt{R_1 R_2}} \tag{5.4}$$

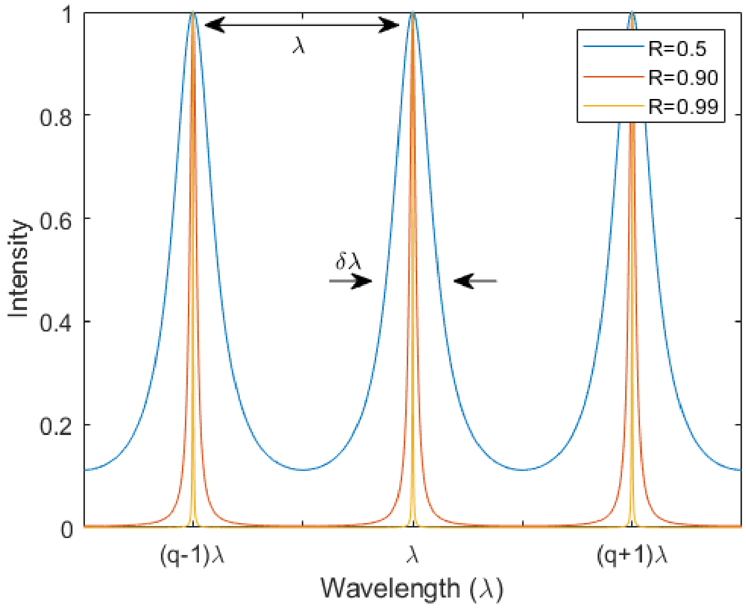

Figure 8: Cavity transmission spectrum for a 1D cavity in terms of numbers of wavelengths q. The reflectivity changes the transmission linewidth, $\delta\lambda$ and the minimum transmission of the cavity.

The reflectivity of the mirrors used in this thesis is $R_1 = 99.8\%$ and $R_2 = 99.9\%$, so the expected finesse of the cavity will be around $\mathcal{F} = 2092$. Another figure of merit for cavity performance is the Quality factor Q, which describes how well the cavity retains its energy and is related to the cavity finesse

$$Q = \frac{2\pi \times total\ energy}{Energy\ loss\ per\ cycle} = \frac{\omega}{\delta\omega} = \frac{2\pi q \Delta v}{2\pi \delta v} = q\mathcal{F} \tag{5.5}$$

The cavities used in this thesis are hemispherical cavities which also have the benefit of laterally confining the field. For describing the cavity profiles of hemispherical cavities, Gaussian optics will need to be introduced.

5.3 Gaussian Beam Optics

The wave equation can be derived from Maxwell's equations in free space ($\rho = 0$ and $J = 0$).

$$\nabla^2 E = \frac{1}{v^2}\frac{\delta^2 E}{\delta t^2} \tag{5.6}$$

For monochromatic waves, the solution can be written in the form

$$E(r,t) = E(r)e^{i\omega t} \tag{5.7}$$

Substituting this solution back into Equation 5.6 gives the Helmholtz equation

$$[\nabla^2 + k^2]E(r) = 0 \tag{5.8}$$

For a beam propagating along the z direction, where the wavefronts are mostly normal to the z direction, the solutions come in the form.

$$E(r) = a(x,y,z) \times e^{ikz} \tag{5.9}$$

Substituting Equation 5.9 into the Helmholtz equation and using the paraxial approximation where $\frac{\partial^2 a}{\partial z^2} \ll k\frac{\partial u}{\partial z}$ and $\frac{\partial^2 a}{\partial z^2} \ll \frac{\partial^a}{\partial x^2}, \frac{\partial^a}{\partial x^2}$ the Helmholtz equation forms the paraxial wave equation.

$$\nabla_\perp^2 E + 2ik\frac{\partial u}{\partial z} = 0 \tag{5.10}$$

One of the solutions to the paraxial wave equation is the Gaussian beam equation.

$$\begin{aligned}
E = i\frac{E_0}{z_r} & \qquad \text{constants} \\
\times \frac{\omega_0}{\omega(z)} & \qquad \text{amplitude reduction along z} \\
\times e^{i(kz-\omega t)} & \qquad \text{wave propagation along z} \\
\times e^{-i\alpha(z)} & \qquad \text{Guoy phase shift along z} \\
\times e^{\frac{-r^2}{\omega(z)^2}} & \qquad \text{Gaussian transverse profile with spot size } \omega(z) \\
\times e^{\frac{ikr^2}{2R(z)}} & \qquad \text{wavefront with radius of curvature at z}
\end{aligned} \tag{5.11}$$

Where E_0 is the amplitude at $z = 0$, z_r is the Rayleigh range that describes the distance before the beam amplitude decays by $\sqrt{2}$. The other beam parameters are described in Equations 5.12 - 5.15.

$$\omega_0^2 = \frac{\lambda z_r}{\pi} \text{ beam waist at z=0} \tag{5.12}$$

$$\omega(z)^2 = \omega_0^2(1 + \frac{z^2}{b^2}) \text{ beam waist at z} \tag{5.13}$$

$$\alpha = arctan(\frac{z}{z_r}) \text{ guoy phase shift at z} \tag{5.14}$$

$$R(z) = z + \frac{z_r^2}{z} \text{ radius of curvature of the wavefront at z} \tag{5.15}$$

The beam waist ω_0 can be related to the divergence of the beam and the numerical aperture, NA

$$NA = n\sin(\theta) = n\sin(\frac{\lambda}{\pi\omega_0}) \tag{5.16}$$

For forming low loss cavity modes, the radius of curvature of the Gaussian beam $R(z)$ (Equation 5.15) at the mirror surface must match the incident radius of curvature (RoC) of the mirror $R_{1,2}$.

$$R(z_1) = z_1 + \frac{z_R^2}{z_1} = R_1 \tag{5.17}$$

$$R(z_2) = z_2 + \frac{z_R^2}{z_2} = R_2 \tag{5.18}$$

$$L = z_2 - z_1 \tag{5.19}$$

Where L is the cavity length. Solving Equations 5.17, 5.18 and 5.19 determines the Rayleigh range of the mode formed within the cavity, z_r.

$$z_r^2 = \frac{g_1 g_2 (1 - g_1 g_2)}{(g_1 + g_2 - 2 g_1 g_2)^2} L^2 \tag{5.20}$$

Where,

$$g_i = 1 - \frac{L}{R_i}$$

$$0 < g_1 g_2 < 1$$

For a hemispherical cavity, R_1 is flat ($R_1 \to \infty$) and substituting Equation 5.20 into Equation 5.12, the beam waist can then be defined by the RoC of the concave mirror R_2 and cavity length L.

$$\omega_0^2 = \frac{\lambda}{\pi} \sqrt{R_2 L - L^2} \tag{5.21}$$

This definition of the beam waist can then be used in Equation 5.16 to relate the cavity NA to the cavity length and the RoC of the concave mirror. This will be used later to see how the cavity NA affects the spherical aberration and collection losses in the cavity emission.

Another formulation to describe the modes formed within the cavity is the Hermite-Gaussian beam equation shown by Equation (5.22)

$$\begin{aligned} E = i\frac{E_0}{z_R} &\times \frac{\omega_0}{\omega(z)} \times e^{i(kz-\omega t)} \times e^{-i\alpha(z)} \times e^{\frac{-r^2}{\omega(z)^2}} \times e^{\frac{ikr^2}{2R(z)}} \\ &\times H_l\left(\frac{\sqrt{2}x}{\omega(z)}\right) H_m\left(\frac{\sqrt{2}y}{\omega(z)}\right) \\ &\times e^{-i(l+m)\alpha} \end{aligned} \tag{5.22}$$

The Hermite-Gaussian beam equation consists of the Gaussian beam profile in Equation 5.11 with additional terms H, which are the Hermite polynomials that describe the intensity profiles of the transverse mode orders l and m and an additional Guoy phase change.

There is also a π phase change introduced when the electric field sign is negative. The intensity profiles and wavefronts are presented in Figure 9. The wavefronts of the Hermite-Gaussian modes will be used to predict the aberrations present for each of the Hermite-Gaussian modes. The resonance criteria for the Hermite-Gaussian cavity modes are described by Equation 5.23, where the round trip phase for resonance needs to be an integer number of π and is dependent on the cavity mode indices and cavity length.

$$p\pi = kL - (l + m + 1)\{\alpha(z_2) - \alpha(z_1)\} \tag{5.23}$$

Where p is the integer number of π phase round trips and α is the Guoy phase shift. This can be used to derive the resonance frequency of a cavity v with cavity mode indices q, l, m, cavity radius of curvature R and cavity length, L.

$$v_{q,l,m} = \frac{\lambda}{2\pi}\left[q + \frac{1}{\pi}(l + m + 1)\arccos\left(\sqrt{\frac{R - L}{R}}\right)\right] \tag{5.24}$$

The higher-order cavity modes that share the same total transverse mode index *(l+m)* are energetically degenerate. This is shown in Figure 10, where the lower wavelength peaks are able to support more higher-order cavity modes. The spacing between the transverse modes is evenly spaced and depends on the RoC of the concave mirror and the cavity length. Only the fundamental cavity mode $(l + m = 0)$ is desired as the electric field is the strongest in the centre of the cavity mode and the transverse cavity modes can be suppressed by adjusting the concave mirror laterally to minimise the transverse mode peaks in the optical spectra.

5.4 Cavity Quantum Electrodynamics

One of the main focuses of this thesis is utilising light-matter interaction between the NV centre and the optical cavity. When an optically active atom is placed within the cavity and the emission is resonant with the cavity mode, the atom will couple with the cavity mode. The

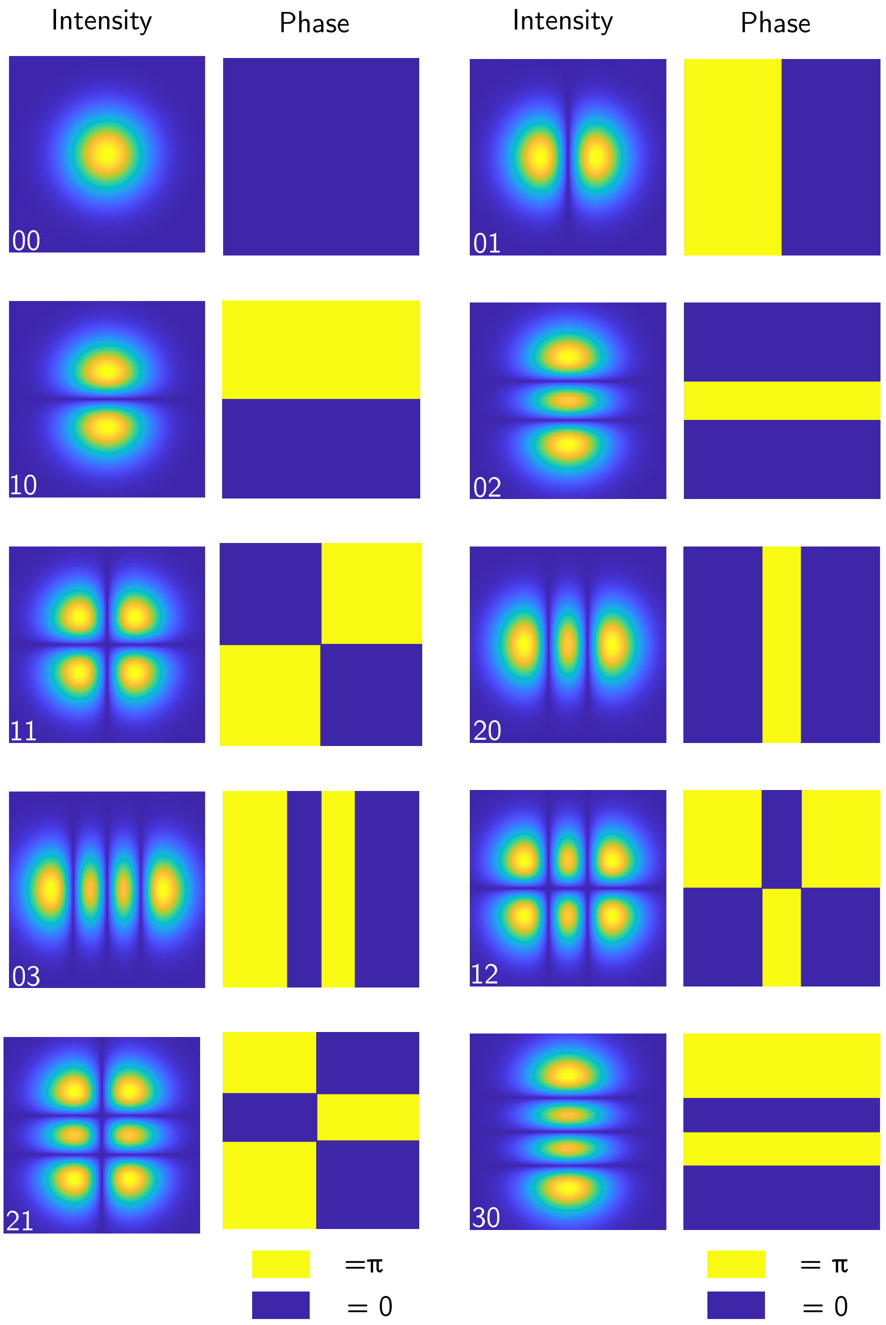

Figure 9: Intensity and phase profiles of the Hermite-Gaussian modes up to l+m = 3. The profiles are labelled by the transverse mode indices in lm format.

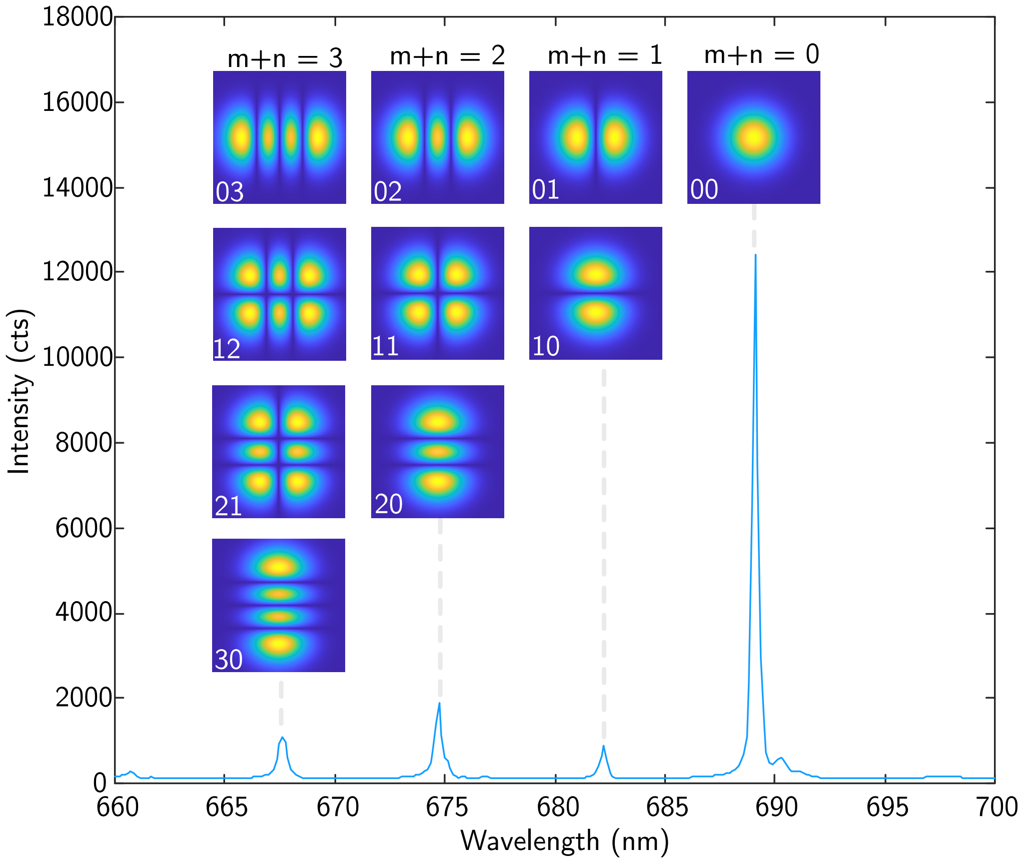

Figure 10: Optical spectrum of an NV centre coupled to a microcavity supporting multiple cavity modes. The broad emission of the NV PSB acts like a broadband photon source that is filtered by the higher-order cavity modes. The inset images show the possible Hermite-Gaussian mode profiles that can be associated with each peak for a constant longitudinal mode index q. For higher values of l+m, the peak may consist of multiple higher-order modes.

coupling between the cavity and the atom affects the emission of the cavity output, depending on the strength of the coupling. There are two possible coupling regimes which are strong coupling and weak coupling. The regime depends on the cavity photon decay rate κ, non resonant decay rate γ and the atom-photon coupling parameter g_0, which describe the losses and the gain within the cavity.

$$\text{Cavity photon decay rate}, \kappa = \frac{\omega}{Q} \tag{5.25}$$

$$\text{atom-photon coupling parameter, } g_0 = \frac{\mu_{12}^2 \omega}{2\epsilon_0 \hbar V_0} \tag{5.26}$$

Where ω is the frequency, Q is the quality factor of the cavity, μ_{12}^2 is the electric dipole matrix of the transition and V_0 mode volume. A high quality factor and small move volume are desired to minimise the cavity photon decay rate and maximise the atom-photon coupling strength. When $g_0 > (\kappa, \gamma)$, the photon emitted by the atom can be reabsorbed before leaving the cavity, which leads to strong coupling. When $g_0 < (\kappa, \gamma)$, the emitted photon leaves the cavity before it can be reabsorbed, leading to weak coupling. For the cavities used in this thesis, the cavity coupling interaction will be in the weak coupling regime. In the weak coupling regime, the cavity can enhance the photon emission of the atom via the Purcell effect. The Purcell effect can be used to enhance the photon emission of the NV centre, which is seen in Figure 10. The following sections will follow the approach by Fox[32] of deriving the spontaneous emission in free space and in the cavity before deriving the Purcell factor.

5.5 Free space spontaneous emission

Before considering the effect of the cavity on the emitter, the emission of the emitter in free space is discussed. The transition rate for spontaneous emission is given by Fermi's golden rule

$$\gamma = \frac{2\pi}{\hbar^2} |M_{12}|^2 g(\omega) \tag{5.27}$$

Where M_{12} is the transition matrix element and $g(\omega)$ is the density of states. For free space, the density of states is given as:

$$g(\omega) = \frac{\omega^2 V_0}{\pi^2 c^3} \tag{5.28}$$

The transition matrix element will consider the interaction of the electric dipole with the vacuum field $\mathcal{E}$ and averaging over all dipole directions.

$$M_{12}^2 = \frac{1}{3}\mu_{12}^2 \mathcal{E}_{vac}^2 = \frac{\mu_{12}^2 \hbar\omega}{6\epsilon_0 V_0} \tag{5.29}$$

Substituting Equations 5.29 and 5.28 into Equation 5.27 gives the free space spontaneous emission.

$$\gamma_{fs} = \frac{\mu_{12}^2 \omega^3}{3\pi\epsilon_0 \hbar c^3} \tag{5.30}$$

5.6 Cavity coupled emission

When the cavity is coupled to the emitter, the cavity modifies the density of states. The density of states is given as:

$$g(\omega)_{cavity} = \frac{2}{\pi\Delta\omega_c} \frac{\omega_c^2}{4(\omega-\omega_c)^2 + \omega_c^2} \tag{5.31}$$

Where $\Delta\omega_c$ is the cavity linewidth and ω_c is the cavity frequency. When the cavity is resonant to the emitter wavelength ($\omega = \omega_c$) the cavity density of states simplifies to:

$$g(\omega)_{cavity} = \frac{2}{\pi\Delta\omega_c} = \frac{2Q}{\pi\omega_0} \tag{5.32}$$

The transition matrix element within the cavity will be treated as:

$$M_{12}^2 = \xi^2 \mu_{12}^2 \mathcal{E}_{vac}^2 = \xi^2 \frac{\mu_{12}^2 \hbar\omega}{2\epsilon_0 V_0} \tag{5.33}$$

W here $\xi = \frac{|p.\mathcal{E}|}{|p||\mathcal{E}|}$ is the normalized dipole orientation factor. Substituting the cavity density of states (Equation 5.32) and transition matrix element (Equation 5.33) into Fermi's golden rule (Equation 5.27) gives the spontaneous emission rate within the cavity.

$$\gamma_{cavity} = \xi^2 \frac{2Q\mu_{12}^2}{\hbar\epsilon_0 V_0} \tag{5.34}$$

The Purcell factor is given by the ratio of the rate of spontaneous emission in the cavity over the rate of spontaneous emission in free space.

$$F_p = \frac{\gamma_{cavity}}{\gamma_{fs}} = \xi^2 \frac{3(\lambda/n)^3}{4\pi^2} \frac{Q}{V_0} \tag{5.35}$$

For a high Purcell factor, a high quality factor Q and a small mode volume is desired. From Equation 5.32, the cavity enhances the density of states of the resonant frequency whilst decreasing the density of states of the off resonant frequencies. For cavity coupling to the NV centre, the ZPL emission can be enhanced whilst suppressing the phonon sideband emission. A detailed model of this is shown by Johnson.[72]

5.7 Distributed Bragg Reflectors

High reflectivity is required in order to maximise cavity finesse and quality factor. Metallic mirrors offer at most $R = 95\%$ while Distributed Bragg Reflector (DBR) mirrors, also known as dielectric mirrors, can offer higher reflectivities of $R = 99.999\%$. DBR mirrors consist of pairs of thin films with a different refractive index and a thin film thickness of $\frac{\lambda}{4n}$. To explain how the reflectivity is determined, transfer matrices will be introduced.[112]

For a single layer thin film with a thickness l, the fields at each end of the film at $z = -l$ and $z = 0$ are described by the transfer matrix in Equation (5.36).

$$\begin{pmatrix} E_x(-l) \\ H_y(-l) \end{pmatrix} = \begin{pmatrix} cos(kl) & -(\frac{i}{n})sin(kl) \\ -(in)sin(kl) & cosk(kl) \end{pmatrix} \begin{pmatrix} E_x(0) \\ H_y(0) \end{pmatrix} \tag{5.36}$$

Where E_x and H_y are the electric and magnetic fields respectively, $k = \frac{2\pi}{\lambda}$ and n is the refractive index of the thin film. When considering an incoming wave entering at $z = -l$. Assuming there are no other losses such as absorption or scattering, there will be a fraction of the wave which will be reflected at $z = -l$ and there will be a transmitted fraction of the wave at $z = 0$.

$$\begin{pmatrix} 1+r \\ n_0(1-r) \end{pmatrix} = \begin{pmatrix} cos(kl) & -(\frac{i}{n})sin(kl) \\ -(in)sin(kl) & cosk(kl) \end{pmatrix} \begin{pmatrix} t \\ n_s t \end{pmatrix} \tag{5.37}$$

For DBR mirror layers, the thickness of each layer is set so that $kl = \frac{\pi}{2}$. This reduces the transfer matrix to.

$$\begin{pmatrix} 1+r \\ n_0(1-r) \end{pmatrix} = \begin{pmatrix} 0 & -(\frac{i}{n}) \\ -(in) & 0 \end{pmatrix} \begin{pmatrix} t \\ n_s t \end{pmatrix} \tag{5.38}$$

For the full DBR mirror composition which will consist of N pairs of layers with refractive indices n_1,n_2 the transfer matrix becomes

$$\begin{aligned} \begin{pmatrix} 1+r \\ n_0(1-r) \end{pmatrix} &= \left[\begin{pmatrix} 0 & -(\frac{i}{n_1}) \\ -(in_1) & 0 \end{pmatrix} \begin{pmatrix} 0 & -(\frac{i}{n_2}) \\ -(in_2) & 0 \end{pmatrix} \right]^N \begin{pmatrix} t \\ n_3 t \end{pmatrix} \\ &= \begin{pmatrix} -(\frac{n_3}{n_2})^N & 0 \\ 0 & -(\frac{n_2}{n_3})^N \end{pmatrix} \begin{pmatrix} t \\ n_s t \end{pmatrix} \end{aligned} \tag{5.39}$$

Solving for r

$$R = r^2 = \left[\frac{n_2^{2N} n_0 - n_s n_1^{2N}}{n_2^{2N} n_0 + n_s n_1^{2N}} \right]^2 \tag{5.40}$$

Where n_0 is the refractive index of the incoming light, n_1 and n_2 are the refractive indices for the thin film layers and n_s is the refractive index for the substrate.

The DBR mirror coatings that have been used for the experiments in this thesis use silicon dioxide SiO$_2$ and tantalum pentoxide Ta$_2$O$_5$ layers and $N = 10$ pairs for the planar mirrors and $N = 16$ pairs for the concave mirrors. The layer thickness was set so the mirror operates at $\lambda = 640$ nm so the thickness of the Ta$_2$O$_5$ layers is around $\frac{\lambda}{4n_{Ta_2O_5}} = 75\ nm$ and the thickness of the SiO$_2$ layers is around $\frac{\lambda}{4n_{SiO_2}} = 110\ nm$. The target reflectivities for the planar and concave mirrors were 99.8% and 99.9% respectively.

5.8 Aberration Theory

5.8.1 Introduction

Optical aberrations describe the deviation in the wavefront with respect to a reference wavefront, which is either a plane wave for a collimated beam or a spherical wave for a converging/ diverging light source. Aberrations will lead to imperfect focusing, where the spot size becomes larger than the diffraction-limited spot size. This will limit the confocal imaging resolution and single-mode fibre coupling efficiency. Common sources of aberrations include imperfect optics, optical misalignment and the sample that is being imaged.

For the optical microcavity, the focusing and collection through the planar mirror can introduce spherical aberration, which can be numerically described. This section will introduce how optical aberrations can be described by Zernike polynomials and show the theory of the spherical aberration introduced when focusing through a planar interface with a different refractive index.

5.8.2 Zernike Polynomials

These polynomials were derived by Fritz Zernike. These polynomials describe a set of orthogonal functions where each polynomial describes a different aberration. An optical wavefront ψ can be decomposed into a linear combination of Zernike polynomials Z_n^m.

$$\psi = \sum_i a_i Z_n^m \tag{5.41}$$

The Zernike polynomials are described by n and m which are integers representing the radial degree and the azimuthal degree respectively, and a_i is the coefficient of the Zernike polynomial. The Zernike polynomials with m=0 represent the radially symmetric aberrations. The equations

i	n	m	$Z(r,\theta)$	Aberration
1	0	0	1	Piston
2	1	1	$2rcos(\theta)$	Tip
3	1	-1	$2rsin(\theta)$	Tilt
4	2	0	$\sqrt{3}(2r^2-1)$	Defocus
5	2	2	$2\sqrt{3}r^2cos(2\theta)$	Oblique astigmatism
6	2	-2	$2\sqrt{3}r^2sin(2\theta)$	Vertical astigmatism
7	3	1	$2\sqrt{2}(3r^3-2r)cos(\theta)$	Coma x
8	3	-1	$2\sqrt{2}(3r^3-2r)sin(\theta)$	Coma y
9	3	3	$2\sqrt{2}r^3cos(3\theta)$	Trefoil x
10	3	-3	$2\sqrt{2}r^3sin(3\theta)$	Trefoil y
11	4	0	$\sqrt{5}(6r^4-6r^2+1)$	Primary spherical
12	4	2	$\sqrt{10}(4r^4-3r^2)cos(2\theta)$	Secondary astigmatism x
13	4	-2	$\sqrt{10}(4r^4-3r^2)sin(2\theta)$	Secondary astigmatism y

Table 1: List of the first 13 Zernike polynomials and the name of the aberration they represent. The column i represents the respective Noll index associated with the Zernike polynomial.

of the first 13 Zernike polynomials are shown in Table 1.

$$Z_n^m(r,\theta) = \begin{cases} R_n^m(r)\cos(m\theta) \text{ even} \\ \\ R_n^m(r)\sin(m\theta) \text{ odd} \end{cases} \tag{5.42}$$

$$R_n^m = \begin{cases} \sum_{l=0}^{\frac{n-m}{2}} \dfrac{(-1)^l(n-l)!}{l!\left(\dfrac{n+m}{2}-l\right)!\left(\frac{n-m}{2}-l\right)!} r^{n-2l} \end{cases} \tag{5.43}$$

The effects of how these aberrations change the focused spot are shown in Figure 11. The aberrations changes the spot shape and intensity distribution of spot. When refocusing aberrated light into single-mode fibres, there will be losses in coupling efficiency due to the mismatch between the spot size and the fibre core, resulting in less intensity being collected by the fibre. This thesis will use Zernike polynomials in the experiments by applying the polynomials, using adaptive optics, to the wavefront of light collected from the emitter and finding the polynomials that maximise the collected intensity. The aberrations associated with these Zernike polynomials can be used to describe the aberrations in the sample. The Zernike

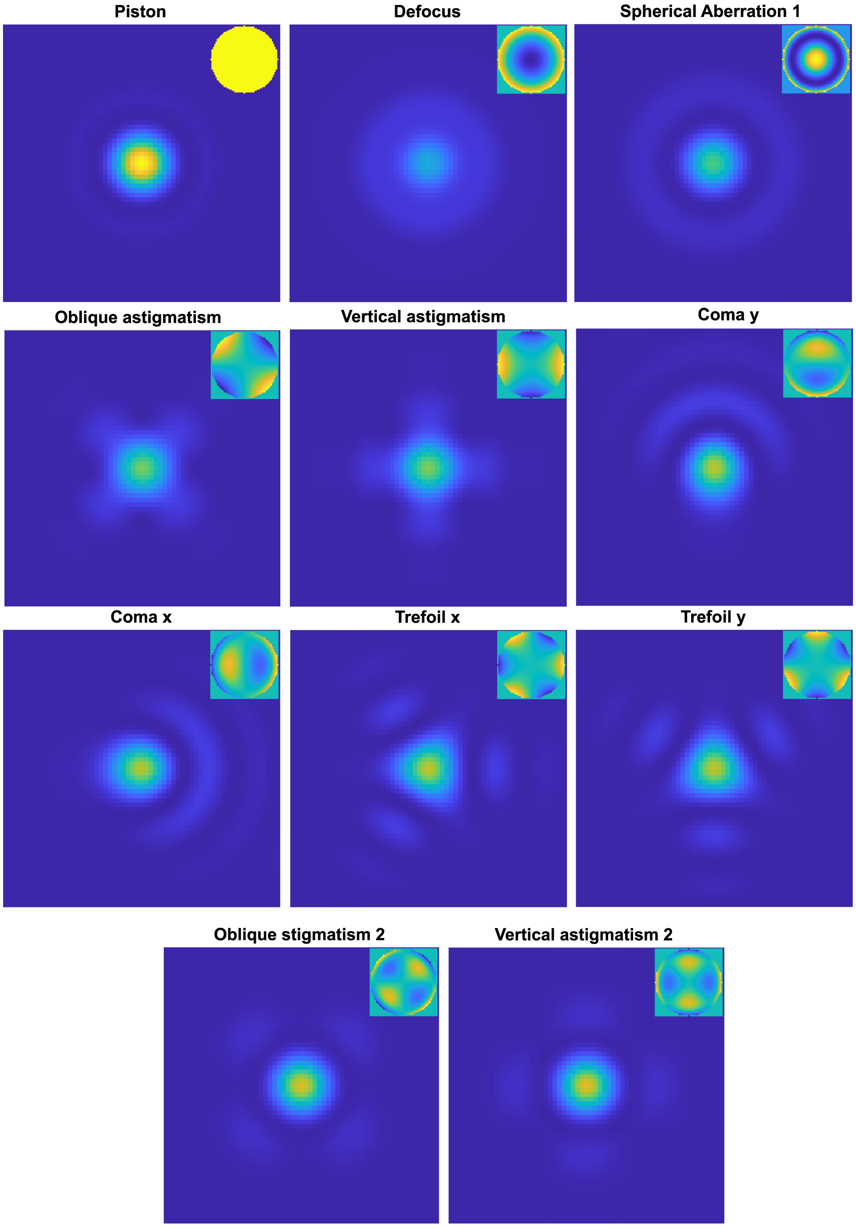

Figure 11: Point spread function of focused laser beam under the affect of each aberration listed in table 1 along with the phase profile of the aberration in the inset. The amplitude of aberration applied is $+\lambda/4$ waves and the plots are normalised to the maximum intensity of a diffraction-limited spot.

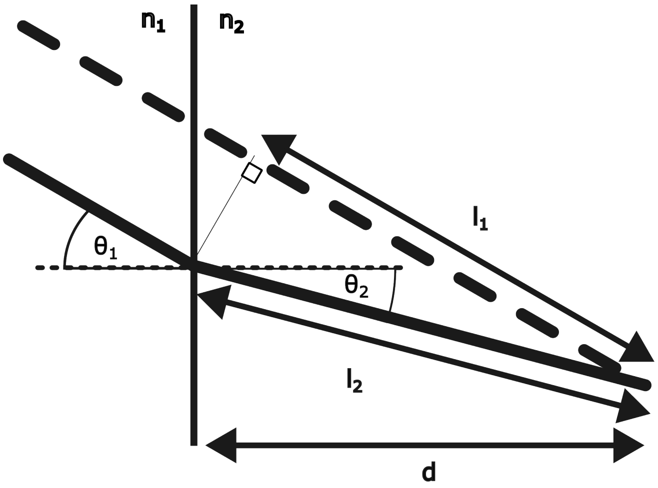

Figure 12: Schematic of ray path change when focusing with only the focusing medium n_1 against focusing in a different medium n_2. d is the length from the refractive mismatch interface to the point of focus.

polynomials will also be used in the theory to decompose the wavefront errors modelled in the later chapters to find which aberrations are associated.

5.8.3 Aberration function focusing through a planar interface

One of the major aberrations in microscopy is introduced when focusing into a sample with a refractive index n_2 that differs from the refractive index of the initial focusing medium n_1. This is illustrated in Figure 12, where a refractive index mismatch causes a phase change when focusing to the same point, which deforms the wavefront. The derivation of the spherical aberration equation follows the derivation by Booth.[113] The aberration function can be derived by taking the difference in the pathlength taken when the ray is focusing through the focusing medium l_1 and the pathlength when the ray is focusing in the sample medium l_2.

$$\Psi = k(n_2 l_2 - n_1 l_1) \tag{5.44}$$

Using Snell's law and the geometry in Figure 12, Equation 5.44 can rearranged to Equation 5.46

$$n_1 sin(\theta_1) = n_2 sin(\theta_2) \tag{5.45}$$

$$\Psi = kd(n_2 cos(\theta_2) - n_1 cos(\theta_1)) \tag{5.46}$$

Assuming that the lens operated under the sine condition and introducing a normalised radius $r = \sin(\theta)/\sin(\alpha_1)$, where α_1 is the maximum angle defined by the NA of the lens $NA = n_1 \sin(\alpha_1)$, the path difference can be further rearranged to form Equation 5.47.

$$\Psi(d, r) = k\, NA\, d \left(\sqrt{\csc^2 a_2 - r^2} - \sqrt{\csc^2 a_1 - r^2}\right) \tag{5.47}$$

Where α_2 is the maximum angle for the ray in the medium n_2.

Equation 5.47 can be used to model the collection losses when collecting light from an emitter in bulk diamond. For a confocal microscope, when light is collected from the emitter, the light gets refocused into an optical fibre, which acts like a pinhole, to couple the light to a photon detector. The refocused intensity profile can be numerically modelled by taking the Fourier transform of the pupil function Ψ to get the point spread function and by multiplying the point spread function by its conjugate. In this case, the pupil function will be the aberration function.

$$I = \left| \int_0^1 e^{i\Psi(d,r)}\, dr \right|^2 \tag{5.48}$$

To include the effect of the pinhole, the total intensity is integrated over the same area as the diffraction-limited spot with zero aberration ($\psi = 0$) and normalised over the total intensity of the diffraction-limited spot.

Figure 13 shows the collected intensity from an emitter in diamond at different depths. For deeper emitters, the losses become significant. SILs can be used to ensure light exits the diamond surface at normal incidence, so no aberration is introduced by the diamond/air interface. For focusing through multiple layers of mismatching refractive indices n_i, this can

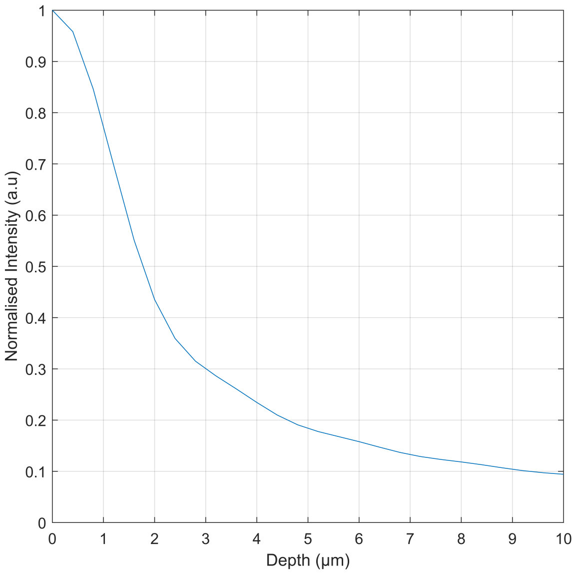

Figure 13: Normalised intensity profile of collected light, when collecting light from an emitter in the diamond. For the calculation, the numerical aperture used is $NA = 0.82$, the refractive index used are $n_1 = 1$ and $n_2 = 2.4$ and the wavelength used is $\lambda = 640\ nm$

be further extended to Equation 5.49.

$$\Psi(d, r) = k\, NA \sum_{i=1}^{I} d_i \left(\sqrt{\csc^2 a_i - r^2} - \sqrt{\csc^2 a_1 - r^2} \right) \tag{5.49}$$

Where α_i is the maximum angle for the ray in the medium n_i. This model can be used to describe the spherical aberration introduced when collecting light through the planar mirror of the microcavity. The aberrated wavefront can then be decomposed into Zernike polynomials to describe which aberrations are introduced by the microcavity

6 Experimental Methods

6.1 Adaptive Optics

Adaptive optic technologies involve the use of a device that can actively modify the phase profile of an incoming wavefront such as Spatial Light Modulators, Adaptive Lenses or Deformable Mirrors (DM) with the latter being used in this thesis. Compared to spatial light modulators, DMs have the advantage of wavelength independent operation, as the phase change introduced by the DM is independent of the wavelength of light.

The multi-3.5 DM has a 12x12 actuator grid with a pixel size of 400 μm and 3.5 μm actuator stroke. A schematic and image of the DM grid are shown in Figure 14a and b respectively. The individual actuator pushes/pulls the mirror surface locally to form a pattern on the mirror. The local mirror deformation will create a local phase difference when light is reflected off the mirror. Surface profiles that represent the Zernike polynomials can be applied to the DM to alter the wavefront of the light collected from the objective lens.

The outer pixels on the edges of the grids have limited movement because they are coupled to the fixed actuators on the edge of the grid, so they are not used. This is shown in Figure 14c, where the area within the circle is the effective area of the back aperture of the objective lens that is exposed on the DM. The actuator grid size will limit the ability to map out the higher-order polynomials, which will have features smaller than the grid size. For the experiments in this thesis, the Zernike polynomials with $n<5$ will be used.

6.2 Laser Scanning Confocal Microscopy

All the experiments were performed on custom laser scanning confocal microscopes. Confocal microscopy has the advantage of achieving higher resolution than widefield microscopy. This is achieved by placing a pinhole on the detection path to ensure that the collected light beam is concentric with the excitation path. The pinhole also serves the purpose of collecting light only within the focal plane and rejecting light that is out of focus. The confocal spot is rastered

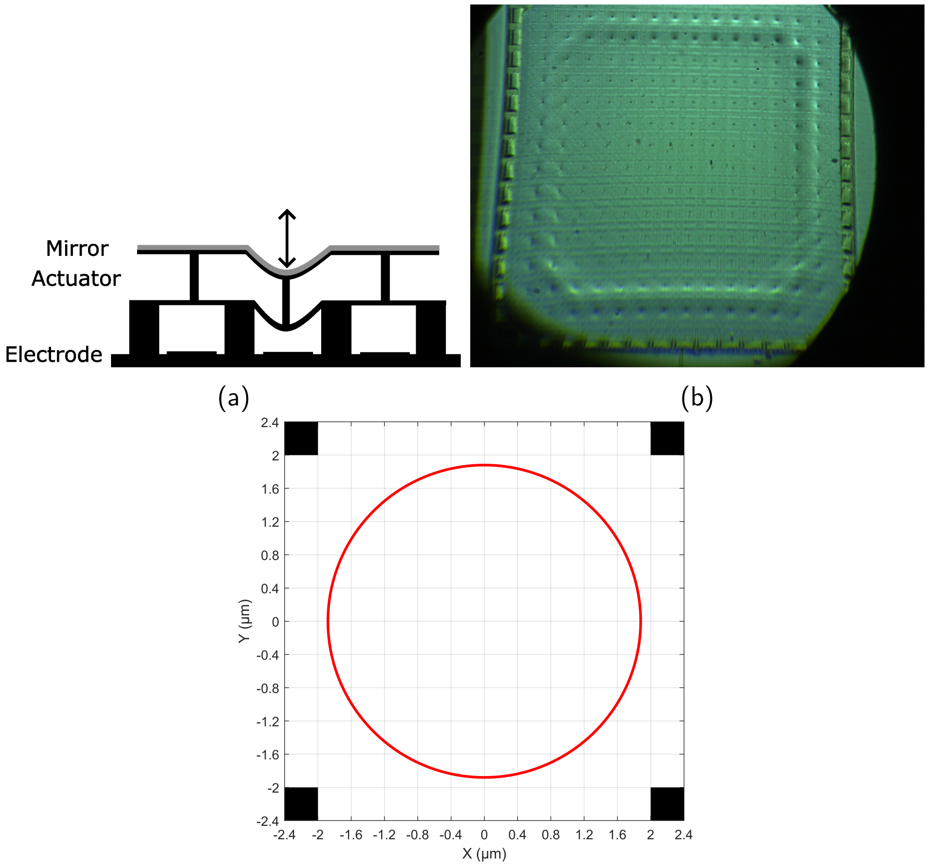

(a) (b)

(c)

Figure 14: (a) Schematic of the deformable mirror, (b) optical image of the Boston Micromachines Multi-3.5-DM and (c) graphic of the actuator grid of the DM. Schematic reproduced from source [114]. Dark pixels represent inactive actuators and the circle represents the active area being used. The red circle is the effective back aperture of the objective lens that is exposed on the DM. The effective diameter is 3.76 mm.

across the sample using a scanning mirror to build up the 2D image.

The resolution of the confocal microscope is defined by the excitation wavelength and the numerical aperture of the lens.

$$\text{Resolution} = \frac{0.51 \times \lambda_{ex}}{NA} \tag{6.1}$$

The optical setup of the confocal microscope is shown in Figure 15 and is separated into three sections. Section A contains the optics for the excitation laser beam delivery and light collection, Section B contains the optics for the deformable mirror and relay optics and Section C contains the optics for the confocal beam scanning and widefield imaging of the microcavity. The optics for Section B were implemented by me.

A continuous 532 nm laser (Cobolt Samba) is used to excite the sample off resonance and is delivered to the system through a single-mode fibre (SM450). On the confocal system, the beam is collimated using an objective lens and is deflected off a dichroic mirror (Semrock FF580-FDi02-t3-25x36) towards the deformable mirror (Boston Micromachines Multi-3.5-DM). A 5 mm dichroic mirror thickness was selected to reduce the reflected wavefront error of the beam. After the deformable mirror, there is a relay lens setup ($2f_a - 2f_b$ configuration, $f_a = 80$ mm, $f_b = 100$ mm) between the beam path of the deformable mirror and the scanning mirror (Newport FSM300). This relay lens has the dual purpose of making sure the phase profile is mapped onto the scanning mirror and expanding the beam to fill the back aperture of the objective lens. The alignment between the DM and FSM is set in a 4f configuration, making the DM and FSM conjugate to each other as shown in Figure 16.

Another relay lens ($4f$ configuration, $f = 275mm$) is placed between the path of the scanning mirror and the back focal plane of the objective lens (Attocube LTAPO - UV VIS). This ensures that the deflection off the steering mirror is mapped onto the back aperture of the objective lens, which will then correspond to lateral displacement on the focal plane of the sample. For fluorescence emission, the confocal microscope is configured in an epifluorescent

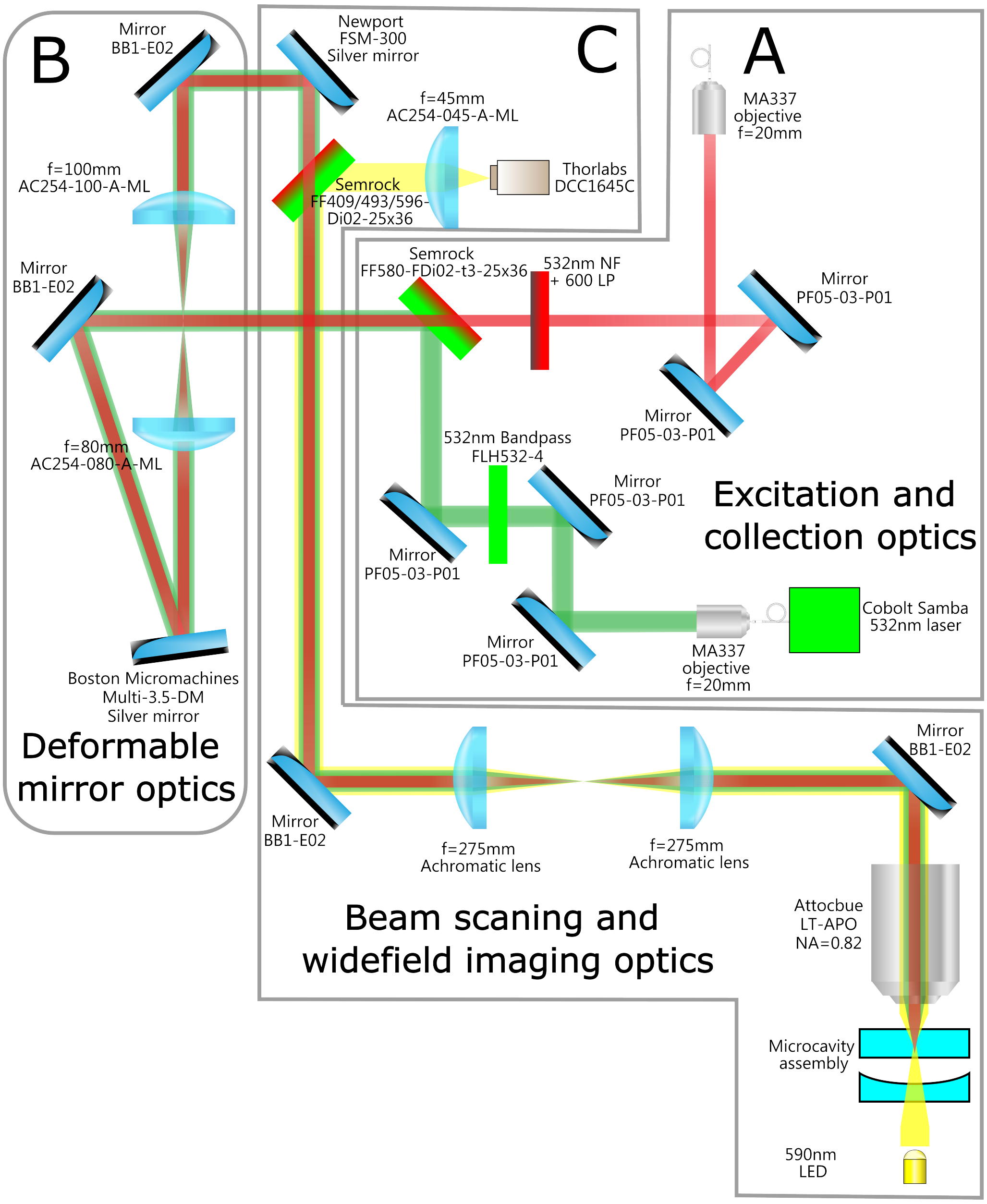

Figure 15: Optical layout of the confocal imaging system using a Deformable Mirror. Figure produced by Amit Dhawan.

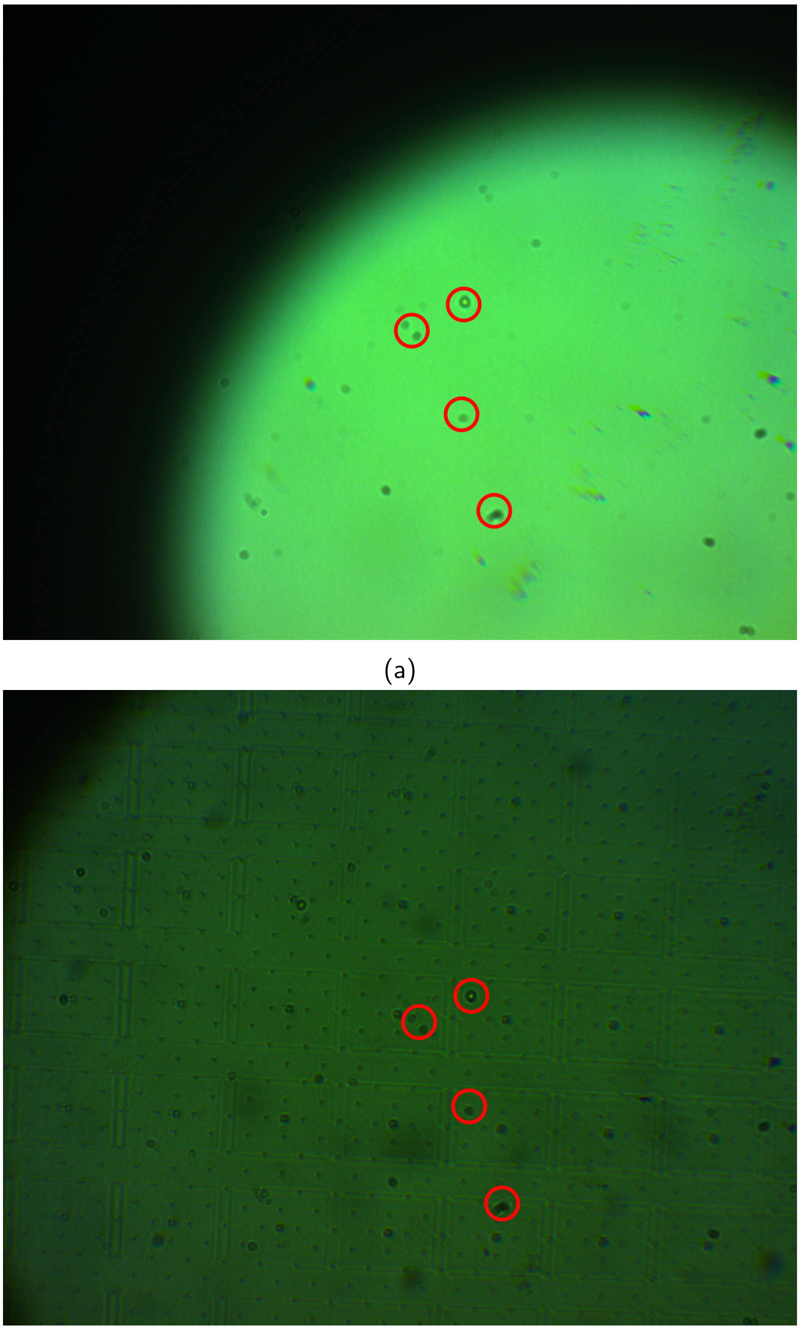

(a)

(b)

Figure 16: Optical images of the FSM(a) and the DM conjugate to the FSM (b). Some of the features on the FSM circled in red can be seen when imaging the DM if the FSM and the DM are conjugate to each other and both are illuminated.

configuration, where the light is collected from the same objective lens as the excitation light. The collected light travels back through the system but is instead transmitted through both dichroic mirrors. There are additional collection filters: a 532 nm notch filter, a 560 nm long pass for further attenuation of the excitation light before the collected light is focused into a single-mode fibre (SM600), which goes towards a Single Photon Avalanche Detector (Excelitas SPCM-AQRH-14-FC).

6.3 Cavity Coupling Assembly

For the fine alignment and coupling of the cavity to the NV centre, the mirrors are mounted on an 8-axis piezo stack consisting of attocube nanopositioners, shown in Figure 17. The three base positioners (2x ANPx101, 1x ANPz101) provide positioning of the whole assembly and for sample positioning of the planar mirror. The five remaining nanopositioners (2x ANPx51 ANPz51 ANGt101, ANGp101) provide five degrees of control (x, y, z, θ, ϕ) for the concave mirror with respect to the planar mirror for both room temperature and low temperature operation.

The cavity mirrors are made by coating UV-fused silica (UQG CFS-1020) with DBR mirror coatings, which are outsourced to NANEO and LAYERTEC. The concave mirrors were prepared by dicing the substrate into 3 mm x 3 mm squares with a 0.3 mm x 0.3 mm elevation of 0.1 mm in the centre. The concave features are then milled using focus ion beam milling (FEI FIB200). The cavity milling was performed by Jiangrui Qian. An image of the concave mirror array is shown in Figure 17. The concave mirrors milled had radii of curvatures of 4 μm, 8 μm, 12 μm. 25 μm with cavity depths of 300 μm and 600 μm.

Grid marks were also FIB milled on the planar mirror to provide a reference for navigating and imaging the defects. The planar mirrors exhibited strong autofluorescence, likely due to oxygen deficiencies in the tantalum pentoxide layer of the DBR mirror.[115,116] The autofluorescence could be reduced by irradiating the surface with a focused 532 nm laser at high power (100 mW). The NV samples used for cavity coupling were 100 nm diamond nanoparticles containing

100s of NVs (FND biotech), which were spin-coated onto the planar mirror. The cavity coupling process begins with finding the nanodiamonds on the planar mirror using confocal imaging of the planar mirror face up. The mirror is then flipped face down, and the same nanodiamonds image that was seen when the mirror was face up is navigated to. When those nanodiamonds are found, the concave mirror is elevated and centred around the emitter to couple and close the cavity around.

The wedge angle between the mirrors is minimised by minimising the number of fringes seen on the webcam when illuminated by the LED beneath the concave mirror. The cavity modes are then tuned by looking at the cavity modes formed on the spectrometer and minimising the transverse mode peaks through x-y translation of the concave mirror.

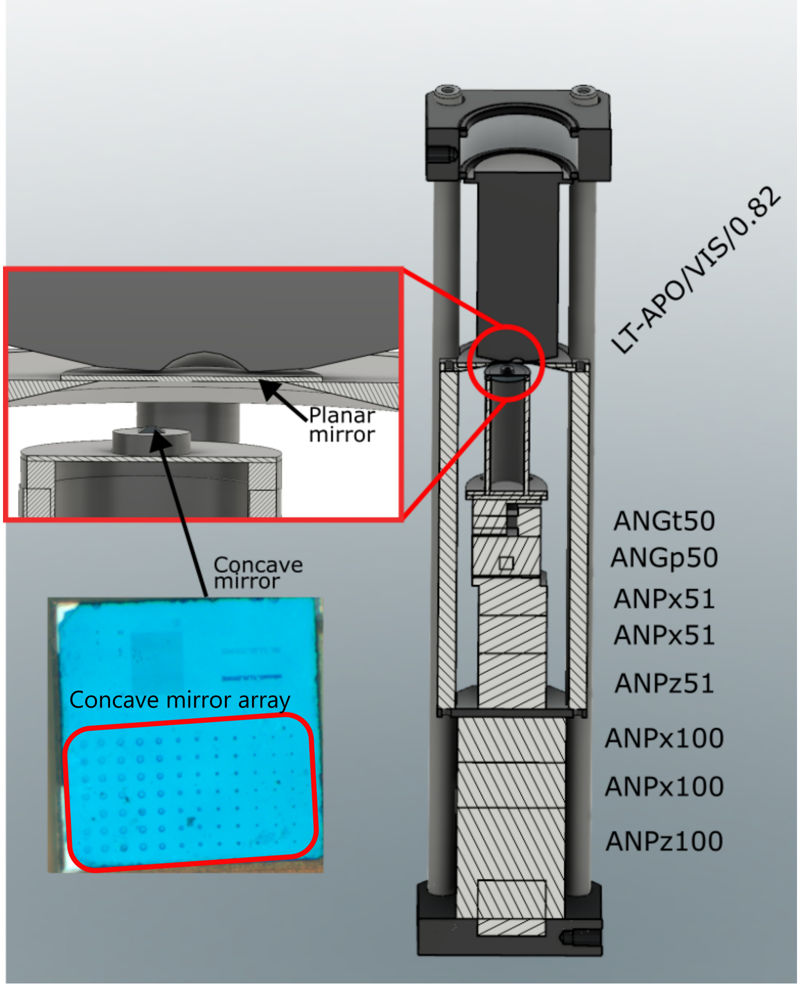

Figure 17: CAD schematic of the cavity coupling assembly with the attocube piezo labelled and the objective lens. Insert image of zoomed-in area of the mirror cavity region and an image of the concave mirror array plinth. The assembly allows for remote in situ alignment of the concave mirror for cavity coupling and tuning.

6.4 Cavity Fringe Stabilisation

In this thesis, the cavity is stabilised by locking the phase of the interference fringes that are introduced within the cavity. The fringes are formed by illuminating a wedge between the cavity mirrors with an LED as shown in Figure 18a. The illumination by the LED will form interference fringes between the planar faces of the mirrors. Any drift in the cavity length will lead to the fringe position shifting as shown in Figure 18b. By monitoring the position and phase of the

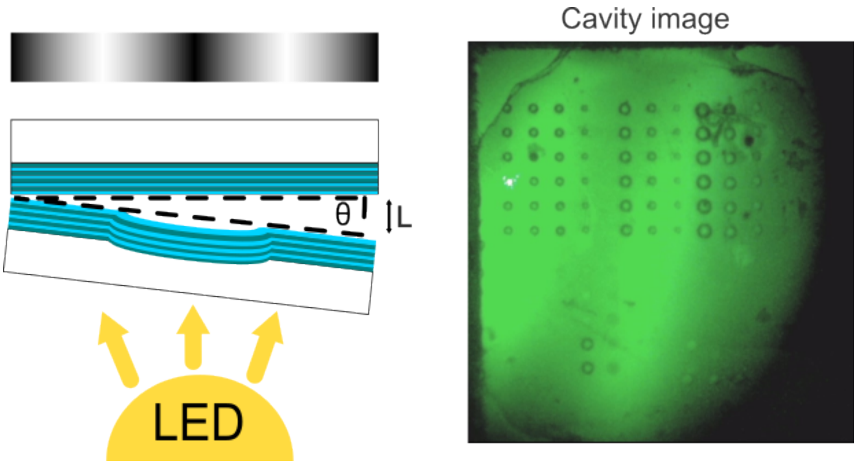

Figure 18: a) Schematic of the the fringe formation in the cavity. The wedge angle in the cavity produces interference fringes in transmission when the cavity is illuminated. b) Cavity image showing 2 fringes formed from the wedge interference. The red arrow shows the direction of fringe movement when the cavity length changes.

fringes and locking them, the cavity length can be locked. The fringe phase position and error are monitored with a webcam and PID feedback is applied to the piezo to maintain the cavity length. A dichroic mirror (Semrock FF409/493/596-Di02-25x36) was used to reflect as much of the fringe light as possible into the webcam, while allowing transmission of the excitation and fluorescence. The phase error can also be used to monitor the drift of the cavity length. This will be used to monitor the drift when MW power is delivered to the cavity.

The number of fringes is controlled by the wedge angle and there will be a trade off between the number of fringes to ensure better phase locking and the shortest cavity length possible. For these experiments, 2-3 fringes were used. This program was developed by Dr William Okell and was adapted by me to communicate with the Keithley 2400 voltage source. The cavity is illuminated with a 590 nm LED, which is placed beneath the concave mirror and the feedback is given to the ANPz51 piezo to control the cavity length. To provide feedback, a Keithley 2400 voltage source was used to supply a voltage to the Attocube ANC 300 controller with the ANM300 module through the DC-in port. The built-in short-pass filter in the attocube controller was used to prevent any high-frequency noise from being fed into the piezo, which would cause the cavity length to oscillate.

6.5 Power Saturation measurement

The power saturation measurement measures the collected intensity with respect to excitation power and is described in Equation 6.2.

$$I = \frac{I_{sat}P}{P + P_{sat}} + bP + c \tag{6.2}$$

Where I_{sat} is the saturation intensity and P_{sat} is the saturation power. There is also a linear background contribution described by the coefficient b, which could be contributed from autofluorescence from the DBR mirror coatings, the mirror substrates and from the bulk material of the diamond. There is also a background signal from the dark counts of the photodetector when no laser power is applied, which is accounted for by the constant c.

The power saturation measurement will be used to characterise the improvement in collection efficiency when aberration correction is applied. As the DM is configured to affect both excitation and collection, the power saturation measurement can help differentiate the contributions, where increases in saturation intensity would correspond to an improvement in collection efficiency, whilst a decrease in saturation power indicates an increase in excitation efficiency.

6.6 Hanbury Brown Twiss measurement

The Hanbury Brown and Twiss (HBT) measurement is used to determine if the light collected from the focal region of the objective lens is from a single emitter. This is used to find single NV centres for fabricating monolithic SILs. A schematic of an HBT setup is shown in Figure 19. The emission from the emitter is split between two detectors and the time difference of photon detection events between both detectors is logged as a histogram. The data can be described by the second-order correlation function:

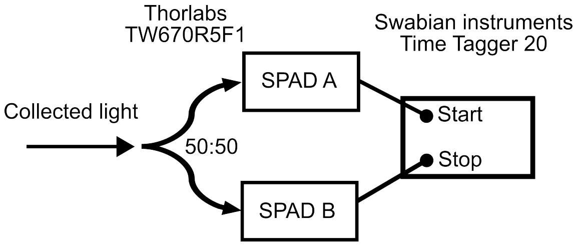

Figure 19: Schematic of the HBT measurement used. The collected light is split by a fibre beam splitter and coupled to two single-photon counting modules. The photon detection is then logged by a time tagger, which will measure and log the time difference between detection from both detectors.

$$g^{(2)}(\tau) = \frac{\langle I_A(t) I_B(t+\tau)\rangle}{\langle I_A(t)\rangle \langle I_B(t_\tau)\rangle} \tag{6.3}$$

Where $\langle ... \rangle$ represents the time average over t, I_A and I_B represent the count rate at detectors A and B, τ is the time delay between both detectors. The denominator can also be expressed as:

$$\langle I_A(t)\rangle \langle I_B(t_\tau)\rangle = I_A \cdot I_B \cdot \delta t \cdot t_{total} \tag{6.4}$$

Where I_1 and I_2 represent the average count rate on detectors A and B respectively, δt is the time bin used and t_{total} is the total measurement time. The NV centre can be treated as a three-level system and so the second-order correlation function can be treated as[117]:

$$g^{(2)}(\tau) = 1 + c_1 e^{\frac{\tau}{\tau_1}} + c_2 e^{\frac{\tau}{\tau_2}} \tag{6.5}$$

Where τ_1 and τ_2 are the radiative lifetimes of the exited and metastable states respectively, and c_1 and c_2 are coefficients.

When the intensity of a single NV centre is collected, it is expected that the second-order correlation function evaluated at zero time delay will be zero ($g^{(2)}(0) = 0$) and when evaluated at higher time delays, the correlation will converge towards 1. However in the experiments, there is a background signal that is also collected so $g^{(2)}(0) > 0$. To correct the $g^{(2)}(\tau)$ function from the background. The background signal can be measured by measuring the intensity of an area adjacent to the emitter to determine a baseline.[59]

$$a = 1 - \frac{S}{S+B} \tag{6.6}$$

Where S and B are the count rates for the signal and background respectively. This baseline can then be used to correct the correlation function:

$$g^{(2)}(\tau) = \frac{g^{(2)_{raw}(\tau)} - a}{1-a} \tag{6.7}$$

6.7 Optically Detected Magnetic Resonance

Optically Detected Magnetic Resonance (ODMR) is a method to characterise the spin transitions of the NV states. The m$_s$=0 $\rightleftharpoons$ m$_s$ $= \pm 1$ transition occurs around 2.88 GHz. When a microwave field that is resonant with this transition is delivered to the NV centre and is optically excited, there will be a relative reduction in intensity compared to when the microwave field is off resonant. The reduction in intensity is due to the inter-system crossing of the excited m$_s$ $= \pm 1$ state that becomes populated from the microwave field.

The ODMR performed in this thesis is used to test the cavity locking scheme implemented for spin control. A coaxial trace loop antenna was used to deliver the microwave field to the NV centre and an image of the design is shown in Figure 20a. The loop antenna provides a compact solution to delivering the microwaves without interfering with optical access. The NV centres that were within the grid pattern are used for cavity coupling. The distance between the loop antenna and the NV centre within the grids ranges from 225 µm to 318 µm as shown in Figure 20b. The antenna is mounted on the planar mirror and the designs were made by Sam Johnson.

The schematic of the ODMR setup is shown in Figure 21a and the position of the loop antenna within the microcavity assembly is shown in Figure 21b. A R&S SGS100A was used

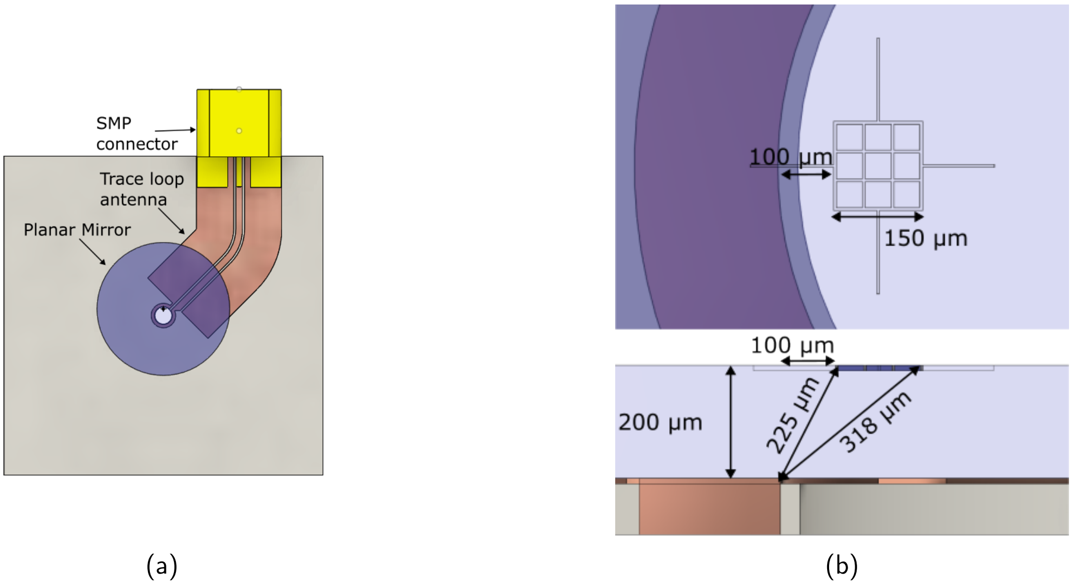

(a) (b)

Figure 20: Schematic of the PCB trace loop antenna with the planar mirror on top and a zoomed in image of the patterned grid on the mirror The PCB is made with Rogers 4350B and interfaced with a 50 Ω SMP PCB connector. The loop was designed with a 1.6 mm diameter and 0.5 mm loop thickness.

as the MW source which is amplified using a amplifier (Amplifier Research 20S1G4). A flexible coaxial cable (Thorlabs SMGF6) was used as the final connection to the loop antenna. Flexibility of the cable was necessary to allow free movement of the piezo assembly. This cable was sufficient for room temperature experiments but not for low temperature measurements in the dewar, where there is less space in the chamber for the wire to move and would be too rigid, obstructing piezo movement. A cryogenic ribbon cable (Delft Circuits, Cri/oFlex 1) was purchased to enable low temperature MW delivery without constraining piezo movement.

6.8 Photoluminescence Excitation Spectroscopy

This measurement of the NV ZPL linewidth involves sweeping the laser frequency through the ZPL of the NV centre and measuring the collected intensity of the emission. This is used in Chapter 7 to measure the ZPL linewidths of the NVs formed by MHz laser diffusion. The NV is exposed to the 637 nm tunable laser and the wavelength of the laser is swept. When

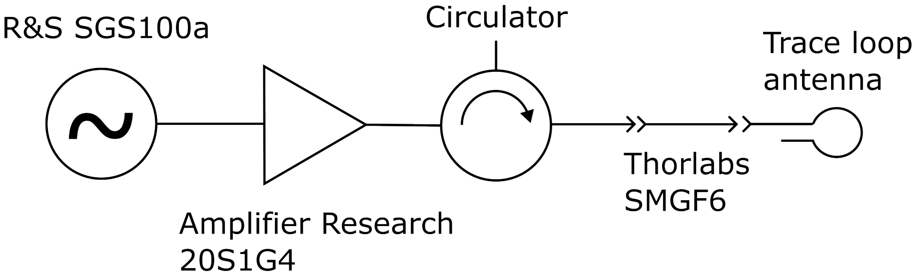

(a)

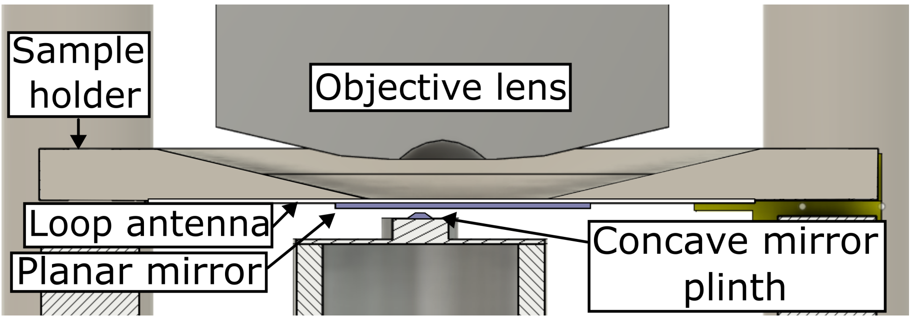

(b)

Figure 21: a) Electrical schematic of the ODMR system. All connections between each device were made using SMA cables except for the semi-rigid cable (Thorlabs SMGF6). b) Schematic of the microcavity assembly with the loop antenna.

the laser wavelength matches the NV ZPL wavelength, the NV becomes excited and will emit light. The photons from the NV PSB are collected. By recording the PSB photons with respect to the wavelength of the laser, the spectrum of the NV ZPL can be acquired. This method offers a spectral resolution limited by the linewidth of the laser(<200 kHz) in contrast to a spectrometer, which is limited to tens of gigahertz which is insufficient to measure the transform-limited linewidth (13 MHz). It is also possible to measure the ZPL by measuring the transmission of the ZPL emission through a scanning Fabry-Pérot interferometer; however, this approach would incur high losses due to mode matching to the Fabry-Pérot cavity, which would slow down the measurement.[118]

The layout for the measurement is shown in Figure 22. A Newport tunable laser (TLB-6704) was used for the resonant excitation sweeping and a 532 nm laser (Laser quantum Gem 532) was used for off resonant excitation and for resetting the charge state of the NV centre ($NV^0 \Rightarrow NV^-$). The frequency was swept by applying a triangle voltage to the laser piezo using a 16-bit DAQ (PCIe-6321) and the photon counts of the NV PSB were measured in the same sequence. The frequency was measured using a wavemeter (HighFinesse WSU-30). The measurements were performed using a lab-built confocal microscope coupled to a Montana Instruments Cryostation s50 cryostat with a Zeizz (EC Epiplan-Neofluar 100x/0.90 BD DIC M27) objective lens. The implementation of the 637 nm excitation optics and software control was developed by me.

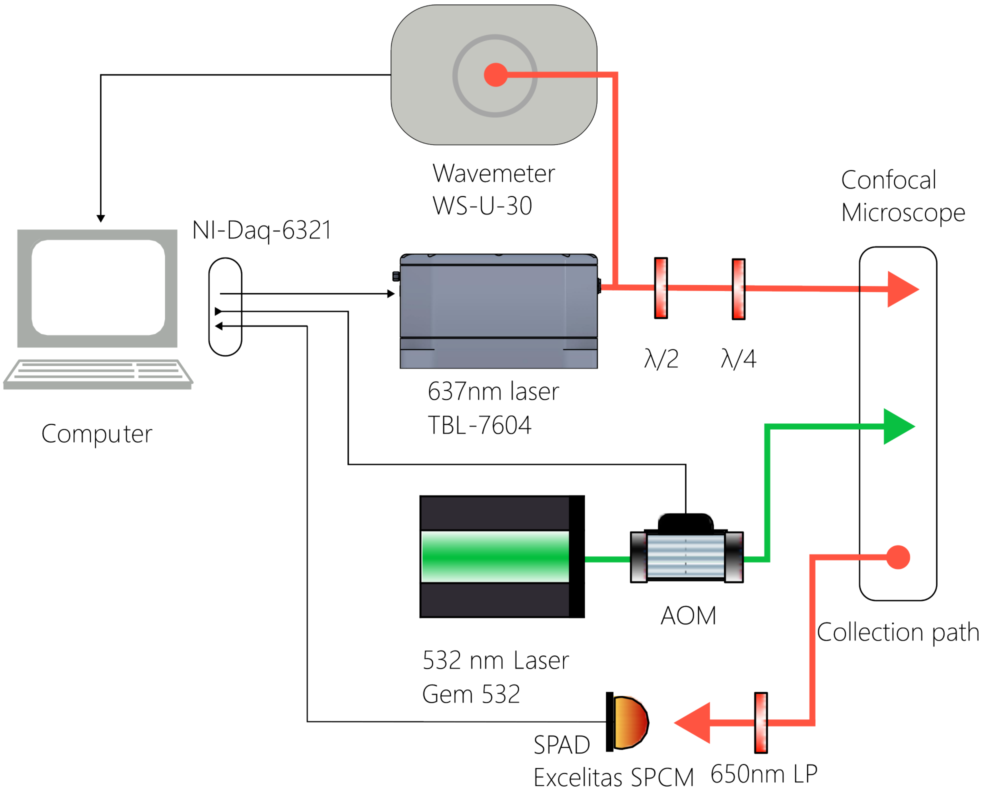

Figure 22: Schematic of the photoluminescence spectroscopy setup. The thin lines represent wired connections and the thick coloured lines represent optical paths. The optical paths going towards the confocal microscope are fibre-coupled to deliver the optics through optical fibres. The 637 nm optics, SPAD collection optics and hardware control/data acquisition programming were developed by me. The 532 nm laser optics was aligned by Gareth Jones. Some of the graphics used are from the ComponentLibrary by Alexander Franzen.

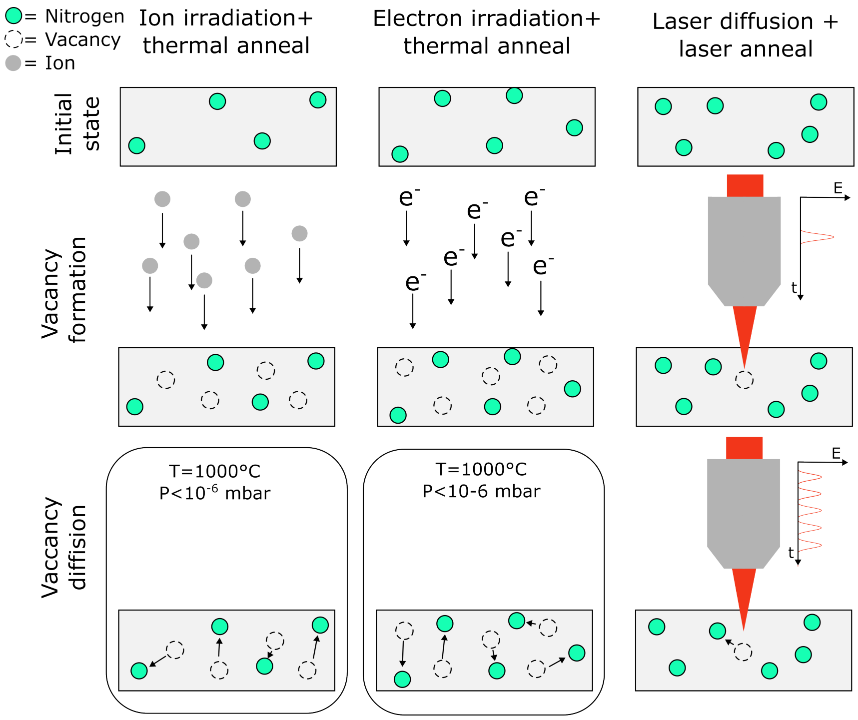

Figure 23: Diagram of NV fabrication procedures using ion/electron irradiation with thermal anneal and laser writing and diffusion. The laser writing process for vacancy generation involves applying a single pulse to generate the vacancy and the diffusion process involves applying multiple laser pulses with a lower power than the vacancy generation pulse to diffuse the vacancy to a local nitrogen atom.

7 Photoluminescence spectroscopy of the MHz diffused NV centres

7.1 Introduction

The laser writing and diffusion process of vacancies in diamond to form NV centres offers a deterministic NV formation process and a stand-alone process in contrast to other methods where the vacancy formation and diffusion processes are operated on different instruments. A diagram of NV fabrication using Ion implantation with thermal annealing, electron irradiation with thermal annealing, and laser writing with laser diffusion is presented in Figure 23. Laser writing and diffusion have previously been demonstrated in HPHT diamond (1.8 ppm nitrogen concentration), where single NV emitters could be generated with a near 96% yield using a kHz repetition rate laser.[59] However, the NVs formed have undesirable ZPL linewidths, which are likely due to the high nitrogen concentration of the sample. This leads to the motivation for performing laser writing and diffusion in electronic-grade diamond (ppb nitrogen concentration) to produce NV centres with narrow ZPL linewidths suitable for quantum applications. In recent developments, laser-written NV centres have been fabricated in electronic-grade diamond. In this chapter, Photoluminescence electron (PLE) spectroscopy as described in Section 6.8 is used to characterise these laser-written NVs and the results are presented.

7.2 Results

The NV fabrication in the electronic-grade diamond was performed by Andrew Kirkpatrick and the PLE characterisation was performed by me. NV centres were formed around 20 µm deep from the surface of an electronic-grade diamond (Element 6) using a 520 nm, 280 fs pulsed laser with a 1 MHz repetition rate. Figure 24 shows the confocal images of two sites A and B with formed NV centres. From these sites, 15 NV centres were visible using the cryostat confocal microscope. Out of the 15 NVs, 6 NVs showed ZPL peaks during the PLE scans, which have been labelled. Figure 25 a and b shows a single PLE linewidth scan of NV centres B3 and B6

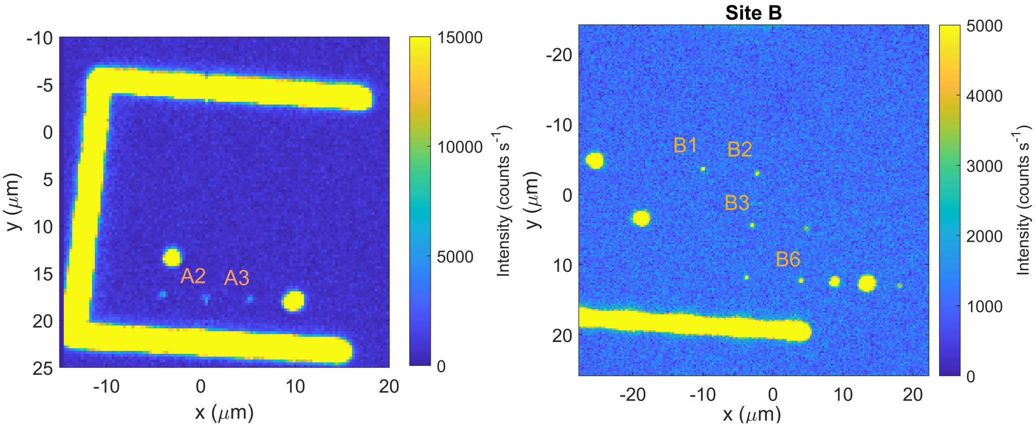

Figure 24: Confocal images of laser-diffused NVs in sites A and B. The NVs that showed peaks in the PLE scans are labelled.

respectively with a Voigt peak fitted to find the single scan linewidth of the ZPL.[119] Both the PLE single scans show a <100 MHz single scan ZPL linewidth. The average linewidth of the single scan linewidths from each PLE scan of B3 and B6 was 34.2±1.0 MHz and 113.0±1.9 MHz respectively. The average linewidths of all the NV centres that were characterised are shown in the histogram in Figure 25c.

Over several scans of the ZPL linewidth, the ZPL peak position can drift due to the local charge environment.[40] This is shown in Figure 26a for the B3 NV centre. For each PLE sweep that showed a ZPL peak, the ZPL position changes. To characterise the extent of the drift of the ZPL position, all of the single PLE sweep scans of that NV centre can be added together and the peak can be fitted to characterise the spectral broadening of the ZPL. The summation of the single PLE scans for NV centre B3 is shown in Figure 26b with a fitted linewidth. This linewidth will be referred as the total linewidth. The total linewidths of the NVs that showed ZPL peaks are also shown in Figure 26c. The total linewidths of the NVs found in site B are narrower than those found in site A. To check if the narrowest ZPL linewidth scans (B3) were affected by power broadening, a power saturation curve was fitted to the average linewidth as a function of objective power. The trend was fitted with $\gamma = \gamma_0\sqrt{1 + P/P_{sat}}$ where γ is the linewidth, γ_0 is the natural linewidth, P is the objective power and P$_{sat}$ is the saturation power.[120] The power broadening is a result of the non-perturbative solution for the population of the excited state. The linewidth for the excited state as a function of excitation frequency is equal to $2\sqrt{\gamma_0^2 + \Omega^2}$ where Ω is the Rabi frequency, which is proportional to excitation power.[121,89] When the excitation power becomes high, the population of the excited state converges to half of the total population of excited and non excited states.

The power saturation fit is shown in Figure 27 showing a saturation power at 2 nW and a natural linewidth of 13 MHz.

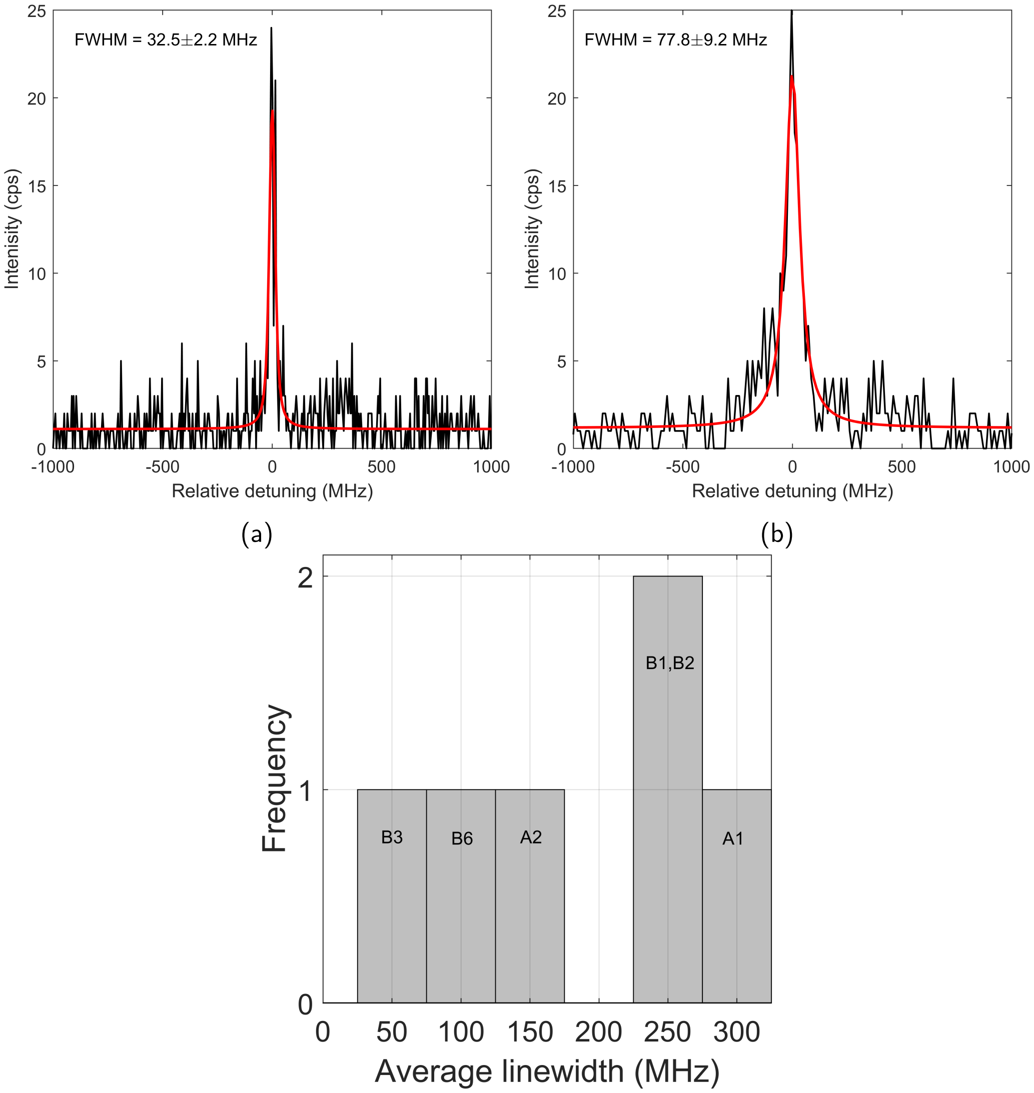

(a)

(b)

(c)

Figure 25: PLE single scans of NV ZPL for B3 (a) and B6 (b) respectively with Voigt functions fitted to the peaks, and the histogram (c) of the average ZPL linewidth from the single scans performed on each NV centre. The objective power of the 637 nm tunable laser used for the scans was 40 nW and 50 nW respectively.

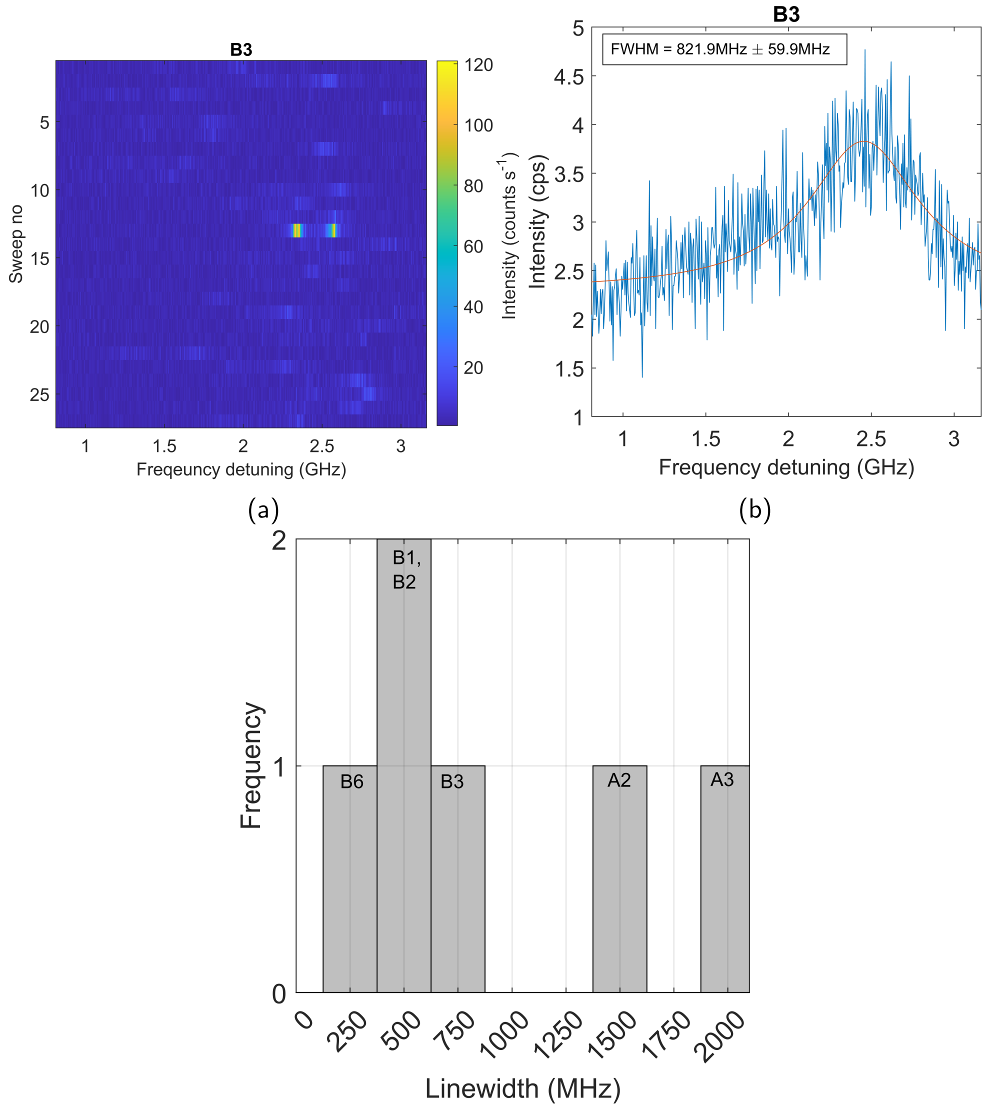

(a) (b)

(c)

Figure 26: Determination of the total linewidth of the ZPL for the B3 NV centre. The single sweep scans that show peaks (a) are added together (b) and the overall peak is fitted to extract the total linewidth. The total linewidths of each NV characterised are presented in the histogram (c).

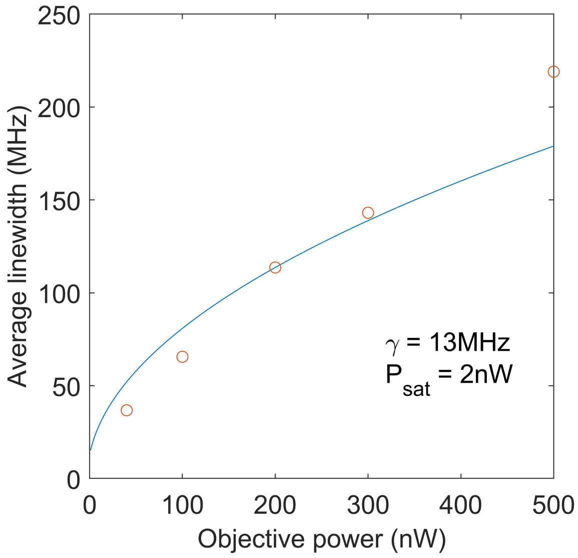

Figure 27: Power saturation measurement of the B3 ZPL.

7.3 Discussion

For generating entanglement, a target linewidth for the NV ZPL is to be less than 100 MHz.[89] To measure the quality of the NVs fabricated, the Empirical Cumulative Density Function (ECDF) of the NV single scan linewidth can be evaluated at 100 MHz to quantify the amount of NVs that have linewidths below 100 MHz.[69] This is shown in Figure 28 and the ECDF evaluated at 100 MHz is 0.167. A comparison of the ZPL linewidth measurements to literature is shown in Table 2. The average linewidth of the single scans for NVs formed using laser writing and diffusion is broader than the linewidths formed by other methods. For the ECDF of the linewidths, the ECDF below 100 MHz for the laser-written and annealed NV centres was significantly lower than that of the NV centres formed by other methods. This may imply that the laser diffusion process is producing NVs with broader ZPL linewidths and that the process needs to be further improved to obtain NVs with narrow linewidths. Another possible explanation is that the linewidths were power broadened. For the narrowest linewidth NV, the lowest power used to obtain the PLE scans was around 50 nW, which was larger than the power saturation (2 nW), suggesting that the linewidths obtained were power broadened. The total

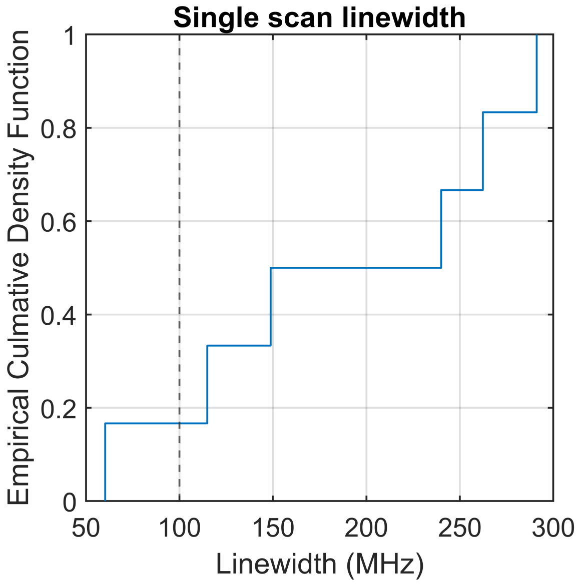

Figure 28: Empirical cumulative distribution function of the NV ZPL single scan linewidths of the MHz laser written and diffused NV centres.

Author	GR1 formation method	GR1 diffusion method	Depth (µm)	Average linewidth (MHz)	ECDF(100 MHz)
A Kirkpatrick (This work)	Laser writing	Laser diffusion	20	186	0.167
V Yurgens [69]	Laser writing	Thermal anneal	2	62.1	0.923
V Yurgens [69]	Laser writing	Thermal anneal	7	62.1	0.909
V Yurgens[69]	Laser writing	Thermal anneal	25-40	74.5	0.811
Y Chen [58]	Laser writing	Thermal anneal	50	98.2	0.583
Y Chen [58]	Laser writing	Thermal anneal	50	95.2	0.739
M Ruf [57]	Electron irradiation	Thermal anneal	$\sim$1.9	39.0	-

Table 2: Summary of the average single scan linewidths and empirical cumulative distribution function evaluated at 100 MHz linewidth for NV ZPL linewidths from different fabrication methods in literature.

linewidths of the NVs formed in site A were broader than the NVs found in site B, indicating that more spectral diffusion was observed in site A than site B. This suggests that the local lattice around site A had more charge defects than site B.[40]

There were also difficulties in measuring linewidths at lower excitation power and this is described in Figure29a, where the rate of ZPL peak presence per sweep was low at the lower objective powers. There is a maximum in the peak presence rate at around 300 nW. The peak presence rate can be described by the competition between the ZPL peak intensity, which increases with objective power and the photo-ionisation rate, which also increases with objective power. When the ZPL peak intensity increases, it becomes easier to measure the NV ZPL. However when the photo-ionisation rate increases, the chance of $NV^- \rightarrow NV^0$ charge state transition occurring increases so no ZPL peak is detected.

The photo-ionisation of the NV^- centre to the NV^0 state can also occur during the scan as shown in Figure29b, where there is a steep decline in counts at around -50 MHz frequency detuning. The linewidths of photo-ionised peaks will be narrower than the ZPL linewidths measured for ZPL peaks that have not been photo-ionised. If the photo-ionised linewidths are included for the average single scan linewidth, the average linewidth will be lower than the actual average. For this reason, the linewidths measured from photo-ionised peaks are discarded.

The difficulty in obtaining ZPL linewidths at lower objective powers may be due to misalignment of the optics, causing low excitation and collection efficiencies. Another reason could be the operation of the PLE sweep. In this PLE measurement, the resonant laser is continuously sweeping across the ZPL so the NV is being excited resonantly for a longer period, which increases the chance of photo-ionisation to the NV^0 state. Another consequence is that when the charge state is reset with a 532 nm pulse, the ZPL peak position changes and broadens the measured total linewidth. A comparison with operating PLE using discrete frequency steps with amplitude modulation[57,69] should be made to determine if the linewidths are dependent on the PLE measurement method.

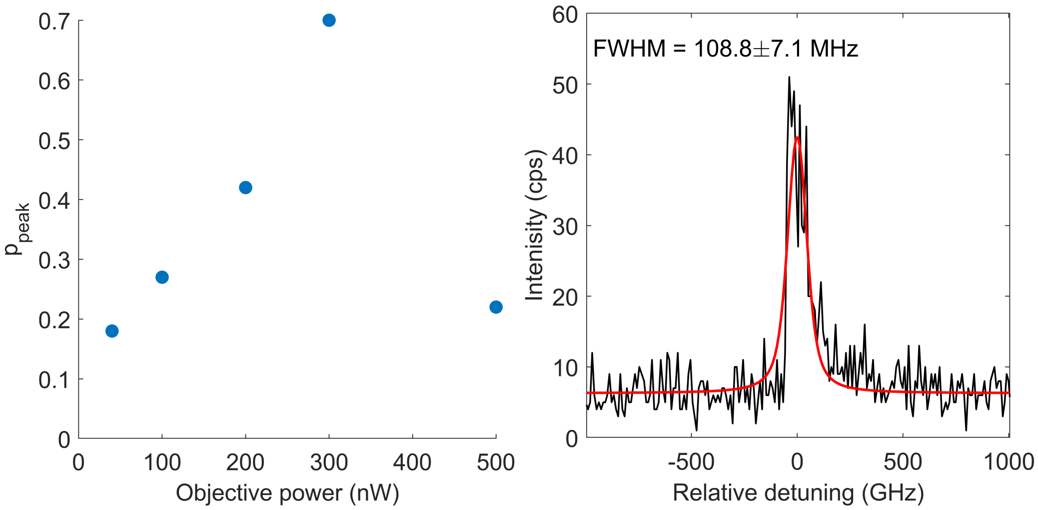

Figure 29: (a) Rate of a peak presence per sweep for different objective powers. (b) PLE single line scan showing photo-ionisation occurring during the sweep. This leads to a peak fit that underestimates the actual linewidth. Sweep was performed with 500 nW objective power.

7.4 Conclusion

The ZPL linewidth of NV centres formed by laser writing and laser diffusion in electronic-grade diamond has been characterised. The average linewidth and the Empirical cumulative distribution function of the ZPL linewidth at 100 MHz were 186 MHz and 0.167 respectively, implying that the laser diffusion process needs to be improved to be reliably used for fabricating NV centres for quantum entanglement. The power saturation measurement suggests that the linewidth measurements were power broadened and that the natural linewidths could be narrower. Further investigation into these NV centres would involve measuring the strain environment of the NV centres.

8 Cavity Locking

8.1 Introduction

Locking the cavity length is essential for open-access microcavity structures, which are susceptible to drift. For the application of cavity coupling to NV centres, the drift would decouple the cavity mode from the ZPL and reduce the ZPL emission, which would decrease the entanglement rate. In this chapter, the performance of the cavity fringe stabilisation described in Section 6.4 is characterised for locking the cavity and demonstrates its application in cavity-coupled continuous-wave ODMR of NV centres, which is described in Section 6.7.

8.2 Cavity locking performance

To assess the performance of the cavity fringe stabilisation, the spectra of the cavity modes were monitored over time. The cavity coupling setup was placed in an optical enclosure and mounted on a passive optical table to minimise vibrations that can decouple the cavity. Figure 30 shows the cavity modes taken 10 seconds and 10 minutes since the beginning of cavity locking using a 300 blaze grating. The inset of Figure 30 shows that the peak profile of the strongest mode has not changed for 10 minutes, indicating that the locking is strong enough to maintain the cavity length within the resolution of the spectrometer. However, there are also changes in the intensity of the transverse modes during the 10 minutes of locking, indicating that there is a lateral shift of the concave mirror. This is expected as the feedback can only compensate for the cavity length.

8.3 Cavity coupled continuous wave ODMR

When Continuous Wave (CW) microwave power was delivered to the loop antenna for ODMR, high microwave power is needed to observe the spin transition. However, applying high microwave power introduces heat. This heat would cause thermal expansion to the cavity assembly, leading the longitudinal mode to drift off resonance. The cavity fringe locking was able to com-

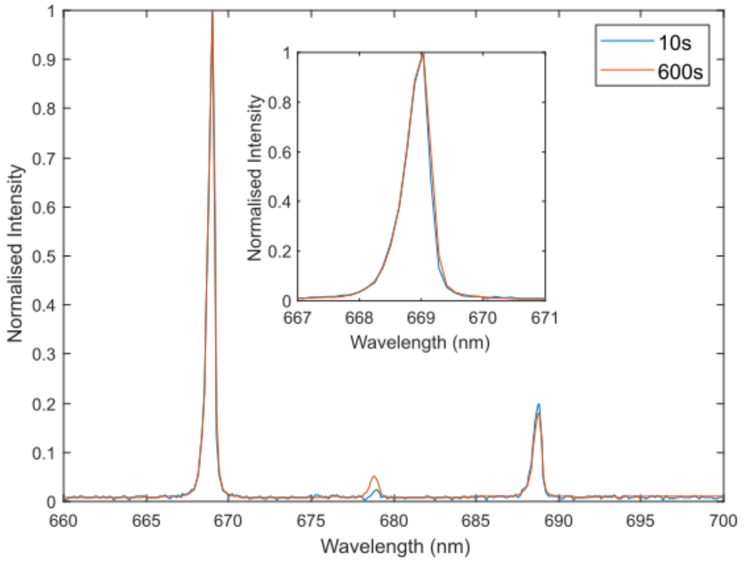

Figure 30: Optical spectrum of the cavity modes taken 10 s and 10 min after the start of the cavity locking. The modes are formed with a 4 µm RoC concave mirror. The inset plot shows the longitudinal mode at around 669 nm.

pensate for this drift and was also used to observe how applying microwaves affects the drift. Figure 31 presents the effects of how changing microwave power, frequency, and frequency sweeping rate affect cavity drift over time. Each plot contains three subplots that represent monitoring the drift for three events: delivering the microwaves to the antenna; applying the cavity locking after 5 minutes and then removing the locking and microwave delivery. The general observations of each of these events will be discussed first before looking at each parameter sweep in detail. In all the plots in Figure 31, it is shown that introducing microwave power will cause the cavity length to drift and over time, the drift appears to saturate. The extent of the drift is affected by the microwave power and frequency.

Upon applying the locking, the locking can compensate for most of the drift after 5 minutes of applying microwave power, to within a few hundred nanometres of the setpoint. This would not be suitable for cavity coupling to narrow linewidths such as the NV ZPL, where the coupling would be lost upon introducing microwave power.

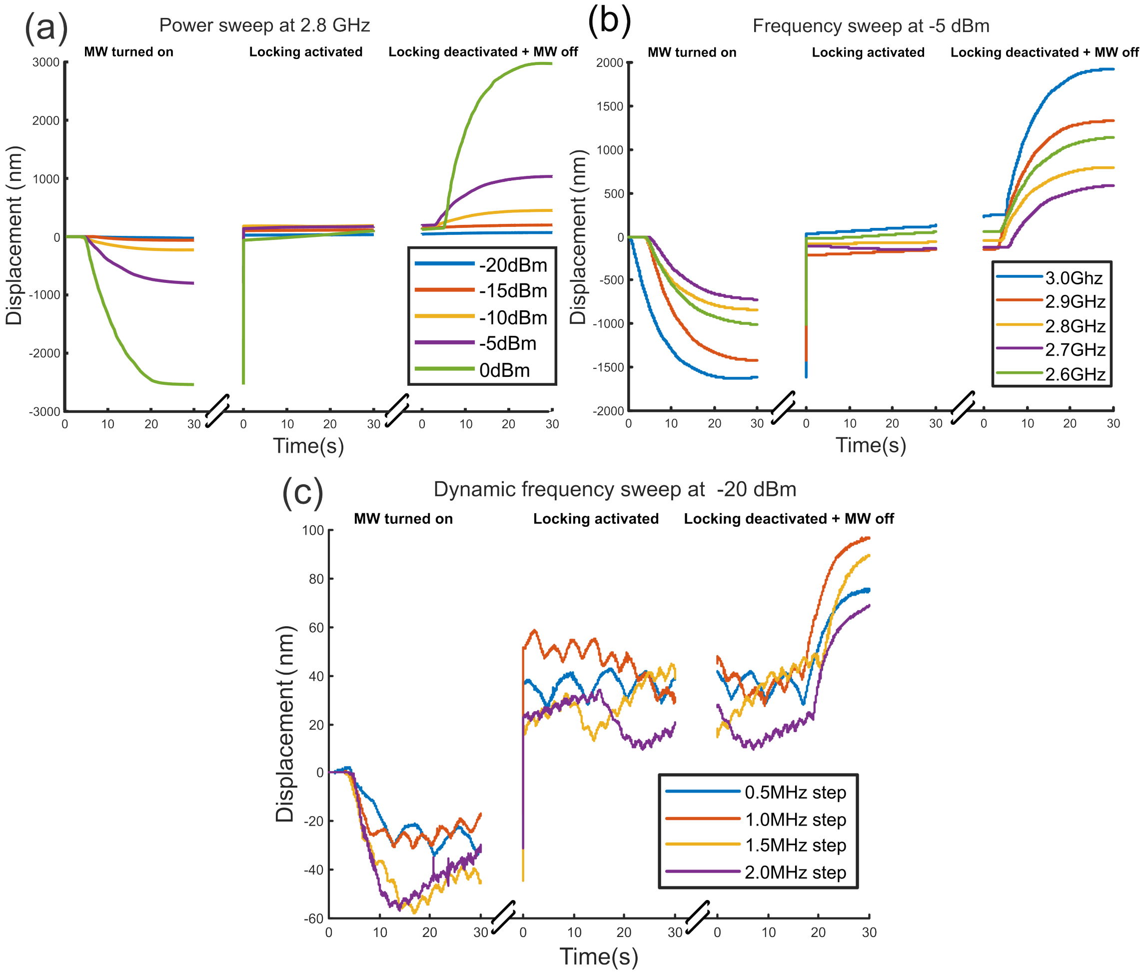

Figure 31: Plots of cavity drift against time for varying microwave power (a), microwave frequency (b) and microwave sweep rate (c). The dynamic frequency sweep range is 2.6 GHz-3.0 GHz. Each plot contains three subplots representing the start of the microwave delivery, applying the cavity locking after 5 minutes and removing the microwaves and locking to the cavity.

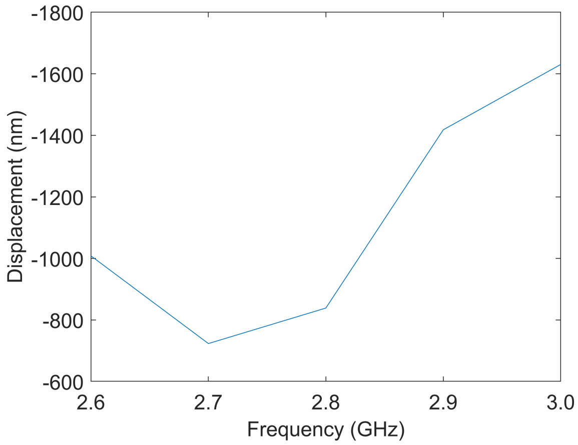

Figure 32: Maximum displacement introduced to the cavity by delivering continuous microwaves at different frequencies

When the microwave delivery and locking are removed from the cavity, the cavity length drifts in the reverse direction to when the microwaves were being applied.

In Figure 31a, the power sweep shows that increasing the microwave power increases the drift of the cavity. This is expected as higher power would generate more heat, leading to further thermal expansion and drift. For the frequency sweep shown in Figure 31b, there is a minimum in peak drift that occurs around 2.7 GHz. This is emphasised in Figure 32 and may correspond to the resonant frequency of the antenna.

When the microwave frequency is continuously swept as shown in Figure 31c, the cavity is drifting periodically in relation to the frequency. The period of the oscillation is related to the frequency step size and the amplitude of the oscillation decreases with increasing frequency step size. This further supports that there is a frequency dependent drift as shown in the static frequency sweep. There is also a decrease in amplitude of the oscillating drift when the frequency step increases, which could be explained by the drift response being unable to respond quickly enough to the change in frequency. When the locking is active, it is unable to respond strongly enough to cancel out this periodic drift.

For cavity coupling to the NV PSB which has a broad linewidth, the locking can maintain resonance with the NV PSB, allowing for cavity-coupled ODMR to be performed and this is

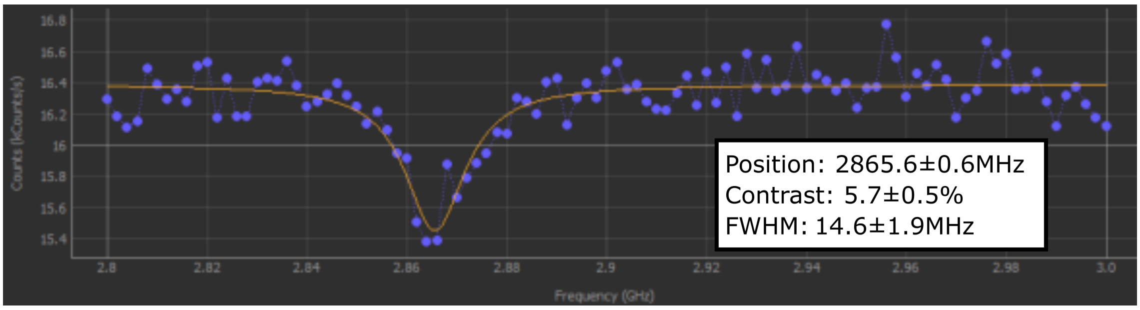

Figure 33: Screenshot showing a plot of the CW ODMR sweep for a cavity-coupled 100 nm Nanodiamond containing 1000s NV centres (FND biotech brFND-100). The plot was averaged over 100 scans and was taken using Qudi.[126] The position and FWHM of the signal are shown in the inset. The ODMR linewidth is expected to be broader due to the ensemble of NVs present and its linewidth is consistent with those reported in the literature.[125]

shown in Figure 33. The ODMR linewidth is dependent on the dephasing rate of the electron spin of the NV centre, which depends on the amount of charge defects and spin impurities in the diamond host.[122,123] By using diamond with a low concentration of ^{13}C isotopes, the ODMR linewidth in bulk diamond can be reduced to the kHz scale.[124] For nanodiamonds containing around 500 NV centres, the ODMR linewidth value ranges between 10-30 MHz[125]. The nanodiamonds used in this thesis contain 1000s of NV centres, so the ODMR linewidth of 14.6 MHz is within expectation.

8.4 Discussion

From the locking performance, this cavity fringe stabilisation presents an alternative approach to locking the cavity length for long-term cavity-coupled devices such as single photon sources, where previous attempts have been to use glue to stabilise the cavity passively. Compared to other active locking methods such as Pound-Drever-Hall (PDH)[127], this method offers a simpler approach as it requires components that most home built confocal systems already have or can be obtained at relatively low cost. These components are: widefield imaging, cavity illumination and fine control of the cavity length.

The locking stability measurement was limited by the resolution of the spectrometer (0.13

nm). Microcavity stability of 4.3 pm[128] and 0.5 pm[129] has been shown using passive vibration isolation with a helium dewar. Since the measurements in this thesis were performed outside the dewar, a higher resolution stability measurement of the microcavity in the dewar would be necessary to compare the locking performance. This measurement can be achieved by using a higher resolution grating for spectroscopy or by sweeping a narrow linewidth laser and monitoring the cavity reflection/transmission.

However, the fringe stabilisation locking is unable to recover the setpoint wavelength for large amounts of drift that occur before activating the locking and for faster drift, which occurs when the microwave frequency is continuously swept. To minimise the error in locking performance, the locking setpoint should be set after the majority of drift has been introduced, which for this case would be applying the microwave input and allowing the drift to saturate. To minimise the fast drift, the feedback could be improved by tuning the PID parameters or by sweeping the microwave frequency more slowly, allowing the locking to have more time to correct the drift.

Within the scope of cavity-coupled spin control for NV centres, pulsed microwave sequences would be applied when the cavity is coupled instead of CW ODMR, which is used for characterisation. The pulsed sequences would send microwave pulses on the order of microseconds. For a continuous wave microwave delivered at the highest power as shown in Figure 31a, the steepest drift over time was around 315 nm s^{-1} when the microwave power is introduced and 375 nm s^{-1} when the microwave power is removed. This suggests that the maximum drift introduced by the microsecond microwave pulse would be around 0.315 pm of drift. This drift would be enough to detune the cavity from the ZPL linewidth (0.02 pm) and on a timescale faster than this cavity locking procedure can compensate for. However, the spin manipulation and optical readout are performed sequentially, so after the microwave pulse is delivered, a delay can be introduced to allow the cavity to recover from the drift and minimise the detuning. To increase the locking frequency, faster data acquisition from a higher frame rate camera and more computing power would be required to increase the data processing speed. The higher frame rate would also mean that there is a shorter exposure time, so the brightness of the LED would need to increase to ensure the signal acquired is strong enough to acquire the interference fringes.

8.5 Conclusion

Cavity fringe stabilisation has been implemented in a low temperature capable open-access microcavity system. The locking can maintain the cavity length against passive drift, but is unable to lock against large and fast amounts of drift introduced by microwave input. Solutions to improve the locking could be to improve the feedback response or to reduce the amount of drift introduced by the microwave source. The drift can also be minimised by depositing the antenna on the cavity mirrors, which reduces the antenna distance to the NV and the power required to excite the spin transition.

9 Aberration corrected cavity coupling

9.1 Introduction

In this chapter, the effect of how aberrations in the microcavity affect the collection efficiency will be explored. The collection efficiency is defined as the fraction of the intensity of light collected through a pinhole from the sample over the intensity of light collected from a diffraction-limited source. A diagram showing how the aberrated light affects the collection efficiency is shown in Figure 34. The light is collected from the sample with an objective lens. Aberrated light will have an aberrated wavefront whilst diffraction-limited light will have a planar wavefront. When the aberrated light is refocused, the spot formed will have a broader intensity profile than the diffraction-limited spot, resulting in less light being transmitted through the pinhole and a lower collection efficiency. Lower collection efficiencies will lead to longer acquisition times and entanglement rates for photon based entanglement. This chapter will explore the microcavity aberrations by first presenting a model calculating the spherical aberration introduced by transmission through the planar mirror substrate. Then the results of the experimental measurements showing how applying aberration correction to cavity-coupled NV centres affects the power saturation and the cavity mode spectrum will be presented and

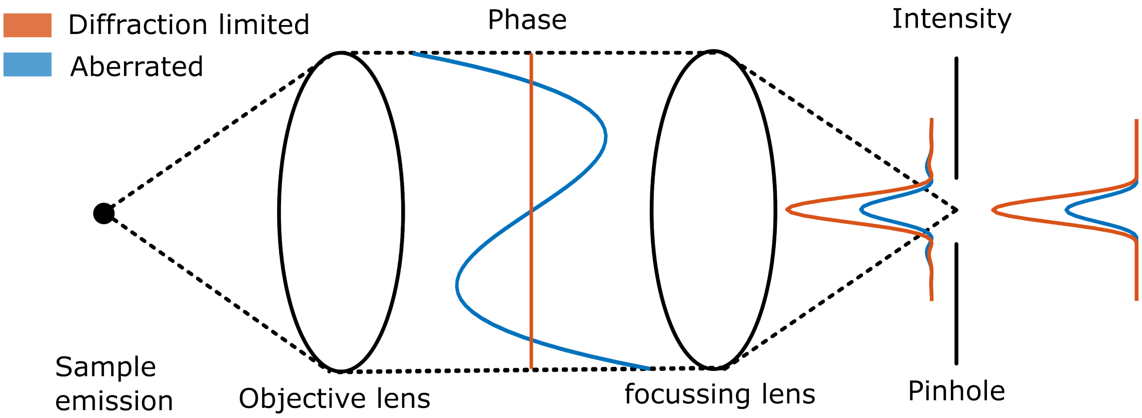

Figure 34: Diagram of how collection efficiency is determined. The pinhole diameter is set to match the diameter of the diffraction-limited spot.

discussed.

9.2 Modelling the spherical aberration within the microcavity

9.2.1 Introduction

The spherical aberration from the hemispherical micro-cavity emission can be modelled using Gaussian optics and the aberration equation. This model can be separated into three steps: cavity mode excitation and emission; transmission and aberration through the mirror substrate and collection into the single-mode fibre. This is illustrated in Figure 35 and the following sections will describe these steps and the results of the model.

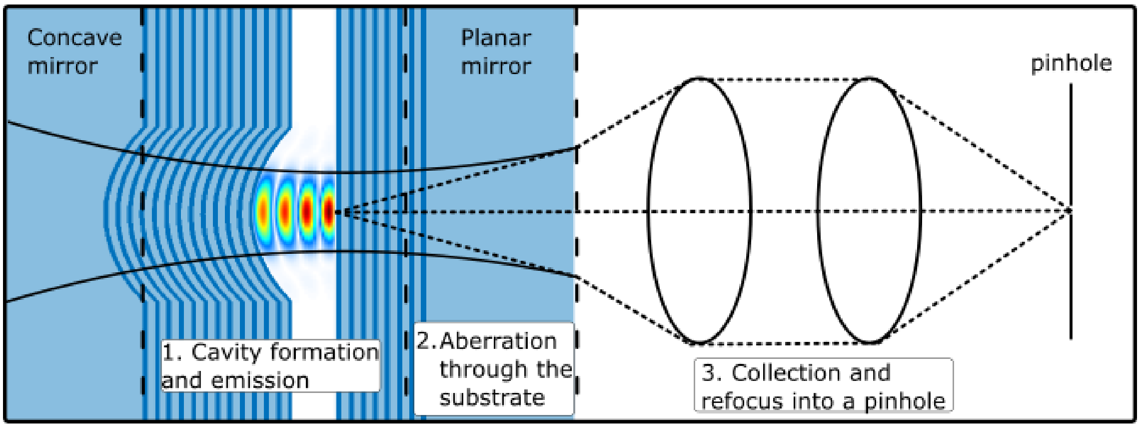

Figure 35: Schematic description to modelling the effect of aberrations to the cavity emission
.

9.2.2 Cavity mode formation and emission

The amount of spherical aberration is related to the effective numerical aperture (NA) of the light that is being collected. This is normally determined by the numerical aperture of the objective lens NA$_{obj}$, which is the limit for the angle of light that can be collected from the emitter. However for cavity mode emission, if the numerical aperture of the cavity mode emission NA$_{cavity}$, is less than the objective lens (NA$_{cavity}$< NA$_{obj}$), the numerical aperture of the cavity mode emission will be the effective numerical aperture of the collected beam. This

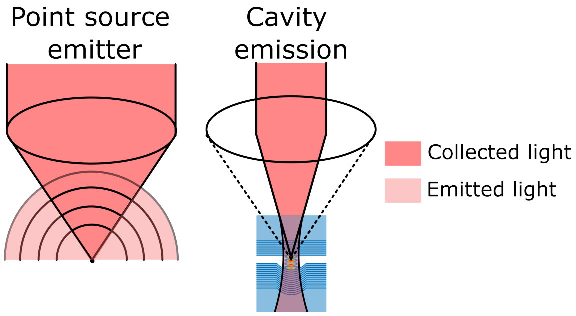

Figure 36: Diagram of the light collection by the objective lens from a point source emitter and a cavity mode.

RoC (μm)	NA
4	0.36
8	0.30
12	0.27
25	0.22

Table 3: Calculated numerical apertures of the cavity mode with $\lambda = 637nm$ and $L = 1\lambda$.

is shown visually in Figure 36.

For a hemispherical microcavity with set cavity length L and radius of curvature of the concave cavity mirror R_2, the minimum beam waist and numerical aperture of the cavity mode can be calculated using Equations 5.16 and 5.21, which have been restated below.

$$NA = n\sin(\theta) = n\sin(\frac{\lambda}{\pi\omega_0}) \tag{5.16 revisited}$$

$$\omega_0^2 = \frac{\lambda}{\pi}\sqrt{R_2L - L^2} \tag{5.21 revisited}$$

The radius of curvature (RoC) of the concave mirrors on the substrate was 4 μm, 8 μm, 12 μm and 25 μm. For a cavity mode with a wavelength of $\lambda = 637\ nm$ and a cavity length of $L = 1\lambda\ (q = 2)$ which is the shortest cavity length possible, the maximum possible numerical aperture values for each RoC are shown in table 3. As the microcavity dimensions approach the wavelength scale, the approximation of using ray optics breaks down.[130] To further validate these numerical aperture values of the cavity emission, FDTD simulations using Lumerical[131] were performed to model the far field emission of the cavity emission vs RoC.

The simulation was built by generating the microcavity geometry of the planar mirror and concave mirror with DBR mirror layers of SIO_2 (n = 1.46) and Ta_2O_5 (n = 2.12) within the software. The planar mirror has $N = 10$ pairs of DBR mirror coatings and the concave mirror has $N = 16$ pairs of DBR mirror coatings. The cavity length was set to 637 nm and a broadband dipole source with a wavelength of 637 nm and a bandwidth of 50 nm was placed on the planar mirror to excite the cavity mode. A far-field monitor was placed outside the cavity on the planar mirror side to measure the emission from the cavity mode. This simulation model was developed by me. In Figure 37, the intensity of the far field emission shows most of

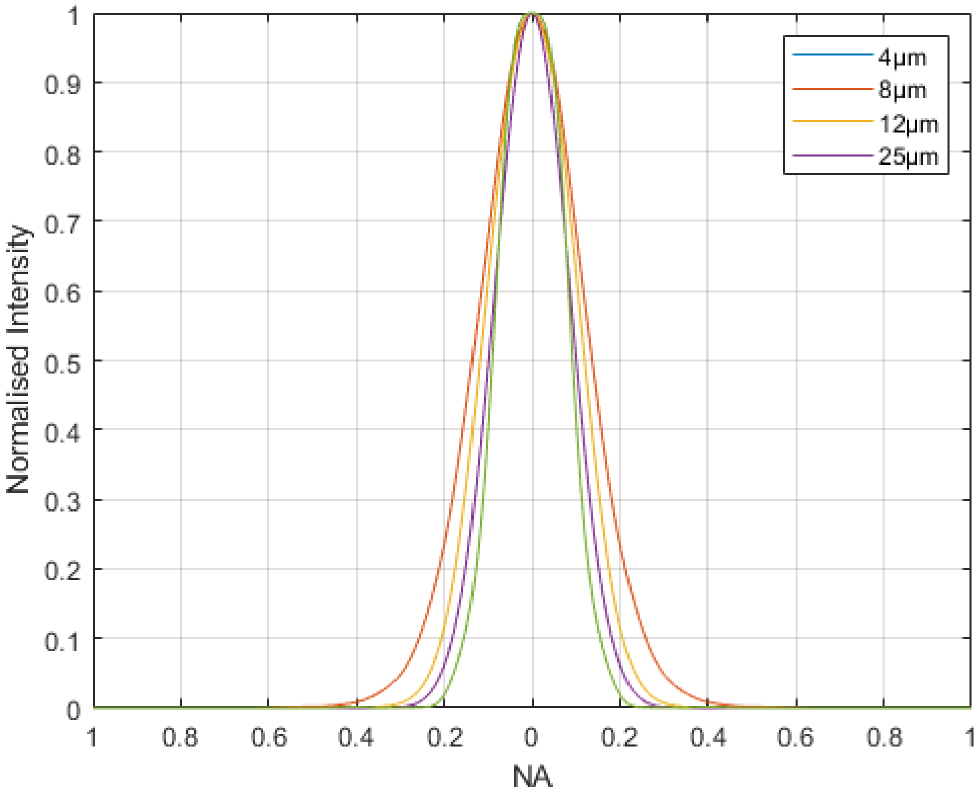

Figure 37: FDTD simulation of the normalised far field intensity profile of the cavity mode emission through the planar mirror direction for hemispherical cavities with different radii of curvature. The cavity length was set to $q = 3$ and DBR mirror reflectivity $R_1 = 99.8\%, R_2 = 99.99\%$.

the energy radiates within the range $0.2 < NA_{cavity} < 0.4$, which compares well to the values calculated using the paraxial approximation. This supports that the values of the numerical aperture for cavity mode emission are less than the numerical aperture of the objective lens ($NA_{cavity} < 0.82$), so the effective numerical aperture used in the spherical aberration equation is determined by the microcavity.

9.2.3 Spherical aberration through the mirror substrate and collection

The cavity mode will transmit through the mirror substrate and the refractive index mismatch as well as the mirror substrate thickness will introduce spherical aberration to the cavity emission as it leaves the substrate. The method of modelling the collected intensity is the same as shown in Section 5.8.3 and the results of the model are shown in Figure 38. Figure 38 shows the normalised intensity collected against the NA$_{cavity}$ through the planar mirror. The intensity starts to reduce when the NA$_{cavity}$ increases above 0.25 and rapidly decreases when the NA$_{cavity}$ is between 0.4 and 0.65, and then continues to steadily decrease when the NA$_{cavity}$ is above 0.65. Using thicker substrates shows an earlier reduction in intensity starting at lower NA values compared to using thinner substrates.

For the microcavities used in the experiment, the maximum expected NA range of the cavity mode emission is $0.22 < NA_{cavity} < 0.36$ and the planar mirror substrate thickness is 200 µm. Within these parameters, this model predicts that the decrease in intensity due to spherical aberration from the mirror substrate will be less than 10 %. The following section presents the experimental results of aberration correction on the micro cavity emission.

9.3 Microcavity aberration

9.3.1 Power saturation measurement

Aberration analysis on the microcavity was performed using open-loop aberration correction[132] on cavity-coupled NV centres and taking power saturation measurements before and after aberration correction. The open-loop aberration correction process involves applying Zernike

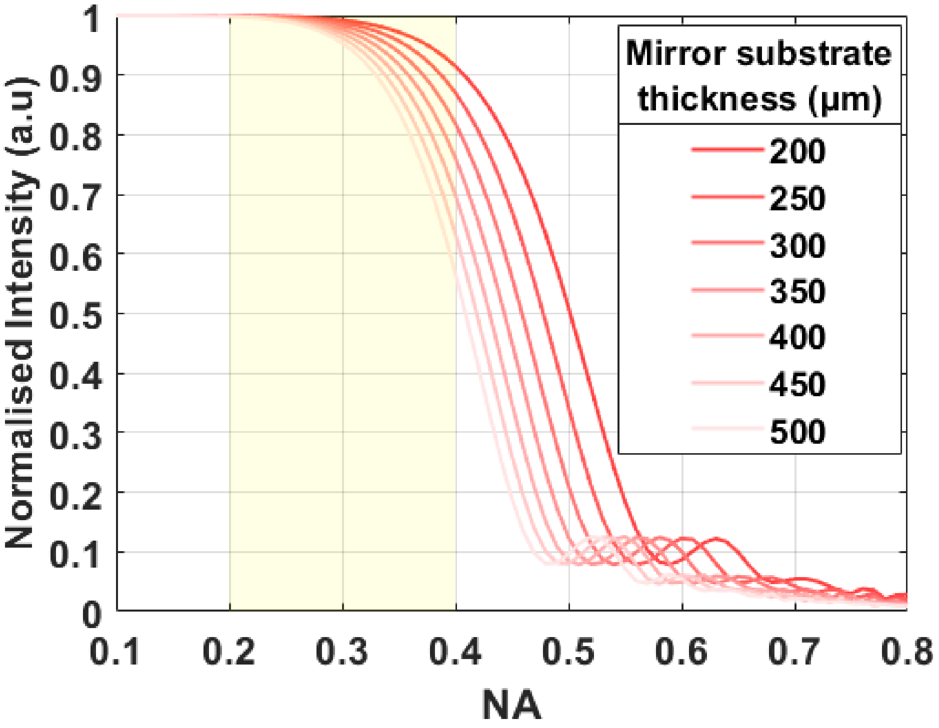

Figure 38: Normalised collected intensity profile against the numerical aperture of the cavity mode emission with spherical aberration introduced by the mirror substrate. Profiles are evaluated at $\lambda = 637\ nm$ and with different substrate thicknesses with $n_2 = 1.5$. The shaded region covers the NA of the cavities available for this study. This model was scripted in MATLAB by me.

polynomials to the deformable mirror and sweeping the amplitude of the Zernike polynomial. The collected intensity is monitored to find and apply the amplitude that maximises the intensity. This process is repeated for each of the Zernike polynomials to find the effect of each Zernike polynomial. The optical excitation power was set to 4 mW to power saturate the NV fluorescence. This ensured that any increase in collected intensity with aberration correction was associated with an enhancement of collection efficiency rather than excitation efficiency due to the decrease in the excitation spot size. Aberration correction was applied initially on the NV centres through the planar mirror and before cavity coupling to correct for any aberrations from the confocal system and the planar mirror. The amplitudes of the Zernike polynomials applied before cavity coupling are used as the reference values for any aberration correction after cavity coupling. After the cavity modes have been formed, further aberration correction is applied to study the aberration introduced by the microcavity. The RoC of the concave mirror used was 5 μm and the NA$_{cavity}$ was estimated to be around 0.35. From Figure 38, for a 200 μm thick substrate and $NA = 0.35$, the model predicts a 2.8 % increase when applying aberration correction. Figures 39a and b show the power saturation curve and spectrum of cavity-coupled NV centres before and after aberration correction. The saturation intensity and power have increased around 7 % and 4 % respectively after applying aberration correction, which would give an effective increase of around 3 %, which compares well to the model. However, the cavity mode spectrum shows that this cavity was primarily coupled to the *l+m=1* mode and that there was an increase in collected intensity of the TEM$_{00}$ peak and a decrease in the TEM$_{l+m=1}$ peak after aberration correction. The shift in cavity mode peak positions is likely due to a drift in the mirror position, changing the cavity length.

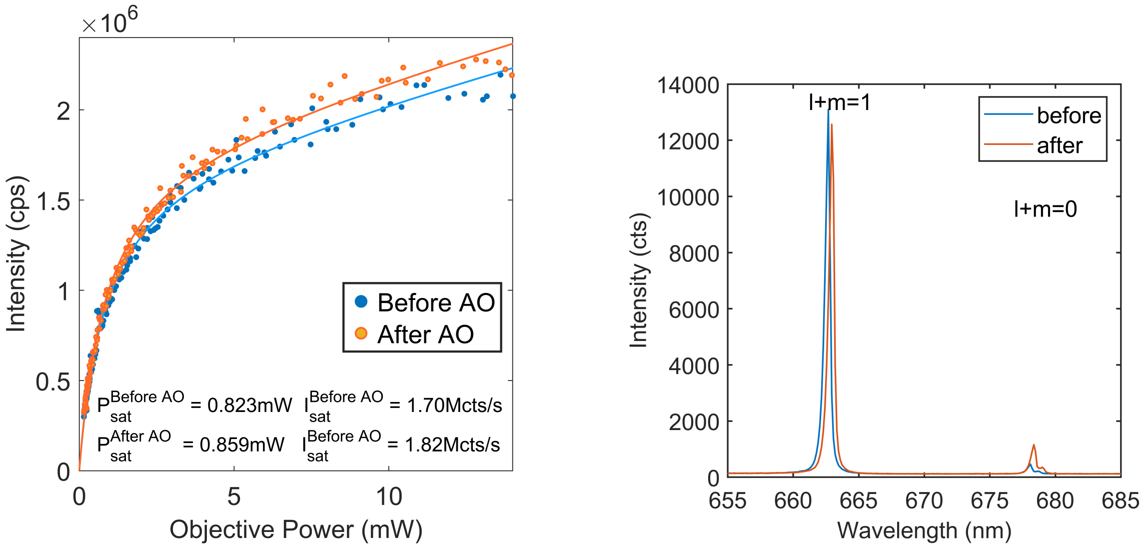

(a) (b)

Figure 39: Power saturation and spectrum of a $5\mu m$ RoC hemispherical cavity before and after applying aberration correction. Power saturation plots are fitted using Equation 6.2

9.3.2 Cavity multi mode measurement

To further investigate the effect of how the aberrations affect the collection of the TEM$_{00}$ and the higher order cavity modes, the spectrum of a multi-mode cavity is taken for different amplitudes of a Zernike polynomial applied to the deformable mirror. This was achieved by first applying aberration correction on the emitter before cavity coupling to define reference amplitudes for each of the Zernike polynomials. Then the cavity is closed to support multiple modes and the cavity mode spectrum is measured for different amplitudes of each Zernike polynomial. Figure 40 shows the multi-mode cavity spectrum under the effects of different amplitudes of primary spherical aberration.

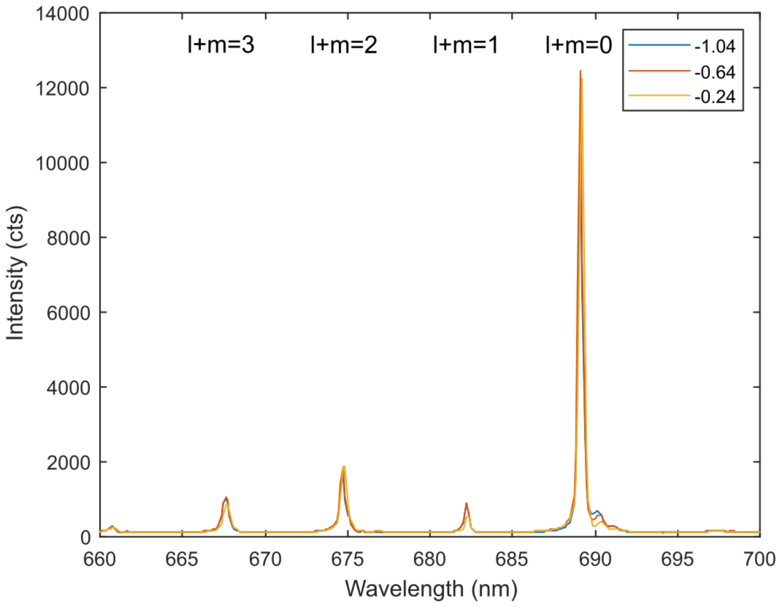

Figure 40: Spectrum of a multi-mode $25\ \mu m$ RoC hemispherical microcavity with a longitudinal mode index q=18 and primarily coupled to the TEM$_{00}$ mode. The *(l+m)*$_{even}$ modes are coupled stronger than the *(l+m)*$_{odd}$ modes. The spectra were taken for 30 s at varying amplitudes of primary spherical aberration applied to the deformable mirror. The amplitude of primary spherical aberration was ± 0.4 radians from the reference amplitude determined by the open-loop aberration correction. The total transverse mode index of the peaks are labelled above the peak.

Cavity mode wavefront decomposition For comparison of the Zernike polynomial sweep for the higher-order cavity modes, the wavefront of the Hermite-Gaussian cavity modes is fitted to the Zernike polynomials to find which aberrations are expected to have the strongest contributions to the wavefront. Figure 41 shows the amplitudes of the Zernike polynomials of the first eight radial degree components (n) for each of the Hermite Gaussian cavity modes. The plots of the aberration components for each mode are grouped by the sum of their transverse mode index *l+m = 1* (a), *l+m=2* (b) and *l+m=3* (c), to aid comparison. The cavity modes with odd sums of the transverse indices (*l+m=1* and *l+m=3*) show that most of the significant aberrations that contribute to the wavefront are from the Zernike polynomials with odd indices of the azimuthal degree, $Z_n^{m_{odd}}$ (coma, trefoil and pentafoil), whilst the modes with even sums of the transverse mode indices (*l+m=2*) shows that most of the contribution comes from the Zernike polynomials with even indices of the azimuthal degree $Z_n^{m_{even}}$ (astigmatism, quadrafoil and spherical aberration). This implies that the collected intensity of cavity modes with odd/even sums of the transverse indices will improve by applying Zernike polynomials with odd/even indices of the azimuthal degree respectively.

Cavity measurement 1 To present the effects of applying Zernike modes for each peak as seen in Figure 40, the intensities for each *l+m* cavity mode index are normalised to the intensity with the reference amplitude of the Zernike polynomial and presented as a bar plot for each cavity mode index. Figure 42 shows the relative changes in intensity when the primary astigmatism, primary coma and the first, second and third order spherical aberrations are individually swept. For the astigmatism sweeps, the most significant increase of 11 % in intensity is seen for the *l+m=2* cavity modes when the oblique astigmatism is swept. This supports the observations in Figure 41 that astigmatism is one of the major components contributing to the wavefronts of those modes and can be corrected to improve the collection of the cavity mode. There is also an 11 % increase in the fundamental mode *l+m=0*. There are also smaller increases of 2% in the vertical astigmatism sweep for the *l+m=1* and *l+m=2* cavity modes.

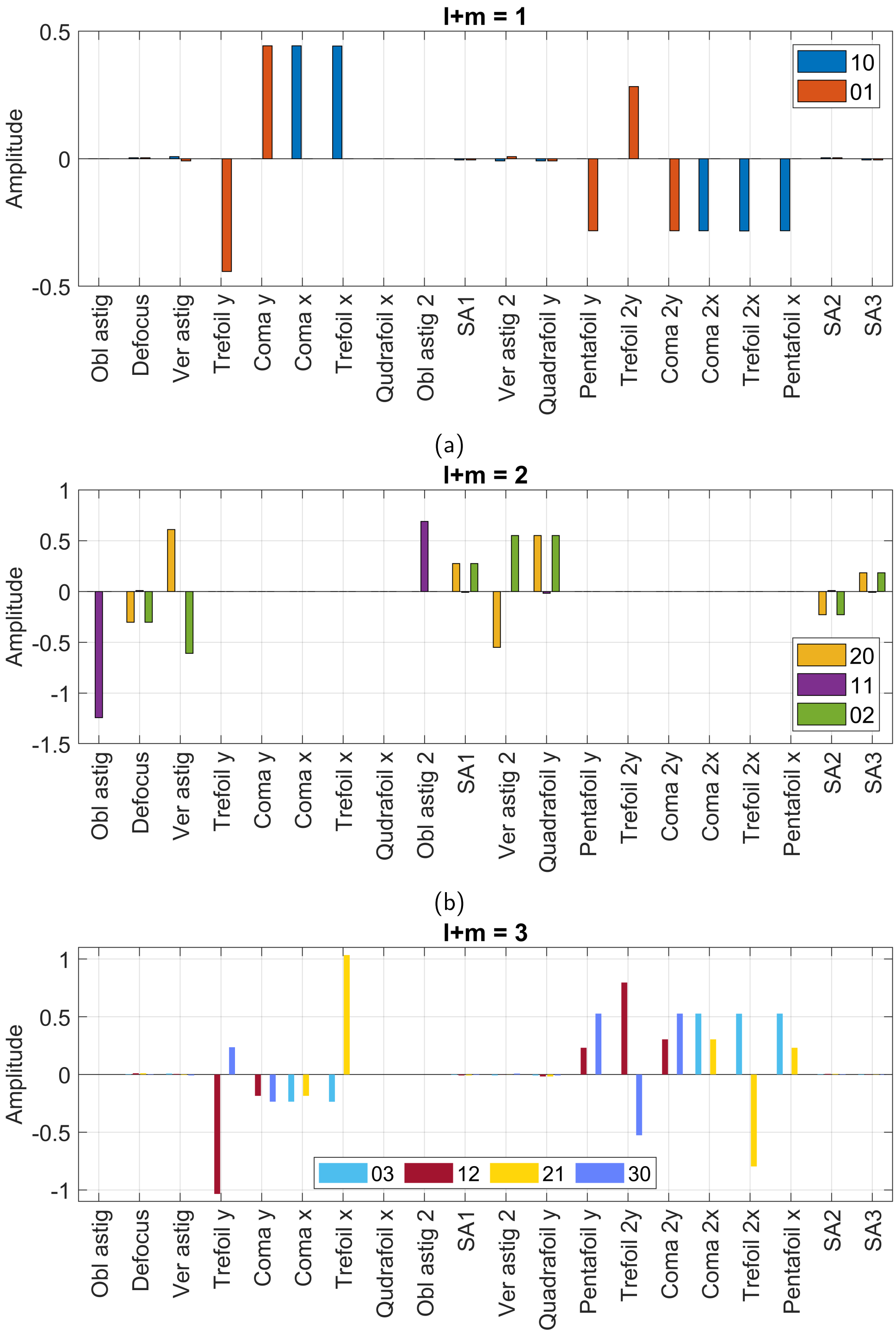

(a)

(b)

(c)

Figure 41: Amplitudes of the Zernike aberrations fitted to the TEM$_{lm}$ wavefronts. The plots are grouped by the sum of their transverse mode index (l+m).

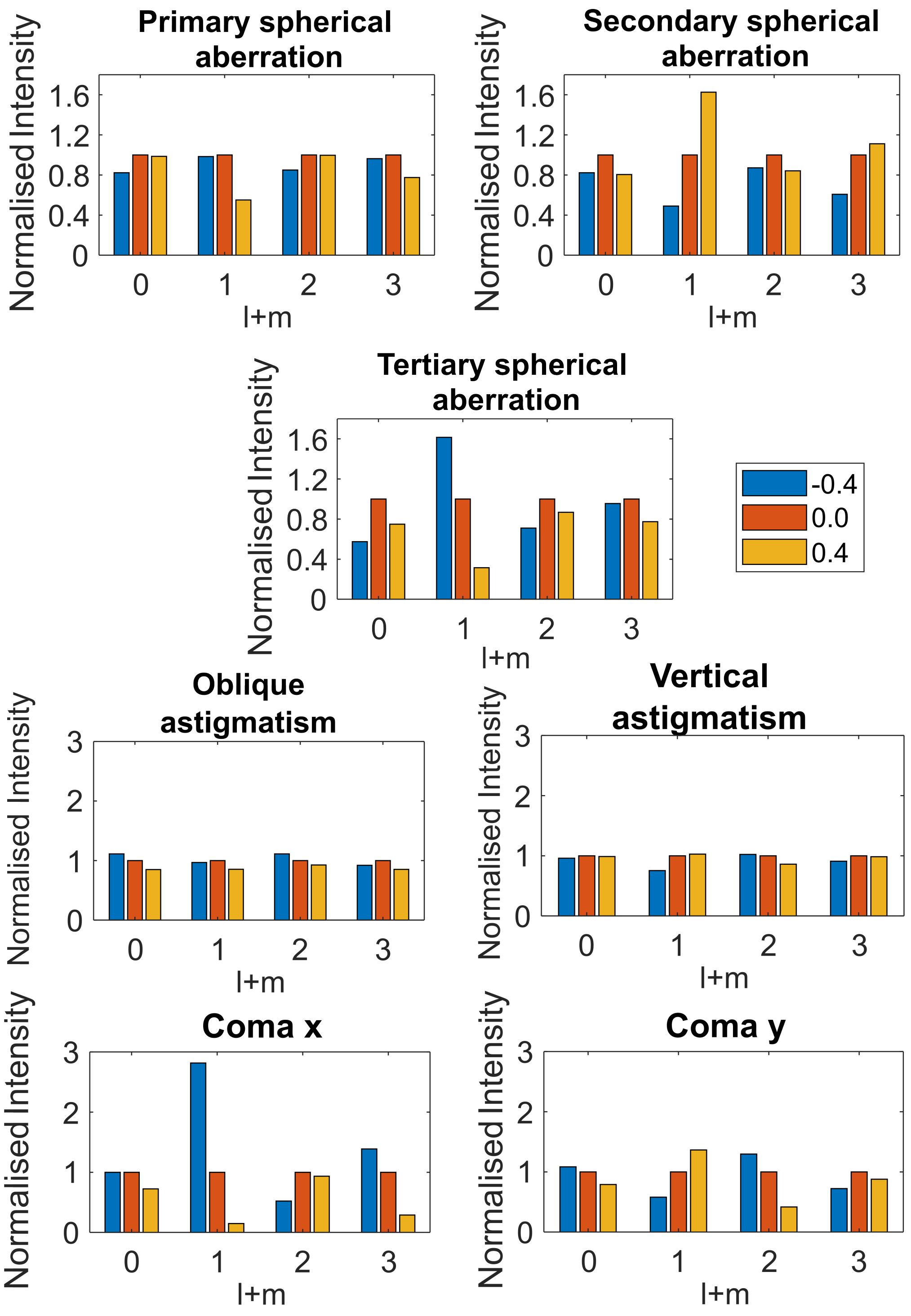

Figure 42: Bar plots of the intensity of the cavity mode peaks under the effects of spherical aberration, astigmatism and coma of different amplitudes. The cavity is coupled using a $25\ \mu m$ RoC concave mirror. Peak intensities are normalised to the midpoint amplitude.

Likewise for the coma aberration sweeps, the most significant increases are observed for the *l+m=1* and *l+m=3* cavity modes when the coma x aberration is swept, where improvements of 170 % and 39 % can be seen respectively. There are also smaller increases shown in the coma y sweep for the modes *l+m=0*, *l+m=1* and *l+m=2* showing increases of 8 %, 36 %, and 29 % respectively. Compared with the astigmatism aberration sweeps, the coma aberration sweeps show a greater increase.

For the spherical aberration sweeps, the *l+m=1* cavity modes show increases with secondary (62 %) and ternary (61 %) spherical aberration. This was unexpected as the theory predicted they would be unaffected by spherical aberration.

Cavity measurement 2 Another aberration sweep is taken for the same cavity but in a cavity mode configuration which is primarily coupled to the TEM$_{01}$ mode. These results are presented in Figure 43. The aberrations affect the collection of the modes for this cavity configuration differently compared to the previous measurement in Figure 42. For the astigmatism y sweep, there are increases in intensity when the amplitude is swept for the cavity modes with *l+m=0*, *l+m=2* and *l+m=3* of 12 %, 9 % and 9 % respectively. The increase in intensity for *l+m=3* cavity modes was unexpected as the theory did not predict astigmatism to have any contribution in Figure 41. For the *l+m=2* cavity modes, there was a concave profile where applying both ± 0.4 waves for astigmatism y increased the intensity. For astigmatism x, there were increases in intensity with the *l+m=0* and *l+m=3* modes of 12 % and 14 % respectively.

For the coma aberration, the larger increases are seen in the $(l{+}m)_{even}$ cavity modes instead of the $(l+m)_{odd}$ cavity modes as seen in Figure 42. For the coma x sweep, there was a 14 % increase with the *l+m=0* cavity mode and a 1 % increase with the *l+m=2* cavity mode. For the coma y sweep, there were increases in intensity for the *l+m=0*, *l+m=2*, *l+m=3* modes of 27 %, 22 % and 7 % respectively.

For the spherical aberrations, there are little to no increases when sweeping for any of the spherical aberrations. There was a 2% increase in intensity for the *l+m=0* modes by applying

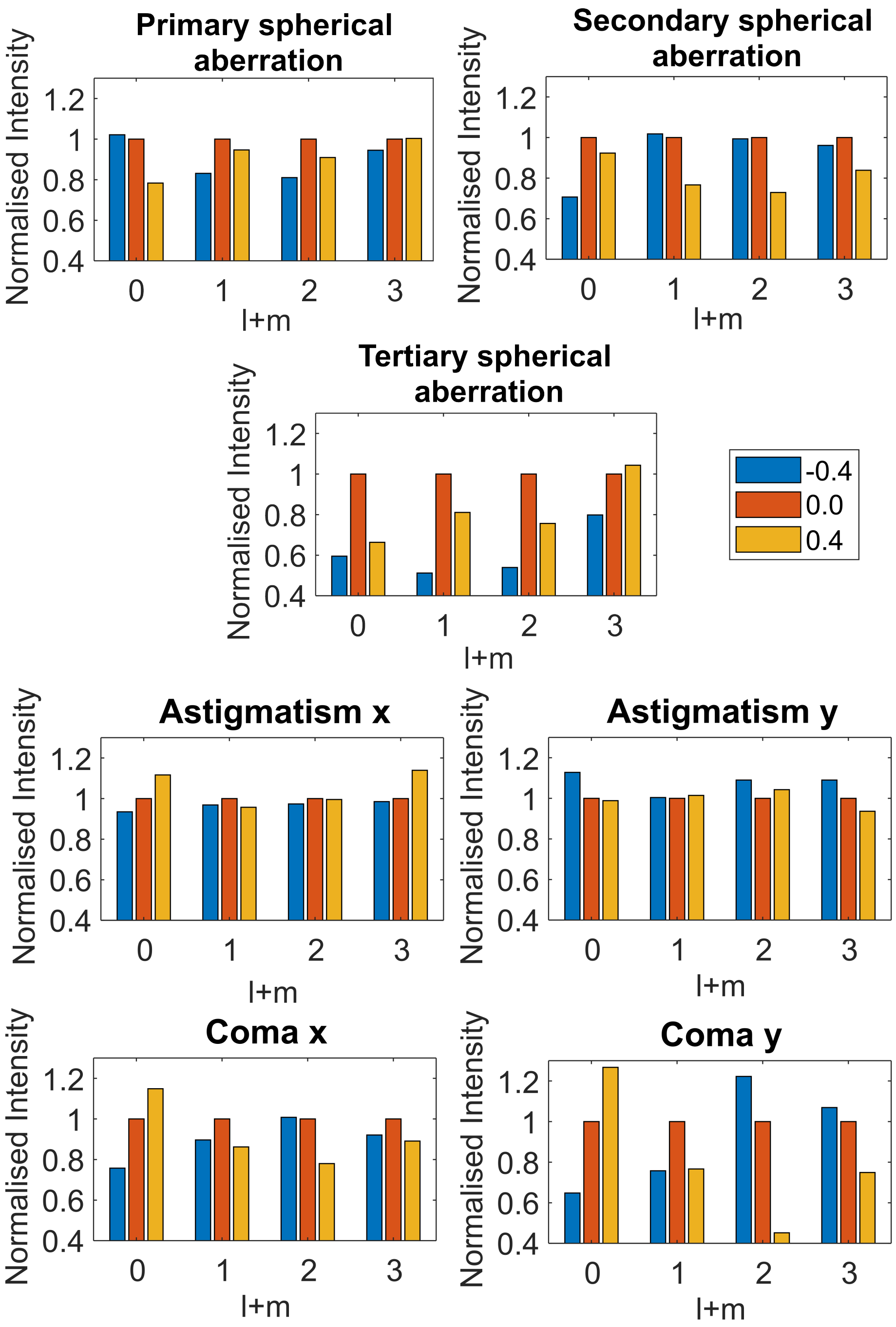

Figure 43: Bar charts of the relative peak intensities of the cavity modes for different amplitudes of the Zernike polynomial applied to the deformable mirror for the $25\ \mu m$ multimode cavity, which is strongly coupled to a TEM_{01} mode. Peak intensities are normalised to the intensity obtained using the reference amplitude.

primary spherical aberration and $l+m=1$ modes by applying secondary spherical aberration, and a 4% increase for the $l+m=3$ modes by applying tertiary spherical aberration.

9.3.3 Effects of aberration correction on higher order modes

To further understand how the aberrations applied during the amplitude sweeps affect the intensity of the modes, the intensity profiles of the cavity modes were modelled with the Zernike polynomials applied to the cavity mode wavefront ($\Psi = \Psi_{cavity} + aZ_n^m$). The method of modelling the intensity profile is the same procedure as described in Section 5.8.3. The effect of the pinhole position will also be explored to show how the lateral drift of the cavity away from the optical axis affects the collection as well as how the rotation of the cavity mode affects the response in collected intensity when applying aberrations. The intensity profiles of the TEM$_{01}$ cavity mode under the effects of different aberrations being applied to the cavity mode wavefront are shown in Figure 44.

Most of the intensity profiles show a reduction in intensity when the aberrations are applied to the wavefronts of the TEM$_{01}$ mode. Significant changes are observed when coma aberration is applied. The coma x aberration shows the effect of shifting the intensity distribution along the x-axis, so the intensity of one lobe increases while the intensity of the other lobe decreases.

The effects of the aberrations on the TEM$_{01}$ mode and the other cavity modes are shown in Figures 45 and 46 when the pinhole is collected in two different positions. Figure 45 collects intensity from one of the brightest lobes of the mode, and Figure 46 collects the intensity from the centre of the cavity mode. The results of the TEM$_{10}$, TEM$_{20}$, TEM$_{30}$ and TEM$_{21}$ cavity modes have been excluded because they show similar results to their rotated equivalents (TEM$_{01}$, TEM$_{02}$, TEM$_{03}$ and TEM$_{12}$) but the response in intensity occur in the coma y aberration instead of the coma x aberration.

In Figure 45, the changes in intensity show that the coma aberrations in general, will increase the intensity of the collected lobe. The cavity modes that have lobes in the x-axis (TEM$_{01}$, TEM$_{02}$, TEM$_{03}$) show improvement with coma x aberration whilst the cavity modes with lobes along both the x and y-axis (TEM$_{11}$, TEM$_{12}$) show improvement with both coma x and coma y aberration. This can be interpreted as the coma aberration shifting the intensity of the lobes along the axis of the coma aberration.

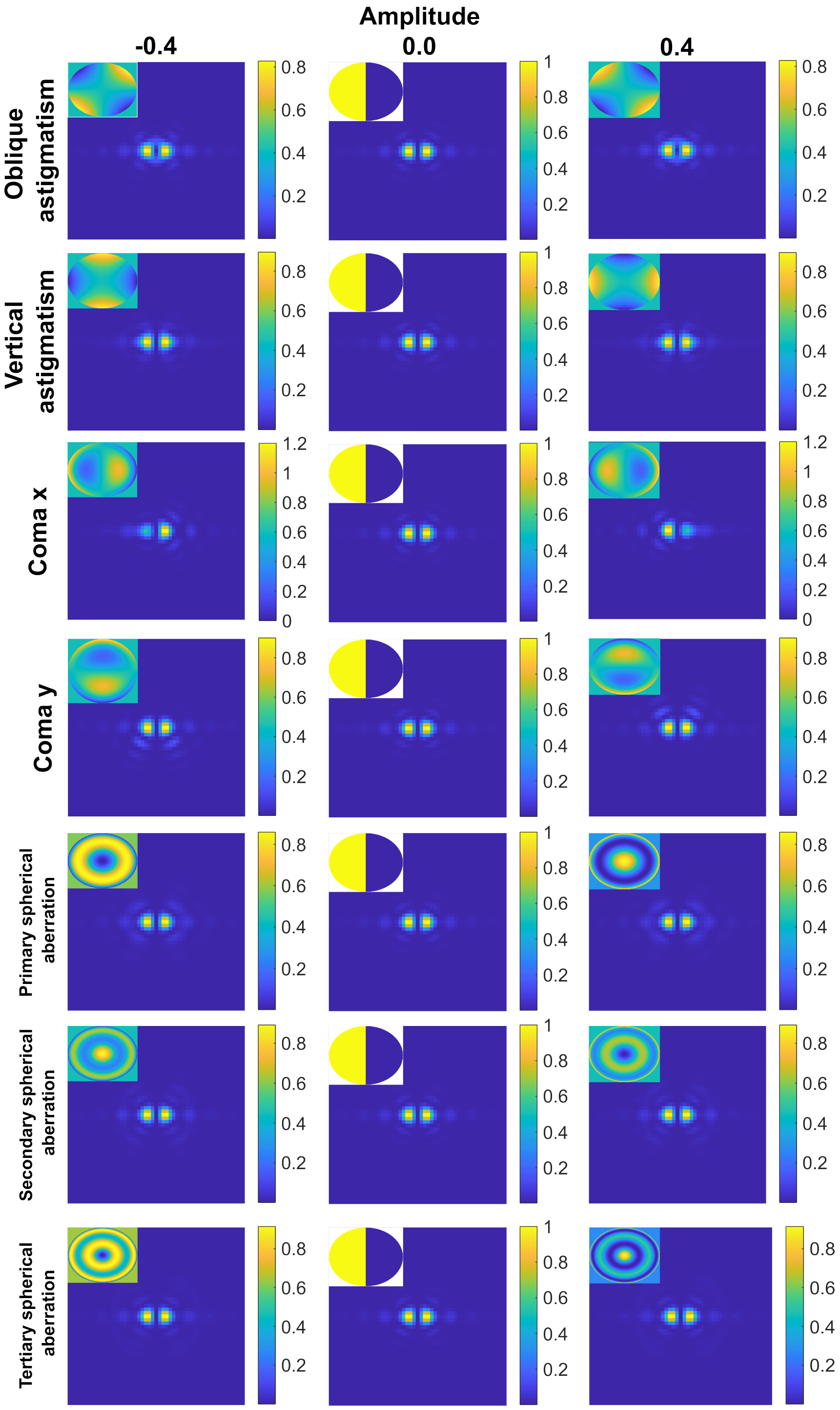

Figure 44: Intensity profiles of the TEM$_{01}$ mode under the effects of aberrations applied to the wavefront. The theoretical applied aberration profiles are shown in the inset of each Figure. For comparison, the phase profile for the TEM$_{01}$ mode is shown in the inset of the figures for the central column.

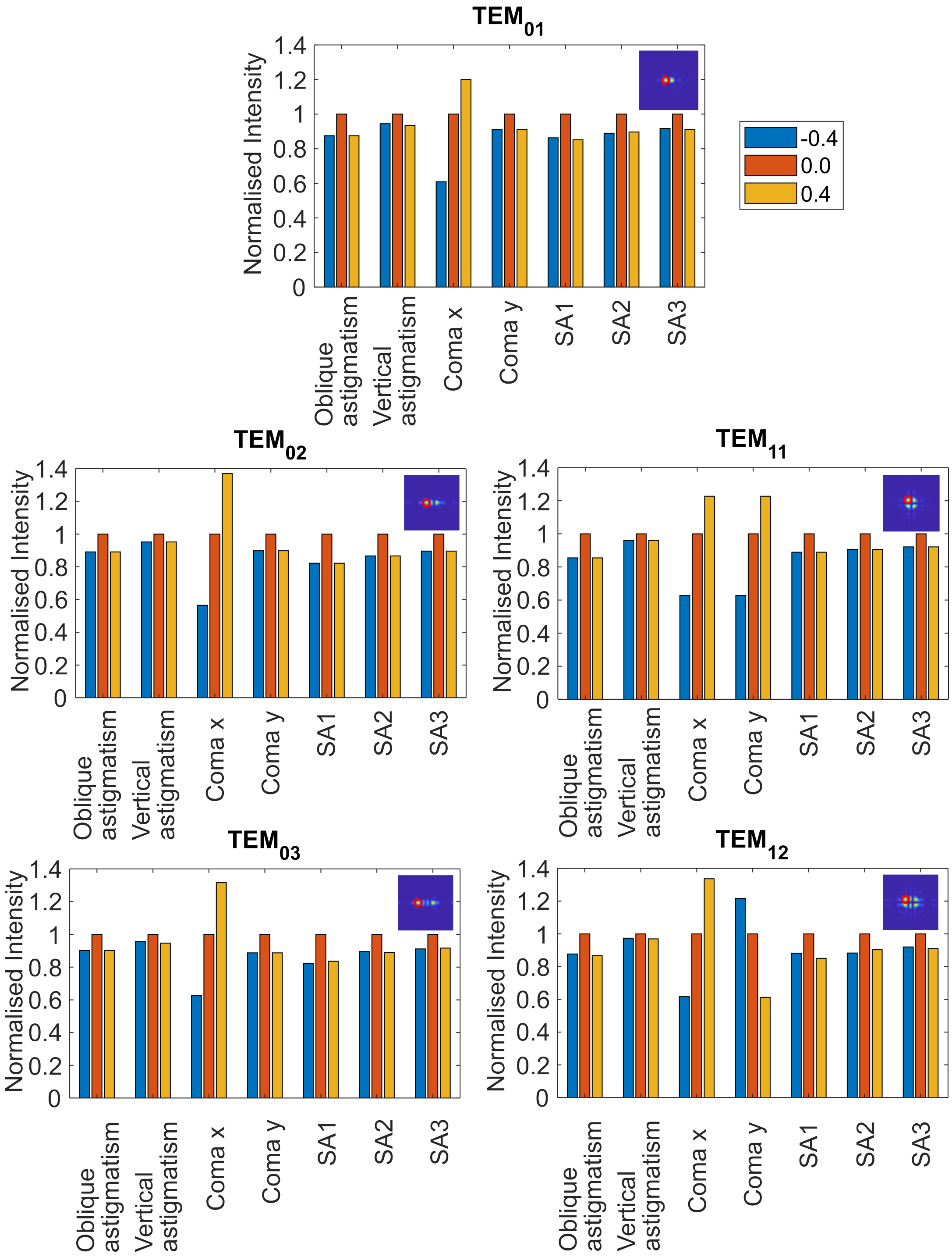

Figure 45: Bar plots of the normalised intensity of the upper leftmost brightest lobe circled of the cavity modes under the effects of aberrations with different amplitudes. The lobe intensity that is collected by the pinhole is circled in red.

Figure 46, shows a different response in collected intensity when collecting intensity from the centre of the cavity mode. The collected intensity increases only with oblique astigmatism for the cavity modes with lobes in both directions (TEM$_{11}$ and TEM$_{12}$).

9.3.4 Effects of aberration correction on rotated cavity modes

The axis of the cavity modes could be rotated relative to the axis of the deformable mirror, which will change the response of the collected intensity when aberrations are applied. This effect can be studied in the model by rotating the wavefront of the applied Zernike polynomial. Figures 47 and 48 show the responses of the collected intensity of the cavity modes when collecting light from the brightest upper left lobe and the centre of the mode respectively.

When the intensity is collected from one of the brightest lobes, the effect of rotation changes the response in intensity when applying the coma aberrations. Previously, for the cavity modes with the lobes along the x-axis (TEM$_{01}$, TEM$_{02}$ and TEM$_{03}$), the coma x aberration had the effect of shifting the intensity distribution of the lobes along the x direction. The effect of rotation reduces the response in intensity with coma x aberration as the direction of the cavity lobes rotates away from the x-axis and increases the response with coma y aberration.

In Figure 47, the TEM$_{01}$, TEM$_{02}$ and TEM$_{03}$ modes show that the 45° rotation reduces the response with coma x aberration and increases the response with coma y aberration to have equal absolute change in intensity with amplitude. For the cavity modes with lobes in both directions of the axes, the rotation has the effect of shifting the response in intensity with both directions of coma aberration to one direction. This is seen in the TEM$_{11}$ and TEM$_{12}$ modes where the 45° rotation has shifted the response in intensity to only the coma y aberration.

When the intensity is collected from the centre of the cavity mode as shown in Figure 48, there is only a change in response for the cavity modes with lobes in both directions. For the TEM$_{11}$ and TEM$_{12}$ modes, the effect of the 45° rotation reduces the intensity change with oblique astigmatism and increases the change with vertical astigmatism until the response is entirely dependent on vertical astigmatism.

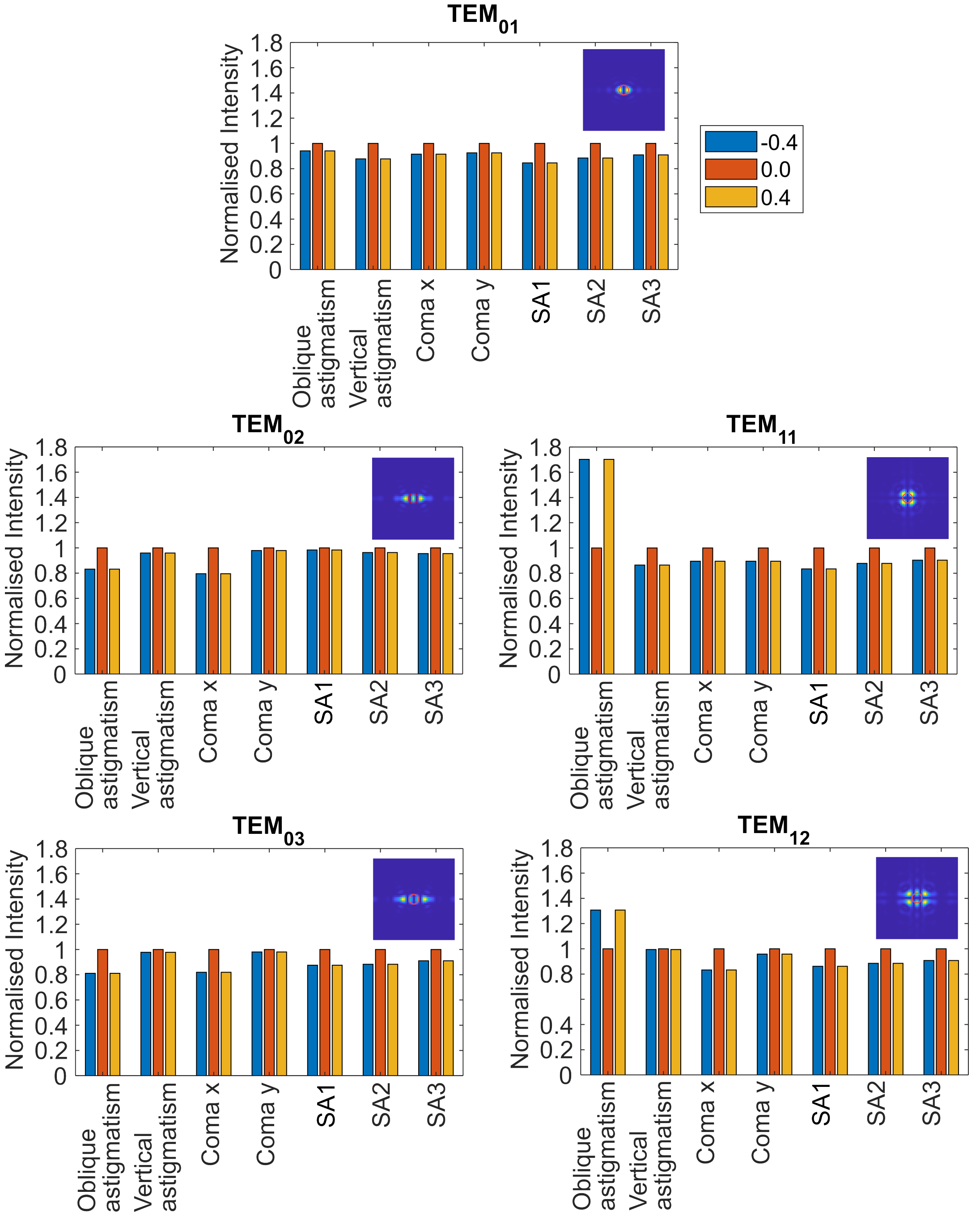

Figure 46: Bar plots of the collected intensity of the cavity modes under the effects of aberrations with different amplitudes when the light is collected in the centre of the cavity mode.

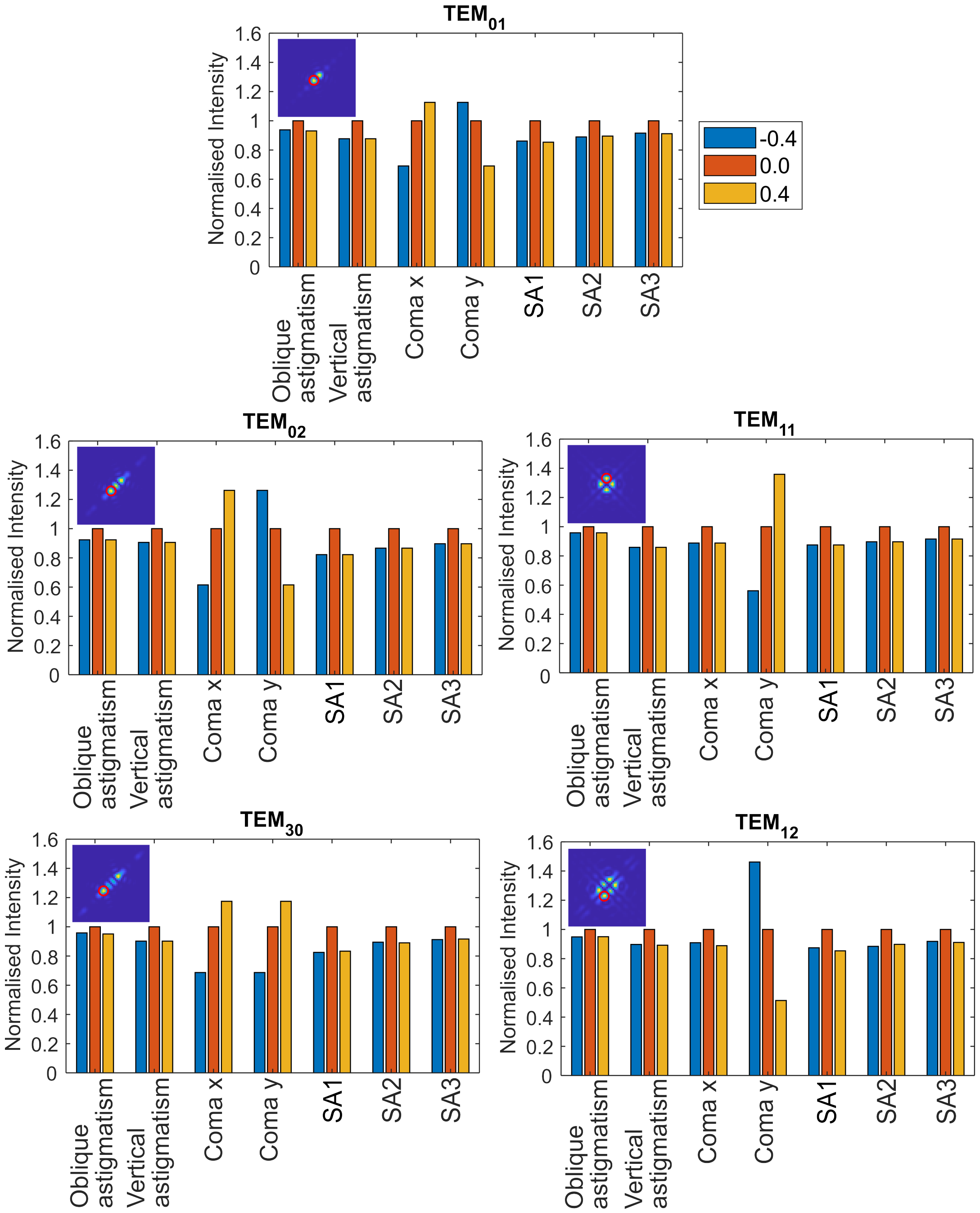

Figure 47: Bar plots of the normalised intensity of the lobe circled in red of the cavity modes rotated 45°clockwise under the effects of aberrations with different amplitudes.

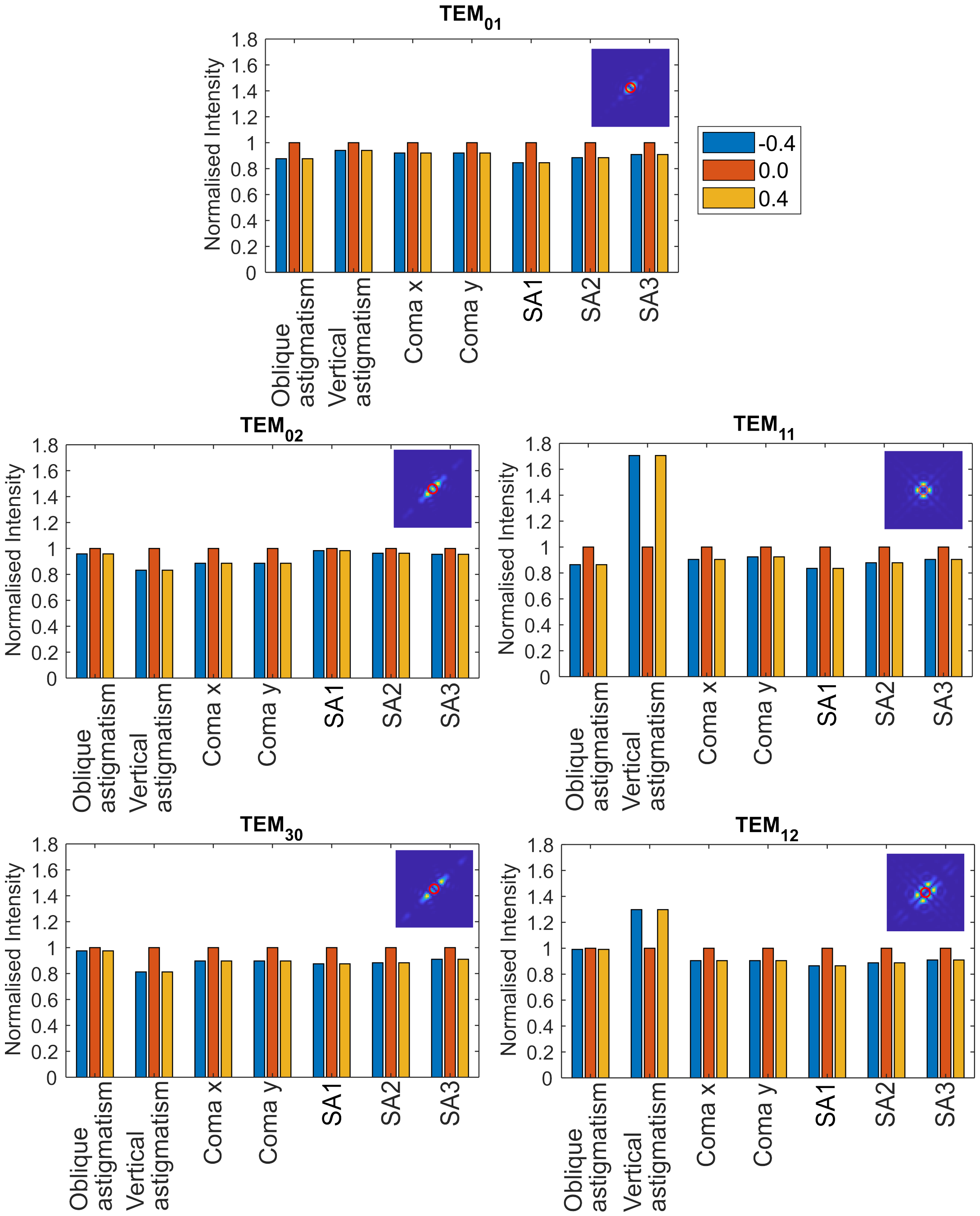

Figure 48: Bar plots of the normalised intensity collected in the centre of the cavity modes rotated 45°clockwise under the effects of aberrations with different amplitudes.

From the results of the model, the effect of applying aberrations appears to shift the intensity of the cavity mode laterally. Applying coma aberrations will shift the intensity of the cavity mode along the direction of the coma aberration, as shown for the TEM$_{01}$, TEM$_{02}$ and TEM$_{03}$ modes. Appling astigmatism shifts the intensity towards the centre of the cavity mode, which can be seen for the TEM$_{11}$ and TEM$_{12}$ modes. The effects of rotating the cavity mode axis relative to the deformable mirror axis shift the intensity response from having responses with single components of coma to having responses with both components of coma and vice versa. For astigmatism, the effect of rotation shifts the astigmatism response towards the other component, which previously had no response with no rotation.

This analysis may explain the observation in the increases in intensity with coma aberration for the *(l+m)=1*, *(l+m)=2* and *(l+m)=3* cavity mode peaks and how there was a increase in intensity with astigmatism for the *(l+m)=2* and *(l+m)=3* cavity mode peaks. The model also did not show any improvements when applying any of the spherical aberrations.

9.4 Discussion

From the power saturation measurement, the increase in effective saturation intensity (3%) compares well with the spherical aberration model for the microcavity, which predicted around a 3% loss. However, this cavity was primarily coupled to a higher-order TEM$_{01}$ mode. Since the spherical aberration model is only dependent on the substrate thickness, substrate refractive index and NA, the result should be consistent for the higher-order modes.

A spectral investigation on the effects of the individual aberrations on the intensity of higher-order cavity modes was made to observe how the aberrations affect the collection of higher-order cavity modes. For the fundamental TEM$_{00}$ peak in both measurements, the spherical aberration sweeps showed little to no increase. This suggests that the collection was near optimal to the Zernike polynomial amplitudes set before closing the cavity and that there was little to no spherical aberration in the cavity mode. The astigmatism and coma amplitude sweeps showed that there is an increase in the TEM$_{00}$ mode collection with astigmatism and coma aberration, which was not predicted by the Zernike polynomial fit. This may be explained by the TEM_{00} peak overlapping with higher-order transverse modes with a lower longitudinal mode (q-1). The increase could also be explained by the concave mirror shape having some ellipticity. This could form an elliptical cavity mode, which introduces astigmatic aberration and can be corrected for by aberration correction.

For the higher-order modes, there was an increase in intensity when sweeping the second- and third-order spherical aberrations, as well as the coma and astigmatism aberrations. For the spherical aberrations, there was a significant increase in intensity of around 60 % with the first measurement shown in Figure42. However, it was not observed for the second measurement. This observation could not be explained by the spherical aberration model, Zernike polynomial fits to the wavefront or the intensity profile modelling.

For the coma aberrations, the Zernike polynomial fits showed that the $(l+m)_{odd}$ cavity modes had components of coma aberration, so applying coma correction was expected to improve the collection of the cavity mode. This was observed in the sweeps in Figure 42, but for the second measurement in Figure 43, applying coma aberration showed increases in intensity for the *l+m=2* cavity mode peak. From the cavity intensity profile modelling shown in Figure45, the effects of coma increase the intensity for the *l+m=1*, *l+m=2* and *l+m=3* cavity modes if the pinhole is collecting the light from one of the brightest cavity lobes. This may explain the results of the experiment if the cavity had drifted laterally so the pinhole was collecting light from one of the brighter lobes.

For astigmatism, the Zernike polynomial fits showed that the $(l+m)_{even}$ cavity modes had significant components of astigmatism. This was generally supported by the significant increases in intensity with astigmatism, which were seen with the *l+m=2* cavity modes, but the *l+m=3* cavity modes also showed improvement with astigmatism. From the intensity profile modelling results in Figure 46, the TEM_{11} and TEM_{12} cavity modes showed an increase in collection with astigmatism when the pinhole is positioned to collect light from the centre of the cavity mode. This could explain the increases in intensity for the l+m=2 and l+m=3 cavity modes.

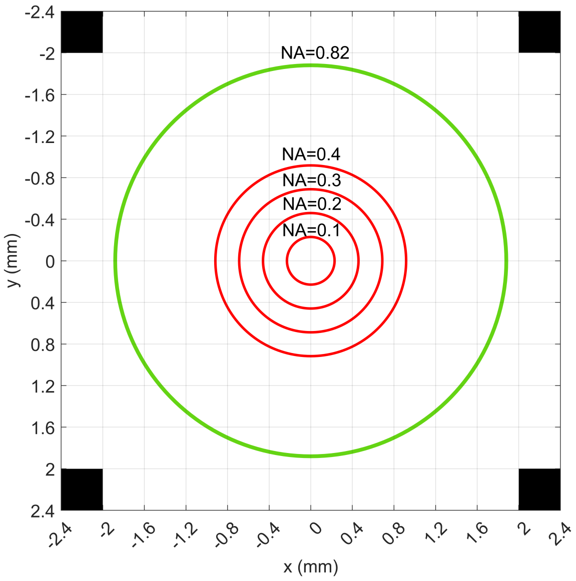

Figure 49: Rings of the apertures exposed on the deformable mirror for different values of NA. The aperture of maximum NA is $\mathrm{NA}_{obj} = 0.82$ is shown by the green ring and the red rings show the possible apertures of the cavity modes.

The reduced NA of the cavity mode emission also limits the ability of the deformable mirror to apply aberration correction. The reduced NA will result in a smaller beam diameter of the collection emission and a smaller area exposed to the deformable mirror. This is shown in Figure 49, where the circles represent the beam diameter of the collected light for different values of NA. The NA values used in the power saturation and multi-mode analysis were 0.35 and 0.13 respectively. The Zernike polynomials are applied to the deformable mirror actuators that affect the area of the full aperture of the objective lens (NA = 0.82). When the NA of the emission is reduced, the collected wavefront only becomes affected by the central part of the Zernike polynomial, which reduces the ability to apply aberration correction. Even if the Zernike polynomial were applied to a smaller diameter of the deformable mirror, there would be fewer actuators to apply the Zernike polynomial across, which limits the shape of the profile the deformable mirror can apply and reduces the aberration correction.

Within the scope of cavity coupling to the ZPL of the NV centres, the ZPL will be primarily coupled to the TEM_{00} mode, so the main source of aberrations will be from the spherical aberration introduced when transmitting through the mirror. The correction of spherical aberrations has shown low improvement in intensity because of the low NA of the cavity modes. This may become more significant when using shorter cavity lengths for strong coupling of microcavities.

9.5 Conclusion

In summary, an aberration model is presented looking at how spherical aberration introduced through the planar mirror of the hemispherical microcavity affects the collection efficiency. The losses associated with spherical aberration were predicted to be low due to the low numerical aperture of the cavity mode emission and the thin mirror substrate thickness. This was supported by the power saturation intensity measurement and the spectral measurements on the TEM_{00} mode. This model will be useful for modelling the spherical aberration of NVs coupled to Fabry-Pérot microcavities where the cavity mode transmits through the mirror substrate, especially when the numerical aperture of the cavity mode emission is expected to be high or thicker mirror substrates are used.

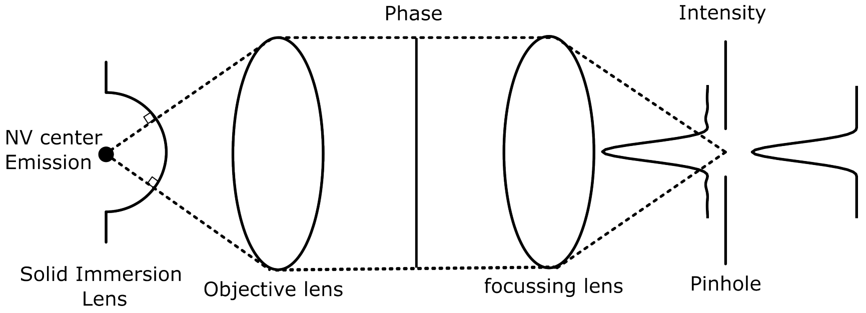

Figure 50: Schematic of the confocal system collecting light from a NV centre under a SIL.

10 Aberrations in solid immersion lenses

10.1 Introduction

Solid immersion lenses (SIL) are another method for enhancing light collection from NV centres. SILs have been used to improve the entanglement rate between NV centres[17] by enhancing the collection efficiency. A schematic of light collection of an NV centre through a SIL is shown in Figure 50. When the NV is positioned in the centre of the SIL, the SIL maximises the collection by ensuring the NV emission radiates at normal incidence to the surface of the SIL, so no spherical aberration is introduced when the emission exits the diamond/air interface. However if the NV centre is positioned off-centre, there will be rays of emission that hit the surface of the SIL at non-normal incidence, which will lead to an aberrated wavefront and less light collection into an optical fibre. In this chapter, a theoretical model is presented for modelling the aberrations and collection loss of the emission when the emitter is displaced axially and laterally from the centre of the SIL. Then, the experimental results of aberration correction for an NV centre in a diamond monolithic SIL will be shown for comparison with the model.

10.2 Aberrations from axially displaced emitters

For calculating the aberrations in a SIL, the aberration can be calculated similarly for focusing through a planar interface with a different refractive index, as shown in Section 5.8.3. Consider the ray geometry in Figure 51a. It shows a sector of the SIL, which represents the surface of the

SIL with a radius r on the cylindrically symmetric axis z and ρ. The optical axis is defined to be along the z axis and D will be the point of focus or the position of the point source along the optical axis. The $\overrightarrow{OD}$ vector represents the displacement of the point source along the optical axis of the SIL and the magnitude is represented by the length d. For a ray focusing to the point D at an angle γ relative to the optical axis, l_1 and l_2 represent the relative pathlength of the rays focusing to the point D in free space and within the SIL respectively from the objective.

Figure 51b shows the geometric relationships between both ray paths and the SIL. Snell's law relates θ_1 and θ_2 with respect to the normal incidence on the SIL, represented by $\overrightarrow{OR}$. Using trigonometric relationships, Snell's law and the sine rule, the following relations can be derived.

$$l_1 = l_2 \cos\theta_3 \tag{10.1}$$

$$\frac{l_2}{\sin\alpha} = \frac{r}{\sin\beta} = \frac{d}{\sin\theta_2} \tag{10.2}$$

$$\gamma = \theta_1 + \alpha \tag{10.3}$$

$$\theta_1 = \theta_2 + \theta_3 \tag{10.4}$$

Equation 10.2 can be rearranged to Equation 10.5 to solve for θ_2. Equation 10.5 can be numerically solved to calculate the path length difference (Equation 5.44) for each of the ray angles to calculate the phase profile in the pupil plane. Equation 10.5 can then be used to find the phase profile for values of displacement of the point source emitters from the centre of the SIL along the optical axis d.

$$\frac{\sin\left(\gamma - \arcsin\left(\frac{n_2}{n_1}\sin\theta_2\right) + \theta_2\right)}{\sin\theta_2} = \frac{r}{d} \tag{10.5}$$

For calculating the wavefront for axially displaced emitters, there is rotational symmetry around the optical axis simplifying the calculation to one dimension. The phase aberration profiles

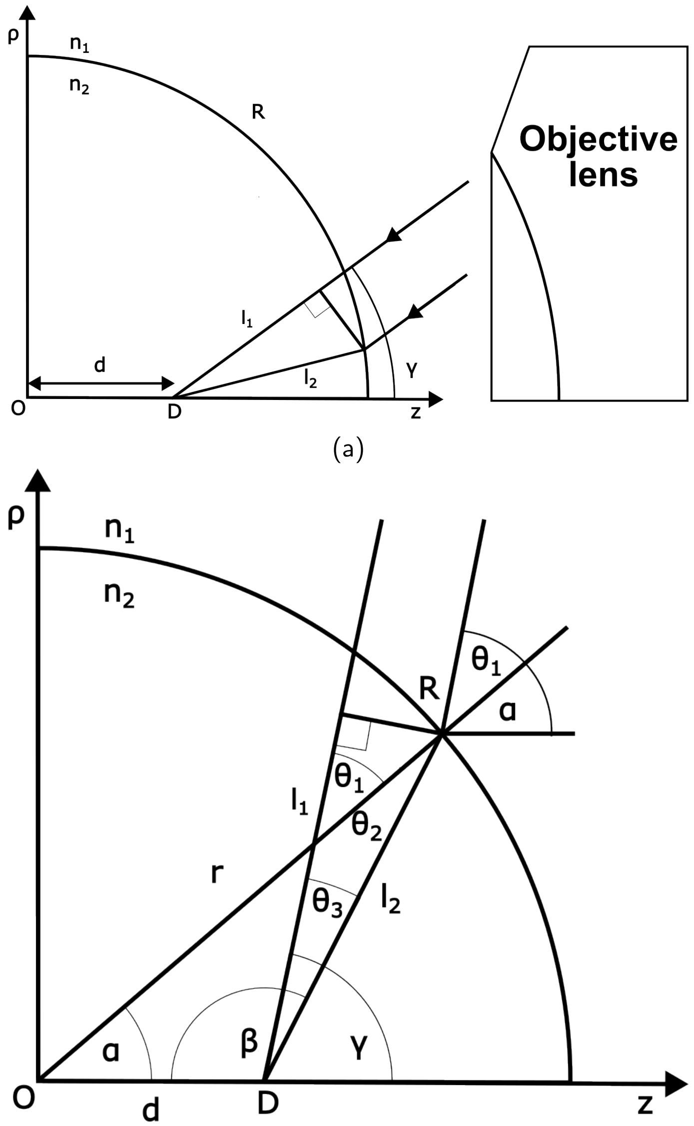

(a)

(b)

Figure 51: Ray (a) and Geometric (b) schematics of the ray paths focusing into a SIL at the point D along the optical axis z. The ray paths l_1 and l_2 represent the rays focusing in free space and in the SIL respectively. The refractive index of the SIL is n_2 and a radius r.

have been fitted to the radially symmetric Zernike polynomials to break down the aberration function into components of defocus and 1st, 2nd and 3rd order spherical aberrations as shown

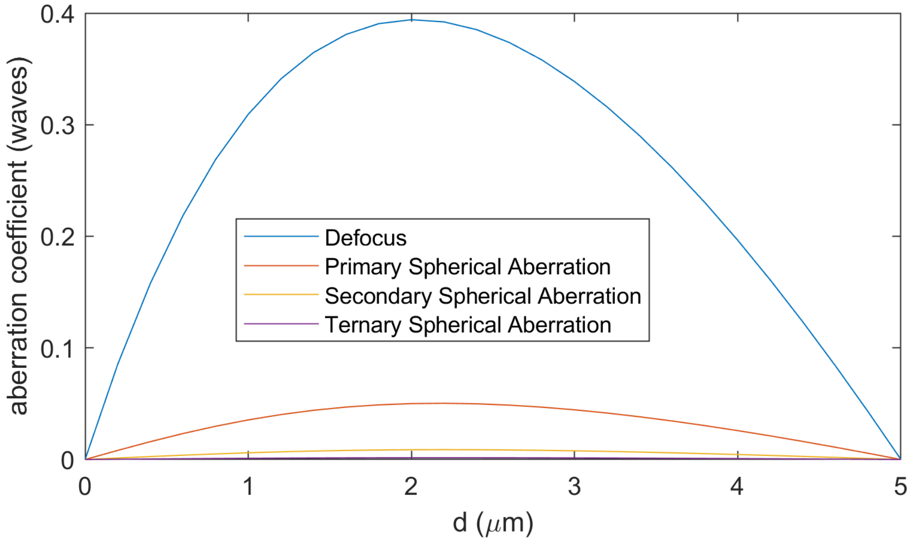

Figure 52: Graph of amplitudes of the rotationally symmetric aberrations for emitters displaced from the centre of the SIL (d=0) to the surface (d=r). Amplitudes are calculated for a $5\mu m$ diamond SIL ($n_2 = 2.4$) focused in free space ($n_1 = 1$) with $\lambda = 640nm$

in Equation 10.6.

$$\psi(r) = a_{20}Z_2^0(r) + a_{40}Z_4^0(r) + a_{60}Z_6^0(r) + a_{80}Z_8^0(r) + \psi_b \tag{10.6}$$

Where a_{n0} represents the coefficients of the Zernike polynomials and ψ_b represents the remaining phase. Figure 52 presents these aberration coefficients of the aberration function for a diamond SIL with a 5 μm radius for emitters placed between the centre of the SIL and the surface (0<d<r). The model is consistent with the expectations of zero aberration for focusing at the centre of the SIL (d=0) and at the surface of the SIL (d=r). The defocus aberration is the main component of the aberration function for focusing along the optical axis of the SIL and can be easily compensated for. To observe the collection losses associated with spherical aberration, the phase profile is calculated using Equation 10.5 for different values of emitter displacement d, then the intensity is modelled by the same method shown in Section 5.8.3 with the defocus aberration removed from the phase profile. Figure 53 shows that the maximum intensity loss due to spherical aberration is ~2% for focusing on any defect between the centre of the SIL

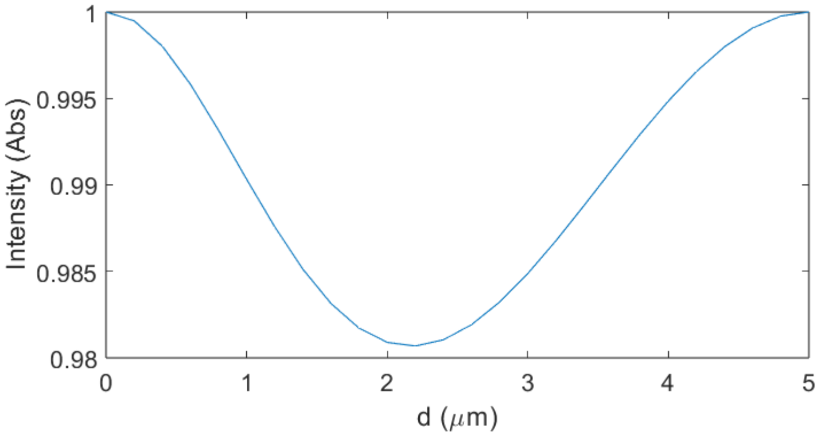

Figure 53: Intensity profile for the collected intensity from the SIL focused at a point source axially displaced from the centre of the SIL. The losses associated with defocus aberration have been removed.

and the surface. This indicates that there is a high tolerance for positioning error along the optical axis of the SIL.

10.3 Aberrations from laterally displaced emitters

For modelling optical emitters that are displaced laterally off the optical axis, the schematic for modelling the aberration function is shown in Figure 54. Figure 54 shows schematics of spheres which represent the SIL in 2D (a,b) and 3D (c,d), where the emitters are displaced axially (a,c) and laterally (b,d) to the optical axis. The ray paths of the aberrated and non aberrated rays are shown as dashed lines in Figure 54a and the contour lines represent the ray angle γ of the non aberrated ray relative to the optical axis. Each contour line represents a constant angle γ relative to the forward direction on the optical axis and also represents a constant phase difference associated with γ.

The aberration profile can be built by finding the phase difference for each ray within the cone of the NA. For axially displaced emitters and using radial symmetry, this can be simplified to finding the phase difference for the different angles relative to the optical axis γ. In 3D, this can be interpreted as sampling the phase difference for the contour lines within the intersected area between the NA cone and the SIL surface, which is outlined in red in Figure54c.

For modelling laterally displaced emitters, the phase profile can be obtained by rotating the numerical aperture cone so that it is perpendicular to the z axis. This is illustrated in Figure 54d, and the aberration profile can then be calculated by finding the phase differences of the rays within the intersected area between the NA cone and the SIL surface, which is also outlined in red. Since the phase differences are rotationally symmetric along the z axis, the phase difference of these rays can be determined by finding the relative angle of the ray to the z axis (γ) and finding the phase difference for that ray within the intersected area of the cone. This method can be extended to find the aberration profiles for emitters that are both axially and laterally displaced. Before presenting the results, the limitation of emitter displacement d will be introduced for modelling emitters with lateral displacement. There is a limit in the maximum displacement from the centre of the SIL before the maximum refraction angle ($\theta_1 = 90°$) out of the SIL will limit the angles of light that the numerical aperture can collect. This is shown in Figure 55 where the shaded area shows the region of rays within

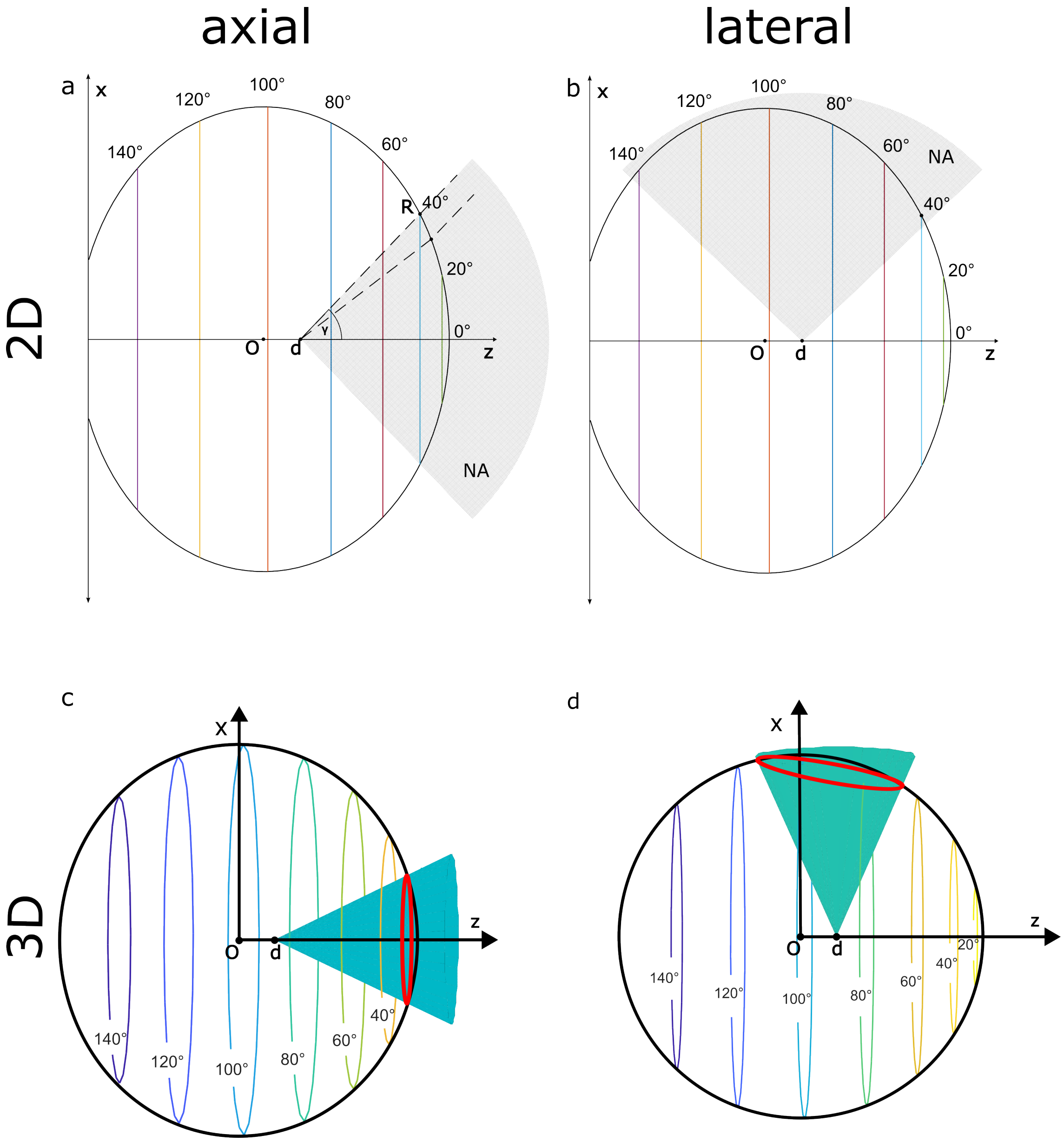

Figure 54: Schematics for determining the aberration function for (a,c) axially or (b,d) laterally displaced emitters on the SIL in 2D (a,b) and 3D (c,d). The contour lines represent the phase differences for the rays towards the emitter for different angles relative to the optical axis. The dashed lines represent the aberrated and non aberrated rays to the emitter for a ray 40° from the optical axis. The shaded area represents the cone of rays that are used to determine the aberration profile.

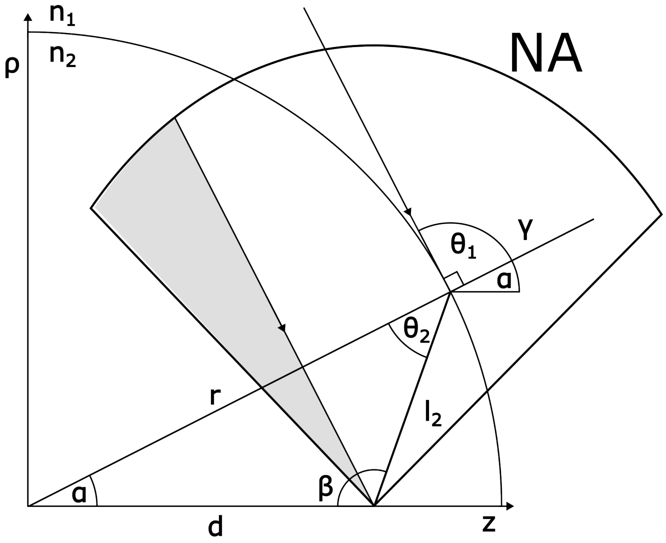

Figure 55: Schematic of a segment of a SIL showing the maximum possible limit of a ray being refracted from the point source. Any ray angle beyond this limit will not be collected by the numerical aperture shown as shaded within the NA cone.

the NA cone that will not be collected. This limit can be derived by solving for d under the conditions of $\theta_1 = 90°$ and $max(\cos(x)) = 1$ and the solution is shown in Equation 10.7. When the displacement exceeds this limit ($d > d_{max}$), the maximum angle of γ is reduced. Any rays within the NA cone and beyond this angle will not be collected on the refracted path and will apodize the aberration function. This relationship is presented in Equation 10.8. For the 5 μm radius diamond SIL, d_{max} is 2.08 μm and the following results will present the aberrations and normalised intensities within the range of $0 < d < 2\ \mu m$.

$$d_{max} = \frac{r\,n_1}{n_2} \tag{10.7}$$

$$-\frac{r\,n_1}{d\,n_2} = \cos(\theta_2 + \gamma_{max}) \tag{10.8}$$

The components of the radially symmetric and asymmetric aberrations for the laterally displaced emitters are shown in Figures 56a and b respectively. The majority of the aberrations introduced by lateral displacement appear to be from primary coma and vertical astigmatism. For low values of lateral displacement of the emitter from the centre of the SIL, coma aberration is the major source of aberration, while at higher displacement, astigmatism becomes the major source of aberration. The results of how the aberrations that are introduced by different amounts of lateral and axial displacement of the emitter, affect the collected intensity are presented in Figure 57. The axial and lateral displacement are represented in polar coordinates (d,η) where d represents the displacement from the centre of the SIL and η represents the angle between the optical axis of the NA cone and the vector from the centre of the SIL to the point of the emitter ($\overrightarrow{OD}$). The defocus component of the aberration is removed to examine the effect of aberrations that cannot be as easily corrected for.

The reduction in intensity with increasing emitter displacement is minimal for axially displaced emitters ($\eta = 0°$). For increasing amounts of lateral displacement, the angle of ρ increases and the reduction in intensity becomes more severe for higher amounts of displacement from the centre of the SIL.

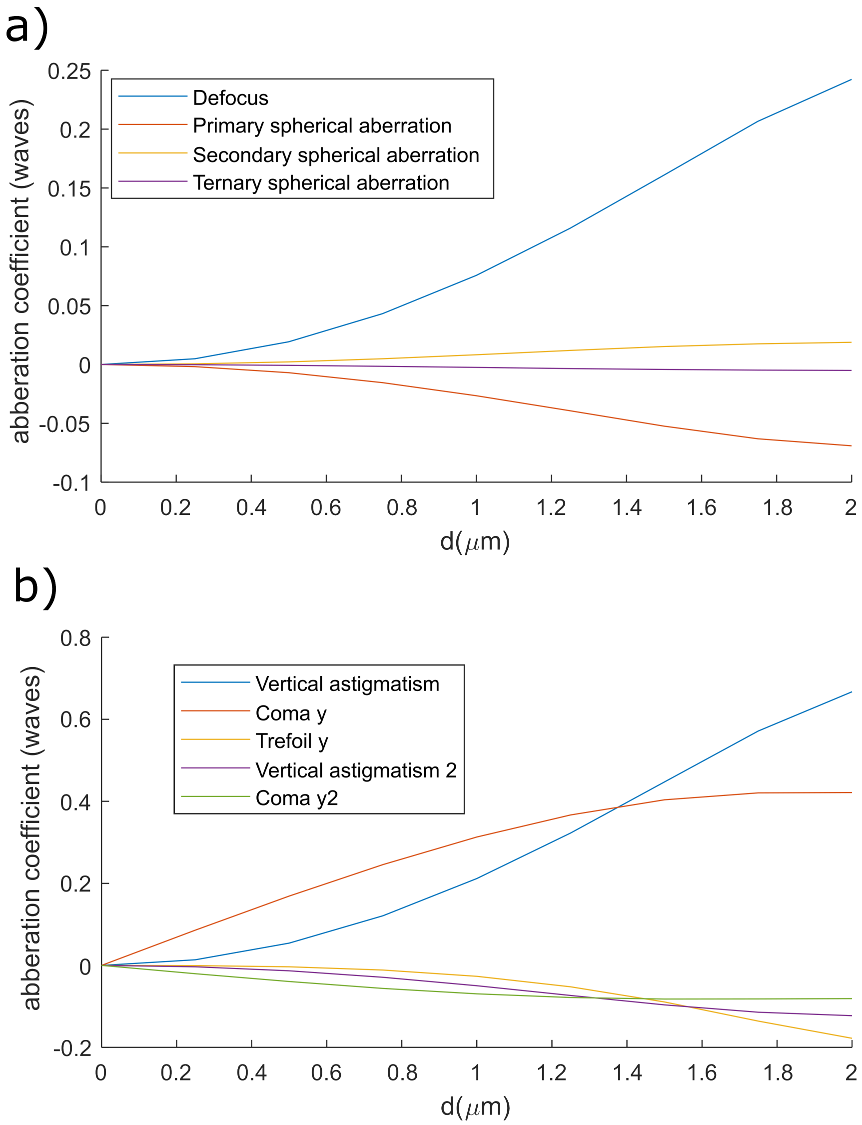

Figure 56: Plots of the components of the radially symmetric (a) and non radially symmetric (b) Zernike polynomials for the aberration wavefront for emitters displaced laterally across the SIL. The SIL modelled was a $5\mu m$ radius diamond ($n_2 = 2.4$) SIL focused through air ($n_1 = 1$) using a NA=0.82 objective lens.

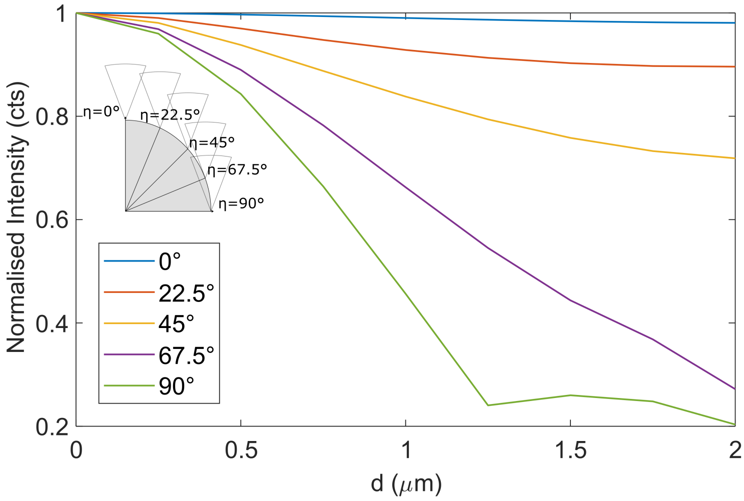

Figure 57: Intensity plots of the modelled intensity vs displacement from the centre of the SIL described in polar coordinates (d, η). Each plot represents a different angle of displacement relative to the optical axis where $\eta = 90^\circ$ represents lateral displacement and $\eta = 0^\circ$ represents axial displacement. The schematic shown in the graph shows the direction of the emitter displacement relative to the optical axis.

10.4 Monolithic SIL

The monolithic SILs were fabricated by FIB milling the SIL structure around a selected NV centre. The fabrication begins with electronic grade CVD diamond from Element Six being prepared by initially etching away 20 μm of the surface using Inductively Coupled Plasma (ICP). A grid pattern is also FIB milled on the diamond surface to provide a visible reference for both the FIB and laser writing systems. The NVs were fabricated 5 μm deep within the grid by initially forming GR1 vacancy centres using the laser writing process and then thermally annealing the sample to diffuse the vacancies to nearby nitrogen to form the NV centre. The FIB milling and laser writing of NV centres were performed by Shazeaa Ishmael and Andrew Kickpatrick respectively. The thermal annealing was performed in a vacuum furnace at 1000 °C for around 3 hours and was performed by Colin Stephen at Warwick University.

The NVs fabricated are then characterised using HBT and optical spectroscopy to identify single NV centres for FIB milling SILs over. The SIL was milled into the sample with a 5 μm radius and a 1 μm wide trench around the SIL. The trench will reduce the numerical aperture of the light that can be collected to around 0.77. Some of the NV centres were removed by the FIB milling process of a SIL, so another thermal anneal was used to recover some of the NV centres.[105] The thermal anneal recovered only one NV out of the eight NVs with SILs initially milled over them. Figure 58 shows confocal and SEM images of the SIL with the NV centre and the HBT characterisation of the NV centre. The second-order correlation fit evaluated at zero time delay ($g^{(2)}(0) = 0.11$) is less than one, indicating that the NV is a single emitter. The confocal xy scan in Figure 58(a) shows the NV is laterally displaced off centre from the SIL by around 0.8 μm and around 1 μm axially above the centre of the SIL. This would correspond to a physical displacement from the centre of the SIL of 5.33 μm at an angle relative to the optical axis of $\eta = 38.7°$. The amplitudes of the fitted Zernike polynomials to the aberrated wavefront for emitter displacement with $\eta = 38.7°$ are presented in Figure 59. From the SIL aberration model, a 6.4% decrease in intensity is predicted due to aberrations excluding defocus.

The results of the aberration sweep using the deformable mirror are presented in Figure 60. Most of the aberrations show no increase in collected intensity except for oblique astigmatism, which shows a $\sim 2\%$ increase in intensity when applying +0.4 waves of oblique astigmatism. This was not expected from the predictions shown in Figure 59b, where the SIL aberration was predicted to have 0.008 waves of astigmatism.

10.5 Discussion

The SIL model presented suggests that the collected intensity is more sensitive to lateral emitter displacements than to axial displacements. For axial displacement, the maximum loss was $\sim 2\%$ whilst for lateral displacement, the maximum loss was up to $\sim 80\%$. This would emphasise the importance of controlling the lateral position of the SIL relative to the emitter. This would be important for the application of stick-on SILs, where a hemispherical cap of a material is adhered on top of the diamond with NV centres to form the SIL.[108] Using stick-on SILs could also provide controlled lateral displacement of the SIL relative to the NV centre to use in the

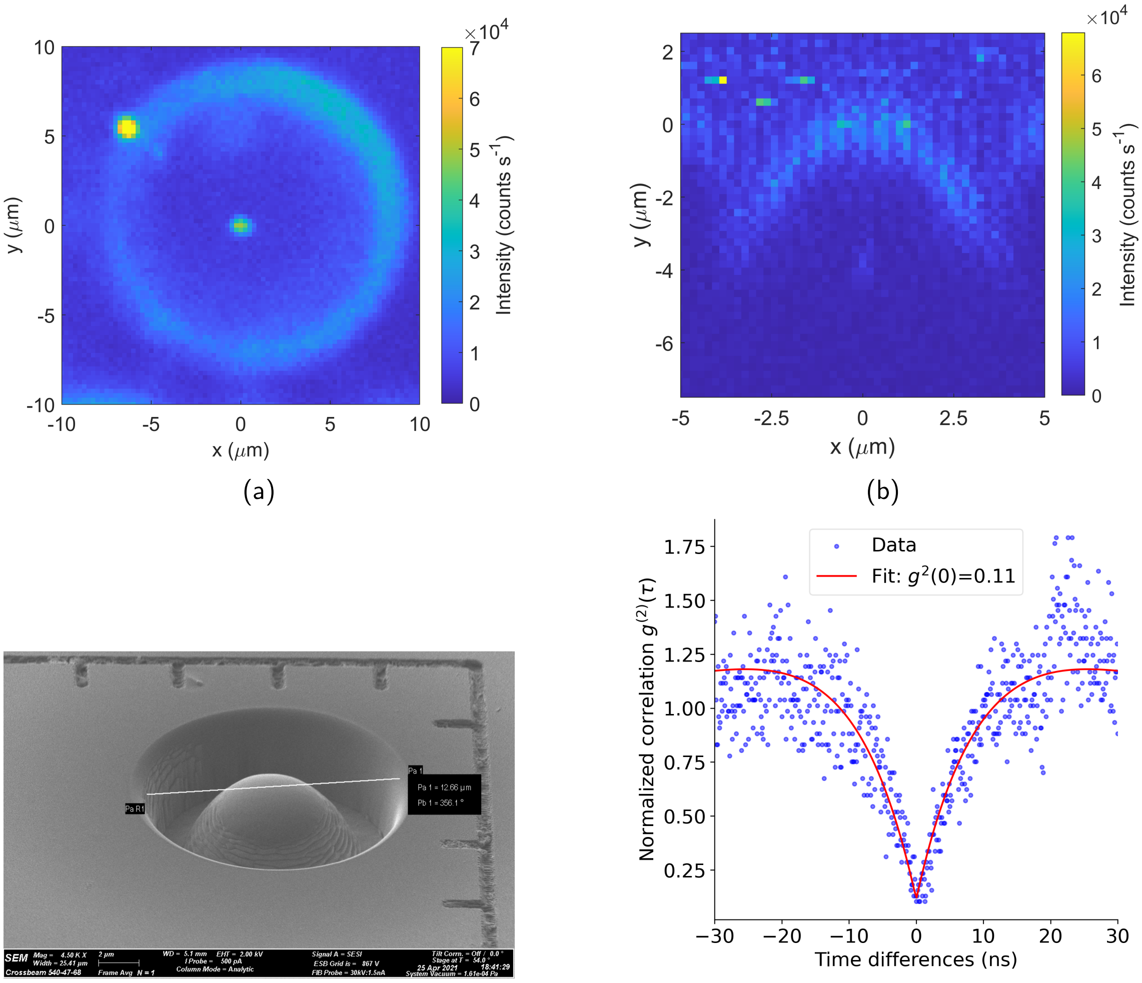

(a)

(b)

(c)

(d)

Figure 58: Confocal xy (a) and xz (b) scans of the NV centre in the monolithic SIL site B2, along with a SEM image (c) and HBT characterisation of the NV under the SIL (d). The xy scan was taken using a beam scanning system with a NA=0.9 air objective lens and the xz scan was taken with a stage scanning system using a NA=1.25 oil objective lens. The SEM image was taken by Shazeaa Ishmael. The HBT plot was fitted using Equation 6.5.

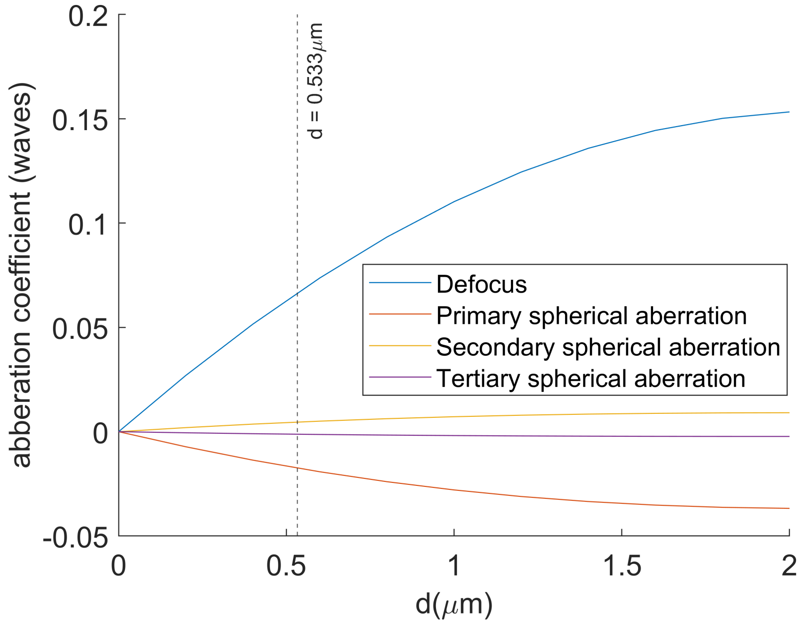

(a)

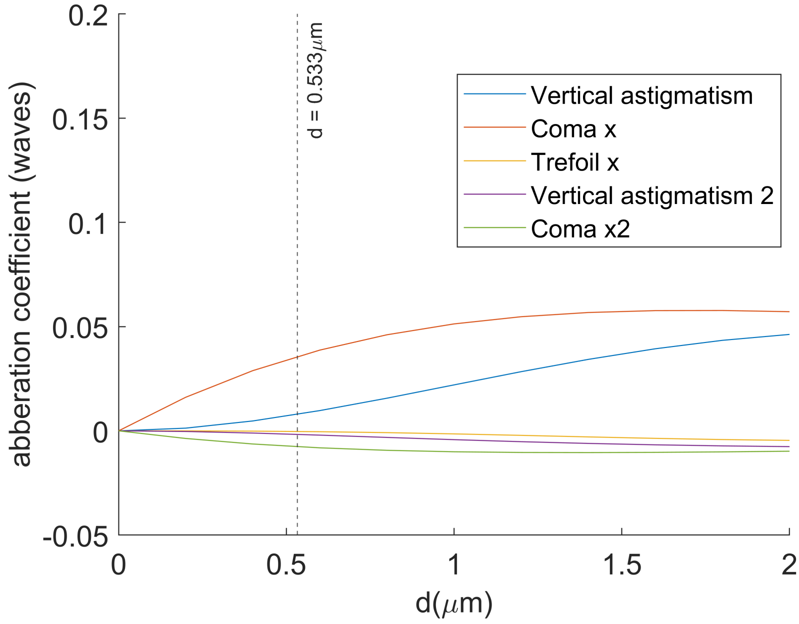

(b)

Figure 59: Plots amplitude of the radially (a) and non-radially (b) symmetric Zernike polynomials fitted to the aberrated wavefront of the SIL for emitters displaced at a length d from the centre of the SIL and at a 38°angle relative to the optical axis ($\eta = 38°$). The dashed vertical line indicates the displacement of the emitter in the monolithic SIL.

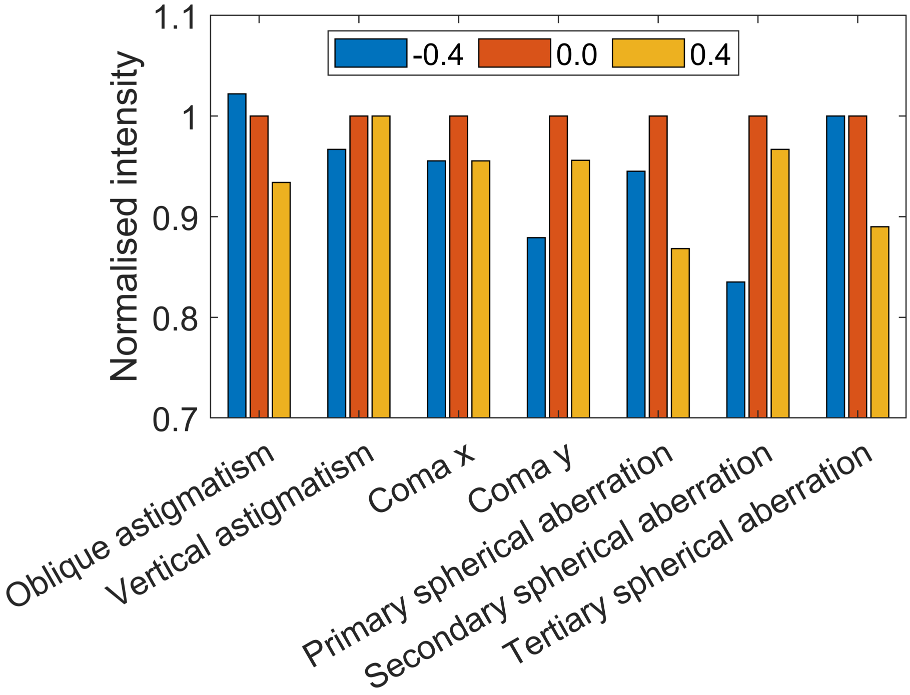

Figure 60: Aberration amplitude sweep on the SIL sample.

aberration correction experiment and to test the SIL aberration model. In Figure 57, there was also a local minimum on the intensity profile for the lateral displacement ($\psi = 90°$) at around d = 1.25 µm. This could be explained by the increasing component of vertical astigmatism, which becomes more significant than the coma aberration at d=1.38 µm seen in Figure 57.

The model has limitations in modelling only perfectly spherical SILs with an isotropic refractive index, so any shape imperfections and surface roughness cannot be modelled. For the aberration sweep on the monolithic SIL, the increase in intensity from applying +0.4 waves of astigmatism was not predicted in the aberration model. A possible explanation is that the shape of the SIL could be slightly elliptical. Another limitation was that the model assumed that light was radiating from a point source emitter, whereas single emitters tend to be dipole sources, so the radiation is not perfectly spherical. Polarisation of the radiation is also not considered, but can be implemented using Jones matrices.[133]

The aberration model is also inaccurate for modelling the aplanatic SIL condition ($d =$

$-\frac{r}{n_2}$), where it gives a non-zero component for spherical aberration, indicating that the model is only valid for modelling depths between the centre of the SIL and the surface. Goh and Sheppard have modelled the aplanatic SIL aberrations by using a different definition of path length difference.[134]

10.6 Conclusion

A SIL aberration model has been presented and shown for modelling a 5 µm radius diamond SIL, that axial displacements of the emitter in the SIL will result in <2% loss and lateral displacements can result in <80% loss. This suggests that lateral positioning of the SILs is more important than axial positioning to reduce the optical aberrations and maximise collection efficiency. When the model was compared to the experiment, the model was not able to predict the larger than expected component of astigmatism which is likely due to the imperfect shape of the SIL. Another method of modelling the SIL aberration would be to obtain the surface profile of the SIL and to use optical modelling software such as opticstudio to model aberration of point source emission under that surface profile.

11 Conclusions and Outlook

11.1 Conclusion

This thesis presents developments in addressing challenges towards developing cavity-coupled NV centres in diamond for quantum computing. The developments are: ZPL linewidth characterisation of laser-written and diffused NV centres to measure the quality of NVs formed by laser diffusion; implementing cavity fringe stabilisation for cavity locking to explore the feasibility of using cavity fringe stabilisation for quantum computing and the aberration study of microcavities and SILs to understand how the microcavity design and SIL positioning can affect photon collection efficiency.

In Chapter 7, the ZPL linewidths of the NVs fabricated in electronic grade diamond using the MHz laser writing and diffusion process were characterised using PLE. The average of the ZPL linewidths for all of the NVs characterised was 186 MHz. Out of the six NVs characterised, one NV showed a 60.3 MHz average linewidth, which is within the target linewidth (<100 MHz) for generating entanglement.[89] From the power saturation fit, the linewidths measured were power broadened suggesting that the natural linewidth is narrower.

In Chapter 8, the cavity fringe stabilisation was demonstrated with cavity-coupled NV centres to maintain the cavity length to within 0.13 nm. When the cavity was coupled to the phonon side-band during ODMR, the fringe stabilisation was able to maintain coupling against the drift introduced by the microwave heating.

A deformable mirror was calibrated and implemented into a beam-scanning confocal microscope to study the aberrations from the microcavities and solid immersion lenses. In Chapter 9, a model of the spherical aberration introduced by transmission through the cavity mirror substrate is presented as a function of mirror substrate thickness and the NA of cavity mode emission. For the microcavities used in this thesis, the NA of the cavity emission was expected to be <0.4 and the maximum predicted losses due to spherical aberration associated with NA were <10%. This model was supported by power saturation measurements on a 5 μm RoC hemispherical cavity, where the effective saturation intensity increased around 3% after aberration correction. This value compared well to the predicted gain of 2.8% from the aberration model. The effects of aberration correction on the higher-order TEM modes were also explored. The Zernike polynomial fits to the TEM wavefronts predicted that the collection of the TEM modes with (l+m)$_{odd}$ values of the transverse mode index would be affected by the correction of the $Z_n^{m_{odd}}$ aberrations and for the (l+m)$_{even}$ modes would be affected by the correction of the $Z_n^{m_{even}}$ aberrations. However, this prediction was not always consistent with the observations found in the measurements. Further theoretical intensity modelling by considering the lateral position of light collection showed that applying coma aberration can shift the intensity distribution across the lobes of the cavity, and that applying astigmatism can shift the intensity towards the centre of the cavity mode. This meant the collection efficiency also depended on the area of the cavity mode that was collected by the pinhole. Whilst the results from the cavity aberration model showed low losses for the microcavities in this thesis, the spherical aberrations would be more severe for higher NA cavities and they would need to be corrected to maximise photon collection.

In Chapter 10, the aberrations introduced from the positioning error of the SIL relative to a point source emitter were explored. The aberration from point source emitters within a SIL was modelled for emitters displaced along the optical axis from the centre of the SIL and for emitters displaced laterally from the centre of the SIL. The aberration model predicted that the aberrations introduced from lateral displacement of the emitters can introduce <80 % loss in collection efficiency, whilst for axial displacement, <2 % loss in collection efficiency was predicted, indicating the importance of lateral positioning of SILs. From the experiment, there are only increases in intensity with astigmatism, which may indicate the shape of the SIL being elliptical.

11.2 Future Work

Whilst the developments presented in this thesis make progress towards quantum computing using NV centres, the work does highlight further investigations that can be made.

For the laser writing and diffusion of NV centres in electronic-grade diamond. Only one of the six NV centres showed an average linewidth below 100 MHz. This suggests that the laser diffusion process needs to be optimised to produce NV centres with narrower linewidths for generating entanglement with. The measured linewidths also appeared to be power broadened, indicating that narrower linewidths could be achieved at lower objective power. However, obtaining measurements at lower objective powers proved to be difficult. Another PLE characterisation procedure based on sending pulses of excitation light and stepping in frequency could be used to obtain PLE measurements at lower objective powers and to compare whether the linewidth measurement is affected by the different characterisation method.

For cavity fringe stabilisation, higher resolution characterisation of the stability on the picometer scale is needed to benchmark the fringe stabilisation stability with the other cavity locking methods. This could be achieved using higher resolution optical spectroscopy or by using a narrow tunable laser to measure the linewidth of the cavity. To improve the fringe stabilisation performance, implementing a higher resolution camera would improve the fringe imaging, so smaller fringe movements and cavity length movements can be detected and corrected for. To improve locking speed, the use of faster microelectronics, such as Field Programmable Gate Arrays, could be implemented.

For the aberration study on microcavities, further experiments could be performed to support the results of the aberration modelling. For the modelling of the spherical aberrations in Fabry-Pérot microcavities, the same experiment could be repeated with coupling to higher NA cavity modes to see if spherical aberration increases. The aberration correction measurement could also be applied to the emission through the concave mirror side of the hemispherical microcavity to see if the transmission through the planar/concave side of the cavity has a different effect on the measurement. Using a Spatial Light Modulator instead of a Deformable Mirror would

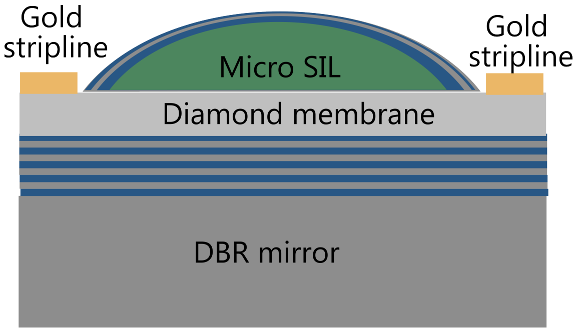

Figure 61: Schematic of a hybrid cavity. This cavity consists of a diamond membrane with laser-written NV centres being placed on a planar DBR mirror, a micro-SIL with a DBR coating to form the cavity and gold striplines to address spin control and Stark shifting of the NV ZPL.

enable the correction of more complex aberrations for studying aberrations in higher-order cavity modes.

For the aberration study on SILs, more experimental measurements were required to validate the SIL aberration model. The use of stick-on SILs would provide a way to control the position of the SIL relative to the emitter, allowing for a comparison of more scenarios with the aberration model. Another comparison could be made with results from ray tracing software such as OpticStudio. The effects of shape error and surface roughness could also be investigated using OpticStudio. The aberration model can be further improved by incorporating the effects of polarisation using Jones matrices, which affects the intensity distribution of the refocussed spot.

The aberration models presented in this thesis have been for photonic devices with simple geometry. Modelling wavefronts for phononic devices with more complex geometry can be achieved using ray tracing software such as OpticSudio and the wavefronts can be fitted to Zernike polynomials to analyse the aberrations associated.

An alternative approach for developing a cavity-coupled NV centre device for quantum computing is to develop a hybrid cavity structure as shown in Figure 61. One of the advantages of using this approach is the modular process of building this cavity. The DBR mirror, diamond membrane and the micro-SIL can be prepared independently and combined together rather than being sequential. Another advantage is that there will be no freestanding components to introduce any drift and cavity detuning. The main uncertainties would be the low temperature adhesion of the micro-SIL at low temperatures and the ability to tune the cavity length.

12 References

References

[1] *Press Kit: Moore's Law - Newsroom*. URL: `https://newsroom.intel.com/press-kit/moores-law`.

[2] David P. DiVincenzo and IBM. "The Physical Implementation of Quantum Computation". In: *Fortschritte der Physik* 48.9-11 (Feb. 2000), pp. 771–783. ISSN: 00158208. DOI: `10.1002/1521-3978(200009)48:9/11<771::AID-PROP771>3.0.CO;2-E`. URL: `https://onlinelibrary.wiley.com/doi/10.1002/1521-3978(200009)48:9/11%3C771::AID-PROP771%3E3.0.CO;2-E`.

[3] Peter W. Shor. "Polynomial-Time Algorithms for Prime Factorization and Discrete Logarithms on a Quantum Computer". In: *SIAM Journal on Computing* 26.5 (Oct. 1997), pp. 1484–1509. ISSN: 0097-5397. DOI: `10.1137/S0097539795293172`. URL: `http://dx.doi.org/10.1137/S0097539795293172`.

[4] D. Deutsch and R. Jozsa. "Rapid Solution of Problems by Quantum Computation". In: *Proceedings of the Royal Society A: Mathematical, Physical and Engineering Sciences* 439.1907 (Dec. 1992), pp. 553–558. ISSN: 1364-5021. DOI: `10.1098/rspa.1992.0167`. URL: `http://rspa.royalsocietypublishing.org/cgi/doi/10.1098/rspa.1992.0167`.

[5] Kishor Datta Gupta et al. "Utilizing Computational Complexity to Protect Cryptocurrency against Quantum Threats: A Review". In: *IT Professional* 23.5 (2021), pp. 50–55. ISSN: 1941045X. DOI: `10.1109/MITP.2021.3089494`.

[6] M C Smith et al. "Single-qubit gates with errors at the 10 7 level". In: (2025).

[7] M. Veldhorst et al. "An addressable quantum dot qubit with fault-tolerant control-fidelity". In: *Nature Nanotechnology 2014 9:12* 9.12 (Oct. 2014), pp. 981–985. ISSN: 1748-3395. DOI: `10.1038/nnano.2014.216`. URL: `https://www.nature.com/articles/nnano.2014.216`.

[8] Mohammad Mirhosseini et al. "Superconducting qubit to optical photon transduction". In: *Nature* 588.7839 (Dec. 2020), pp. 599–603. ISSN: 0028-0836. DOI: `10.1038/s41586-020-3038-6`. URL: `https://www.nature.com/articles/s41586-020-3038-6`.

[9] Nick Grimm et al. "Coherent Control of a Long-Lived Nuclear Memory Spin in a Germanium-Vacancy Multi-Qubit Node". In: *Physical Review Letters* 134.4 (Jan. 2025), p. 043603. ISSN: 10797114. DOI: `10.1103/PHYSREVLETT.134.043603/CONTROL{\_}LONG-LIVED{\_}NUCLEAR{\_}MEMORY{\_}SPIN{\_}GEV{\_}PUB.PDF`. URL: `https://journals.aps.org/prl/abstract/10.1103/PhysRevLett.134.043603`.

[10] D. S. Levonian et al. "Optical Entanglement of Distinguishable Quantum Emitters". In: *Physical Review Letters* 128.21 (May 2022). ISSN: 10797114. DOI: `10.1103/PhysRevLett.128.213602`.

[11] Romain Debroux et al. "Quantum Control of the Tin-Vacancy Spin Qubit in Diamond". In: *Physical Review X* 11.4 (Dec. 2021), p. 041041. ISSN: 21603308. DOI: `10.1103/PHYSREVX.11.041041/DEBROUX{\_}SI.PDF`. URL: `https://journals.aps.org/prx/abstract/10.1103/PhysRevX.11.041041`.

[12] Peng Wang et al. "Transform-Limited Photon Emission from a Lead-Vacancy Center in Diamond above 10 K". In: *Physical Review Letters* 132.7 (Feb. 2024), p. 073601. ISSN: 10797114. DOI: `10.1103/PHYSREVLETT.132.073601/SUPPLEMENTARY{\_}AFTER{\_}ACCEPTANCE.PDF`. URL: `https://journals.aps.org/prl/abstract/10.1103/PhysRevLett.132.073601`.

[13] J R Weber et al. "Quantum computing with defects." In: *Proceedings of the National Academy of Sciences of the United States of America* 107.19 (May 2010), pp. 8513–8. ISSN: 1091-6490. DOI: 10.1073/pnas.1003052107. URL: http://www.ncbi.nlm.nih.gov/pubmed/20404195%20http://www.pubmedcentral.nih.gov/articlerender.fcgi?artid=PMC2889300.

[14] S.C. Benjamin, B.W. Lovett, and J.M. Smith. "Prospects for measurement-based quantum computing with solid state spins". In: *Laser & Photonics Reviews* 3.6 (Nov. 2009), pp. 556–574. DOI: 10.1002/lpor.200810051. URL: https://onlinelibrary.wiley.com/doi/10.1002/lpor.200810051.

[15] Xiaobo Zhu et al. "Coherent coupling of a superconducting flux qubit to an electron spin ensemble in diamond". In: *Nature* 478.7368 (Oct. 2011), pp. 221–224. ISSN: 0028-0836. DOI: 10.1038/nature10462. URL: http://www.nature.com/doifinder/10.1038/nature10462.

[16] Peng Bo Li et al. "Hybrid Quantum Device with Nitrogen-Vacancy Centers in Diamond Coupled to Carbon Nanotubes". In: *Physical Review Letters* 117.1 (2016). ISSN: 10797114. DOI: 10.1103/PhysRevLett.117.015502.

[17] H. Bernien et al. "Heralded entanglement between solid-state qubits separated by three metres". In: *Nature* 497.7447 (May 2013), pp. 86–90. DOI: 10.1038/nature12016. URL: https://www.nature.com/articles/nature12016.

[18] B. Hensen et al. "Loophole-free Bell inequality violation using electron spins separated by 1.3 kilometres". In: *Nature* 526.7575 (Oct. 2015), pp. 682–686. ISSN: 0028-0836. DOI: 10.1038/nature15759. URL: http://www.nature.com/articles/nature15759.

[19] A J Stolk et al. "Metropolitan-scale heralded entanglement of solid-state qubits". In: (2024).

[20] M. V. Gurudev Dutt et al. "Quantum register based on individual electronic and nuclear spin qubits in diamond". In: *Science* 316.5829 (June 2007), pp. 1312–1316. ISSN:

00368075. DOI: 10.1126/SCIENCE.1139831/SUPPL{_}FILE/DUTT.SOM.PDF. URL: https://www.science.org/doi/10.1126/science.1139831%20http://www.sciencemag.org/cgi/doi/10.1126/science.1139831.

[21] T. Van Der Sar et al. "Decoherence-protected quantum gates for a hybrid solid-state spin register". In: *Nature 2012 484:7392* 484.7392 (Apr. 2012), pp. 82–86. ISSN: 1476-4687. DOI: 10.1038/nature10900. URL: https://www.nature.com/articles/nature10900.

[22] C. E. Bradley et al. "A Ten-Qubit Solid-State Spin Register with Quantum Memory up to One Minute". In: *Physical Review X* 9.3 (May 2019). ISSN: 21603308. DOI: 10.1103/PhysRevX.9.031045. URL: http://arxiv.org/abs/1905.02094.

[23] Kae Nemoto et al. "Photonic Architecture for Scalable Quantum Information Processing in Diamond". In: *Physical Review X* 4.3 (Aug. 2014), p. 031022. ISSN: 2160-3308. DOI: 10.1103/PhysRevX.4.031022. URL: https://link.aps.org/doi/10.1103/PhysRevX.4.031022.

[24] Sam Johnson, Philip R. Dolan, and Jason M. Smith. "Diamond photonics for distributed quantum networks". In: *Progress in Quantum Electronics* 55 (Sept. 2017), pp. 129–165. ISSN: 0079-6727. DOI: 10.1016/J.PQUANTELEC.2017.05.003. URL: https://www.sciencedirect.com/science/article/pii/S0079672717300162.

[25] Earl T. Campbell and Simon C. Benjamin. "Measurement-Based Entanglement under Conditions of Extreme Photon Loss". In: *Physical Review Letters* 101.13 (Sept. 2008), p. 130502. ISSN: 0031-9007. DOI: 10.1103/PhysRevLett.101.130502. URL: https://link.aps.org/doi/10.1103/PhysRevLett.101.130502.

[26] Naomi H. Nickerson, Joseph F. Fitzsimons, and Simon C. Benjamin. "Freely Scalable Quantum Technologies using Cells of 5-to-50 Qubits with Very Lossy and Noisy Photonic Links". In: (June 2014). DOI: 10.1103/PhysRevX.4.041041. URL: http://arxiv.org/abs/1406.0880%20http://dx.doi.org/10.1103/PhysRevX.4.041041.

[27] Julia Michl et al. "Perfect alignment and preferential orientation of nitrogen-vacancy centers during chemical vapor deposition diamond growth on (111) surfaces". In: *Applied Physics Letters* 104.10 (Mar. 2014), p. 102407. ISSN: 0003-6951. DOI: `10.1063/1.4868128`. URL: `http://aip.scitation.org/doi/10.1063/1.4868128`.

[28] Jonathan D. Breeze et al. "Continuous-wave room-temperature diamond maser". In: *Nature* 555.7697 (Mar. 2018), pp. 493–496. ISSN: 0028-0836. DOI: `10.1038/nature25970`. URL: `http://www.nature.com/articles/nature25970`.

[29] Daiki Misonou et al. "Construction and operation of a tabletop system for nanoscale magnetometry with single nitrogen-vacancy centers in diamond". In: *AIP Advances* 10.2 (Feb. 2020). ISSN: 21583226. DOI: `10.1063/1.5128716`.

[30] Marcus W. Doherty et al. "The nitrogen-vacancy colour centre in diamond". In: *Physics Reports* 528.1 (July 2013), pp. 1–45. ISSN: 03701573. DOI: `10.1016/j.physrep.2013.02.001`. URL: `https://www.sciencedirect.com/science/article/abs/pii/S0370157313000562?via%3Dihub%20https://linkinghub.elsevier.com/retrieve/pii/S0370157313000562`.

[31] Gopalakrishnan Balasubramanian et al. "Ultralong spin coherence time in isotopically engineered diamond". In: *Nature Materials* 8.5 (May 2009), pp. 383–387. ISSN: 1476-1122. DOI: `10.1038/nmat2420`. URL: `http://www.nature.com/articles/nmat2420`.

[32] Mark Fox. *Quantum Optics : An Introduction*. Oxford, UNITED KINGDOM: Oxford University Press USA - OSO, 2006. ISBN: 9780191524257.

[33] Albert Liu et al. "Spectral Broadening and Ultrafast Dynamics of a Nitrogen-Vacancy Center Ensemble in Diamond". In: *Materials for Quantum Technology* 1.2 (May 2020), pp. 1–7. ISSN: 2633-4356. DOI: `10.1088/2633-4356/ABF330`. URL: `http://arxiv.org/abs/2011.00153%20https://iopscience.iop.org/article/10.1088/2633-4356/abf330`.

[34] Tesfaye A Abtew et al. “Dynamic Jahn-Teller Effect in the NV À Center in Diamond”. In: (2011). DOI: `10.1103/PhysRevLett.107.146403`.

[35] Kai Mei C. Fu et al. “Observation of the dynamic Jahn-Teller effect in the excited states of nitrogen-vacancy centers in diamond”. In: *Physical Review Letters* 103.25 (Dec. 2009), p. 256404. ISSN: 00319007. DOI: `10.1103/PHYSREVLETT.103.256404/FIGURES/4/MEDIUM`. URL: `https://journals.aps.org/prl/abstract/10.1103/PhysRevLett.103.256404`.

[36] Taras Plakhotnik, Marcus W Doherty, and Neil B Manson. “Electron-phonon processes of the nitrogen-vacancy center in diamond”. In: *RAPID COMMUNICATIONS PHYSICAL REVIEW B* 92 (2015), p. 81203. DOI: `10.1103/PhysRevB.92.081203`.

[37] A. Batalov et al. “Low Temperature Studies of the Excited-State Structure of Negatively Charged Nitrogen-Vacancy Color Centers in Diamond”. In: *Physical Review Letters* 102.19 (May 2009), pp. 1–4. ISSN: 00319007. DOI: `10.1103/PhysRevLett.102.195506`. URL: `https://journals.aps.org/prl/abstract/10.1103/PhysRevLett.102.195506`.

[38] Ph Tamarat et al. “Spin-flip and spin-conserving optical transitions of the nitrogen-vacancy centre in diamond”. In: *New Journal of Physics* 10.4 (Apr. 2008), p. 045004. ISSN: 1367-2630. DOI: `10.1088/1367-2630/10/4/045004`. URL: `https://iopscience.iop.org/article/10.1088/1367-2630/10/4/045004`.

[39] Sean D. Barrett and Pieter Kok. “Efficient high-fidelity quantum computation using matter qubits and linear optics”. In: (Aug. 2004). DOI: `10.1103/PhysRevA.71.060310`. URL: `http://arxiv.org/abs/quant-ph/0408040%20http://dx.doi.org/10.1103/PhysRevA.71.060310`.

[40] Ph Tamarat et al. “Stark Shift Control of Single Optical Centers in Diamond”. In: *Physical Review Letters* 97.8 (Aug. 2006), p. 083002. ISSN: 0031-9007. DOI: `10.`

1103/PhysRevLett.97.083002. URL: https://link.aps.org/doi/10.1103/PhysRevLett.97.083002.

[41] Arian Stolk et al. "Telecom-band quantum interference of frequency-converted photons from remote detuned NV centers". In: *PRX Quantum* 3.2 (Jan. 2022), p. 020359. ISSN: 26913399. DOI: 10.1103/PRXQuantum.3.020359. URL: https://journals.aps.org/prxquantum/abstract/10.1103/PRXQuantum.3.020359%20http://arxiv.org/abs/2202.00036%20http://dx.doi.org/10.1103/PRXQuantum.3.020359.

[42] Marc Warner et al. "Potential for spin-based information processing in a thin-film molecular semiconductor". In: *Nature* 503.7477 (Oct. 2013), pp. 504–508. ISSN: 0028-0836. DOI: 10.1038/nature12597. URL: http://www.nature.com/doifinder/10.1038/nature12597.

[43] N. Aslam et al. "Photo-induced ionization dynamics of the nitrogen vacancy defect in diamond investigated by single-shot charge state detection". In: *New Journal of Physics* 15 (2013). ISSN: 13672630. DOI: 10.1088/1367-2630/15/1/013064.

[44] Igor Aharonovich and Elke Neu. "Diamond Nanophotonics". In: *Advanced Optical Materials* 2.10 (Oct. 2014), pp. 911–928. ISSN: 21951071. DOI: 10.1002/adom.201400189. URL: http://doi.wiley.com/10.1002/adom.201400189.

[45] A. Sipahigil et al. "Indistinguishable photons from separated silicon-vacancy centers in diamond". In: *Physical Review Letters* 113.11 (Sept. 2014), p. 113602. ISSN: 10797114. DOI: 10.1103/PHYSREVLETT.113.113602/SUPPLEMENTAL{_}MATERIALS.PDF. URL: https://journals.aps.org/prl/abstract/10.1103/PhysRevLett.113.113602.

[46] Kay D. Jahnke et al. "Electron–phonon processes of the silicon-vacancy centre in diamond". In: *New Journal of Physics* 17.4 (Apr. 2015), p. 043011. ISSN: 1367-2630. DOI: 10.1088/1367-2630/17/4/043011. URL: https://iopscience.iop.org/article/10.1088/1367-2630/17/4/043011%20https://iopscience.iop.org/article/10.1088/1367-2630/17/4/043011/meta.

[47] Jonas N. Becker et al. "All-Optical Control of the Silicon-Vacancy Spin in Diamond at Millikelvin Temperatures". In: *Physical Review Letters* 120.5 (Jan. 2018), p. 053603. ISSN: 10797114. DOI: `10.1103/PHYSREVLETT.120.053603/SUPPLEMENT{\_}BECKER{\_}ET{\_}AL{\_}FINAL{\_}SUBMISSION.PDF`. URL: `https://journals.aps.org/prl/abstract/10.1103/PhysRevLett.120.053603`.

[48] Young Ik Sohn et al. "Controlling the coherence of a diamond spin qubit through its strain environment". In: *Nature Communications 2018 9:1* 9.1 (May 2018), pp. 1–6. ISSN: 2041-1723. DOI: `10.1038/s41467-018-04340-3`. URL: `https://www.nature.com/articles/s41467-018-04340-3`.

[49] Xinghan Guo et al. "Microwave-Based Quantum Control and Coherence Protection of Tin-Vacancy Spin Qubits in a Strain-Tuned Diamond-Membrane Heterostructure". In: *Physical Review X* 13 (2023). DOI: `10.1103/PhysRevX.13.041037`.

[50] Suzanne B. Van Dam, Maximilian T. Ruf, and Ronald Hanson. "Optimal design of diamond-air microcavities for quantum networks using an analytical approach". In: *New Journal of Physics* 20.11 (June 2018), p. 115004. ISSN: 1367-2630. DOI: `10.1088/1367-2630/aaec29`. URL: `https://iopscience.iop.org/article/10.1088/1367-2630/aaec29/meta`.

[51] Julia Heupel et al. "Fabrication of High-Quality Thin Single-Crystal Diamond Membranes with Low Surface Roughness". In: *physica status solidi (a)* 220.4 (Feb. 2023), p. 2200465. ISSN: 1862-6300. DOI: `10.1002/pssa.202200465`. URL: `https://onlinelibrary.wiley.com/doi/10.1002/pssa.202200465`.

[52] I. Bayn et al. "Diamond processing by focused ion beam-surface damage and recovery". In: *Applied Physics Letters* 99.18 (Oct. 2011). ISSN: 00036951. DOI: `10.1063/1.3658631/341188`. URL: `/aip/apl/article/99/18/183109/341188/Diamond-processing-by-focused-ion-beam-surface`.

[53] P. C. Maurer et al. "Room-Temperature Quantum Bit Memory Exceeding One Second". In: *Science* 336.6086 (June 2012), pp. 1283–1286. ISSN: 0036-8075. DOI: `10.1126/science.1220513`. URL: `http://www.sciencemag.org/cgi/doi/10.1126/science.1220513`.

[54] G. D. Fuchs et al. "A quantum memory intrinsic to single nitrogen–vacancy centres in diamond". In: *Nature Physics* 7.10 (June 2011), pp. 789–793. ISSN: 1745-2473. DOI: `10.1038/nphys2026`. URL: `http://www.nature.com/doifinder/10.1038/nphys2026`.

[55] T. D. Ladd et al. "Coherence time of decoupled nuclear spins in silicon". In: *Physical Review B* 71.1 (Jan. 2005), p. 014401. ISSN: 1098-0121. DOI: `10.1103/PhysRevB.71.014401`. URL: `https://link.aps.org/doi/10.1103/PhysRevB.71.014401`.

[56] Ariful Haque et al. "An Overview on the Formation and Processing of Nitrogen-Vacancy Photonic Centers in Diamond by Ion Implantation". In: *Journal of Manufacturing and Materials Processing* 1.1 (Aug. 2017), p. 6. ISSN: 2504-4494. DOI: `10.3390/jmmp1010006`. URL: `http://www.mdpi.com/2504-4494/1/1/6`.

[57] Maximilian Ruf et al. "Optically Coherent Nitrogen-Vacancy Centers in Micrometer-Thin Etched Diamond Membranes". In: *Nano Letters* 19.6 (June 2019), pp. 3987–3992. ISSN: 1530-6984. DOI: `10.1021/acs.nanolett.9b01316`. URL: `https://pubs.acs.org/doi/10.1021/acs.nanolett.9b01316`.

[58] Yu-Chen Chen et al. "Laser writing of coherent colour centres in diamond". In: *Nature Photonics* 11.2 (Feb. 2017), pp. 77–80. ISSN: 1749-4885. DOI: `10.1038/nphoton.2016.234`. URL: `http://www.nature.com/articles/nphoton.2016.234`.

[59] Yu-Chen Chen et al. "Laser writing of individual nitrogen-vacancy defects in diamond with near-unity yield". In: *Optica* 6.5 (July 2019), p. 662. ISSN: 23342536. DOI: `10.1364/optica.6.000662`. URL: `http://arxiv.org/abs/1807.04028%20http://dx.doi.org/10.1364/OPTICA.6.000662`.

[60] Kenichi Ohno et al. "Engineering shallow spins in diamond with nitrogen delta-doping". In: *Applied Physics Letters* 101.8 (Aug. 2012), p. 82413. ISSN: 00036951. DOI: `10.1063/1.4748280/112025`. URL: `/aip/apl/article/101/8/082413/112025/Engineering-shallow-spins-in-diamond-with-nitrogen`.

[61] Y. Chu et al. "Coherent optical transitions in implanted nitrogen vacancy centers". In: *Nano Letters* 14.4 (Apr. 2014), pp. 1982–1986. ISSN: 15306992. DOI: `10.1021/NL404836P/ASSET/IMAGES/LARGE/NL-2013-04836P{\_}0003.JPEG`. URL: `https://pubs.acs.org/doi/full/10.1021/nl404836p`.

[62] Daniel Riedel et al. "Deterministic enhancement of coherent photon generation from a nitrogen-vacancy center in ultrapure diamond". In: *Physical Review X* 7.3 (Sept. 2017), p. 031040. ISSN: 21603308. DOI: `10.1103/PhysRevX.7.031040`. URL: `https://link.aps.org/doi/10.1103/PhysRevX.7.031040`.

[63] Suzanne B. van Dam et al. "Optical coherence of diamond nitrogen-vacancy centers formed by ion implantation and annealing". In: (Dec. 2018). DOI: `10.1103/PhysRevB.99.161203`. URL: `http://arxiv.org/abs/1812.11523%20http://dx.doi.org/10.1103/PhysRevB.99.161203`.

[64] Z. Huang et al. "Diamond nitrogen-vacancy centers created by scanning focused helium ion beam and annealing". In: *Applied Physics Letters* 103.8 (Aug. 2013). ISSN: 00036951. DOI: `10.1063/1.4819339/130933`. URL: `/aip/apl/article/103/8/081906/130933/Diamond-nitrogen-vacancy-centers-created-by`.

[65] Sébastien Pezzagna et al. "Nanoscale Engineering and Optical Addressing of Single Spins in Diamond". In: *Small* 6.19 (Oct. 2010), pp. 2117–2121. ISSN: 1613-6829. DOI: `10.1002/SMLL.201000902`. URL: `https://onlinelibrary.wiley.com/doi/full/10.1002/smll.201000902`.

[66] B Campbell and A Mainwood. "Radiation Damage of Diamond by Electron and Gamma Irradiation". In: *physica status solidi (a)* 181.1 (Sept. 2000), pp. 99–107. ISSN: 0031-

8965. DOI: https://doi.org/10.1002/1521-396X(200009)181:1<99::AID-PSSA99>3.0.CO;2-5. URL: https://onlinelibrary.wiley.com/doi/epdf/10.1002/1521-396X%28200009%29181%3A1%3C99%3A%3AAID-PSSA99%3E3.0.CO%3B2-5.

[67] Claire A. McLellan et al. "Patterned Formation of Highly Coherent Nitrogen-Vacancy Centers Using a Focused Electron Irradiation Technique". In: *Nano Letters* 16.4 (Apr. 2016), pp. 2450–2454. ISSN: 15306992. DOI: 10.1021/ACS.NANOLETT.5B05304/SUPPL{_}FILE/NL5B05304{_}SI{_}001.PDF. URL: https://pubs.acs.org/doi/full/10.1021/acs.nanolett.5b05304.

[68] Sébastien Pezzagna et al. "Creation and nature of optical centres in diamond for single-photon emission—overview and critical remarks". In: *New Journal of Physics* 13.3 (Mar. 2011), p. 035024. ISSN: 1367-2630. DOI: 10.1088/1367-2630/13/3/035024. URL: http://stacks.iop.org/1367-2630/13/i=3/a=035024?key=crossref.ba013f6c45f5337170d778550b58b9c0.

[69] Viktoria Yurgens et al. "Low-Charge-Noise Nitrogen-Vacancy Centers in Diamond Created Using Laser Writing with a Solid-Immersion Lens". In: *ACS Photonics* 8.6 (June 2021), pp. 1726–1734. ISSN: 2330-4022. DOI: 10.1021/acsphotonics.1c00274. URL: https://doi.org/10.1021/acsphotonics.1c00274%20https://pubs.acs.org/doi/10.1021/acsphotonics.1c00274.

[70] Anchita Addhya et al. "Photonic-Cavity-Enhanced Laser Writing of Color Centers in Diamond". In: *Nano Letters* (2024). ISSN: 15306992. DOI: 10.1021/acs.nanolett.4c02639.

[71] Kerry J. Vahala. "Optical microcavities". In: *2005 European Quantum Electronics Conference, EQEC '05*. Vol. 424. 6950. Aug. 2003, p. 352. ISBN: 0780389735. DOI: 10.1109/EQEC.2005.1567517. URL: http://www.nature.com/articles/nature01939.

[72] S Johnson et al. "Tunable cavity coupling of the zero phonon line of a nitrogen-vacancy defect in diamond". In: *New Journal of Physics* 17.12 (Dec. 2015), p. 122003. ISSN: 1367-2630. DOI: 10.1088/1367-2630/17/12/122003. URL: http://stacks.iop.org/1367-2630/17/i=12/a=122003?key=crossref.eb189333211e426b97a29b65684d0b7b.

[73] Andrei Faraon et al. "Coupling of Nitrogen-Vacancy Centers to Photonic Crystal Cavities in Monocrystalline Diamond". In: *Physical Review Letters* 109.3 (July 2012), p. 033604. ISSN: 0031-9007. DOI: 10.1103/PhysRevLett.109.033604. URL: https://link.aps.org/doi/10.1103/PhysRevLett.109.033604.

[74] Luozhou Li et al. "Efficient photon collection from a nitrogen vacancy center in a circular bullseye grating". In: *Nano Letters* 15.3 (Mar. 2015), pp. 1493–1497. ISSN: 15306992. DOI: 10.1021/NL503451J/SUPPL{_}FILE/NL503451J{_}SI{_}001.PDF. URL: https://pubs.acs.org/doi/full/10.1021/nl503451j.

[75] Stefan Schietinger and Oliver Benson. "Coupling single NV-centres to high-Q whispering gallery modes of a preselected frequency-matched microresonator". In: *Journal of Physics B: Atomic, Molecular and Optical Physics* 42.11 (May 2009), p. 114001. ISSN: 0953-4075. DOI: 10.1088/0953-4075/42/11/114001. URL: https://iopscience.iop.org/article/10.1088/0953-4075/42/11/114001%20https://iopscience.iop.org/article/10.1088/0953-4075/42/11/114001/meta.

[76] Andrei Faraon et al. "Resonant enhancement of the zero-phonon emission from a colour centre in a diamond cavity". In: *Nature Photonics* 5.5 (May 2011), pp. 301–305. ISSN: 1749-4885. DOI: 10.1038/nphoton.2011.52. URL: http://www.nature.com/articles/nphoton.2011.52.

[77] Khodadad N Dinyari et al. "Mechanical tuning of whispering gallery modes over a 05 THz tuning range with MHz resolution in a silica microsphere at cryogenic temperatures". In: *Optics Express* 19.19 (Sept. 2011), p. 17966. ISSN: 1094-4087. DOI: 10.1364/OE.19.017966. URL: https://opg.optica.org/oe/abstract.cfm?uri=oe-19-19-17966.

[78] S. Mosor et al. "Scanning a photonic crystal slab nanocavity by condensation of xenon". In: *Applied Physics Letters* 87.14 (Oct. 2005), pp. 1–3. ISSN: 0003-6951. DOI: 10.1063/1.2076435. URL: /aip/apl/article/87/14/141105/117362/Scanning-a-photonic-crystal-slab-nanocavity-by%20http://aip.scitation.org/doi/10.1063/1.2076435.

[79] Jingyuan Linda Zhang et al. "Strongly Cavity-Enhanced Spontaneous Emission from Silicon-Vacancy Centers in Diamond". In: *Nano Letters* 18.2 (Feb. 2018), pp. 1360–1365. ISSN: 15306992. DOI: 10.1021/ACS.NANOLETT.7B05075/ASSET/IMAGES/LARGE/NL-2017-05075R{_}0004.JPEG. URL: https://pubs.acs.org/doi/full/10.1021/acs.nanolett.7b05075.

[80] Erika Janitz et al. "Cavity quantum electrodynamics with color centers in diamond". In: *Optica, Vol. 7, Issue 10, pp. 1232-1252* 7.10 (Oct. 2020), pp. 1232–1252. ISSN: 2334-2536. DOI: 10.1364/OPTICA.398628. URL: https://opg.optica.org/viewmedia.cfm?uri=optica-7-10-1232&seq=0&html=true%20https://opg.optica.org/abstract.cfm?uri=optica-7-10-1232%20https://opg.optica.org/optica/abstract.cfm?uri=optica-7-10-1232.

[81] Maximilian Ruf et al. "Quantum networks based on color centers in diamond". In: *Journal of Applied Physics* 130.7 (Aug. 2021), p. 70901. ISSN: 10897550. DOI: 10.1063/5.0056534/1061464. URL: /aip/jap/article/130/7/070901/1061464/Quantum-networks-based-on-color-centers-in-diamond.

[82] Aurélien A. P. Trichet et al. "Topographic control of open-access microcavities at the nanometer scale". In: *Optics Express* 23.13 (2015), p. 17205. ISSN: 1094-4087. DOI: 10.1364/oe.23.017205.

[83] D Hunger et al. "A fiber Fabry–Perot cavity with high finesse". In: *New Journal of Physics* 12.6 (June 2010), p. 065038. ISSN: 1367-2630. DOI: 10.1088/1367-2630/

12/6/065038. URL: http://stacks.iop.org/1367-2630/12/i=6/a=065038?key=crossref.e6ea72b3da2564be9138384f611286d0.

[84] Sigurd Flågan et al. “A diamond-confined open microcavity featuring a high quality-factor and a small mode-volume”. In: *Journal of Applied Physics* 131.11 (Mar. 2022), p. 113102. ISSN: 10897550. DOI: 10.1063/5.0081577/2836604. URL: /aip/jap/article/131/11/113102/2836604/A-diamond-confined-open-microcavity-featuring-a.

[85] Yiliang Bao et al. “Concave silicon micromirrors for stable hemispherical optical microcavities”. In: *Optics Express* 25.13 (June 2017), p. 15493. ISSN: 1094-4087. DOI: 10.1364/OE.25.015493. URL: https://opg.optica.org/abstract.cfm?URI=oe-25-13-15493.

[86] Jannis Hessenauer et al. “Laser written mirror profiles for open-access fiber Fabry-Perot microcavities”. In: *Optics Express, Vol. 31, Issue 11, pp. 17380-17388* 31.11 (May 2023), pp. 17380–17388. ISSN: 1094-4087. DOI: 10.1364/OE.481685. URL: https://opg.optica.org/viewmedia.cfm?uri=oe-31-11-17380&seq=0&html=true%20https://opg.optica.org/abstract.cfm?uri=oe-31-11-17380%20https://opg.optica.org/oe/abstract.cfm?uri=oe-31-11-17380.

[87] Christina J. Hood, H. J. Kimble, and Jun Ye. “Characterization of high-finesse mirrors: Loss, phase shifts, and mode structure in an optical cavity”. In: *Physical Review A* 64.3 (Aug. 2001), p. 033804. DOI: 10.1103/PhysRevA.64.033804. URL: https://link.aps.org/doi/10.1103/PhysRevA.64.033804.

[88] Hanno Kaupp et al. “Purcell-Enhanced Single-Photon Emission from Nitrogen-Vacancy Centers Coupled to a Tunable Microcavity”. In: *Physical Review Applied* 6.5 (Nov. 2016), p. 054010. ISSN: 2331-7019. DOI: 10.1103/PhysRevApplied.6.054010. URL: https://link.aps.org/doi/10.1103/PhysRevApplied.6.054010.

[89] Maximilian Ruf et al. "Optically coherent nitrogen-vacancy centers in μm-thin etched diamond membranes - Supplementary information". In: *arXiv* 19.6 (2019), pp. 1–11. ISSN: 23318422.

[90] T. Legero et al. "Time-resolved two-photon quantum interference". In: *Applied Physics B: Lasers and Optics* 77.8 (2003), pp. 797–802. ISSN: 09462171. DOI: `10.1007/s00340-003-1337-x`.

[91] Xinghan Guo et al. "Tunable and Transferable Diamond Membranes for Integrated Quantum Technologies". In: *Nano Letters* 21.24 (Dec. 2021), pp. 10392–10399. ISSN: 1530-6984. DOI: `10.1021/acs.nanolett.1c03703`. URL: `https://pubs.acs.org/doi/10.1021/acs.nanolett.1c03703%20https://doi.org/10.1021/acs.nanolett.1c03703`.

[92] Stefan Bogdanović et al. "Design and low-temperature characterization of a tunable microcavity for diamond-based quantum networks". In: *Applied Physics Letters* 110.17 (Dec. 2017). ISSN: 00036951. DOI: `10.1063/1.4982168`. URL: `http://arxiv.org/abs/1612.02164%20http://dx.doi.org/10.1063/1.4982168`.

[93] Yanik Herrmann et al. "A low-temperature tunable microcavity featuring high passive stability and microwave integration". In: *AVS Quantum Science* 6.4 (Dec. 2024), p. 27. ISSN: 26390213. DOI: `10.1116/5.0233296/3325344`. URL: `/avs/aqs/article/6/4/041401/3325344/A-low-temperature-tunable-microcavity-featuring`.

[94] E. Janitz et al. "A High-Mechanical Bandwidth Fabry-Perot Fiber Cavity". In: (June 2017). DOI: `10.1364/OE.25.020932`. URL: `http://arxiv.org/abs/1706.09843%20http://dx.doi.org/10.1364/OE.25.020932`.

[95] M. Fisicaro et al. "Active stabilization of an open-access optical microcavity for low-noise operation in a standard closed-cycle cryostat". In: *Review of Scientific Instruments* 95.3 (Mar. 2024). ISSN: 10897623. DOI: `10.1063/5.0174982`. URL: `/aip/rsi/article/95/3/033101/3268097/Active-stabilization-of-an-open-access-optical`.

[96] Thibaud Ruelle et al. "A tunable fiber Fabry-Perot cavity for hybrid optomechanics stabilized at 4 K". In: *Review of Scientific Instruments* 93.9 (Sept. 2022), p. 95003. ISSN: 10897623. DOI: `10.1063/5.0098140/2849410`. URL: `/aip/rsi/article/93/9/095003/2849410/A-tunable-fiber-Fabry-Perot-cavity-for-hybrid`.

[97] Meryem Benelajla et al. "Physical Origins of Extreme Cross-Polarization Extinction in Confocal Microscopy". In: *Physical Review X* 11.2 (Apr. 2021), p. 021007. ISSN: 2160-3308. DOI: `10.1103/PhysRevX.11.021007`. URL: `https://link.aps.org/doi/10.1103/PhysRevX.11.021007`.

[98] P. Steindl et al. "Cross-Polarization-Extinction Enhancement and Spin-Orbit Coupling of Light for Quantum-Dot Cavity Quantum Electrodynamics Spectroscopy". In: *Physical Review Applied* 19.6 (June 2023), p. 064082. ISSN: 23317019. DOI: `10.1103/PHYSREVAPPLIED.19.064082/FIGURES/6/MEDIUM`. URL: `https://journals.aps.org/prapplied/abstract/10.1103/PhysRevApplied.19.064082`.

[99] M. Ruf et al. "Resonant Excitation and Purcell Enhancement of Coherent Nitrogen-Vacancy Centers Coupled to a Fabry-Perot Microcavity". In: *Physical Review Applied* 15.2 (Feb. 2021). ISSN: 23317019. DOI: `10.1103/PHYSREVAPPLIED.15.024049`.

[100] Viktoria Yurgens et al. "Cavity-assisted resonance fluorescence from a nitrogen-vacancy center in diamond". In: *npj Quantum Information 2024 10:1* 10.1 (Nov. 2024), pp. 1–8. ISSN: 2056-6387. DOI: `10.1038/s41534-024-00915-9`. URL: `https://www.nature.com/articles/s41534-024-00915-9`.

[101] Hannes Bernien et al. "Two-Photon Quantum Interference from Separate Nitrogen Vacancy Centers in Diamond". In: *Physical Review Letters* 108.4 (Jan. 2012), p. 043604. ISSN: 0031-9007. DOI: `10.1103/PhysRevLett.108.043604`. URL: `https://link.aps.org/doi/10.1103/PhysRevLett.108.043604`.

[102] W L Barnes et al. "Solid-state single photon sources: Light collection strategies". In: *European Physical Journal D*. Vol. 18. 2. 2002, pp. 197–210. DOI: `10.1140/epjd/e20020024`.

[103] J. P. Hadden et al. "Strongly enhanced photon collection from diamond defect centers under microfabricated integrated solid immersion lenses". In: *Applied Physics Letters* 97.24 (2010). ISSN: 00036951. DOI: `10.1063/1.3519847`.

[104] L. Marseglia et al. "Nanofabricated solid immersion lenses registered to single emitters in diamond". In: *Applied Physics Letters* 98.13 (2011), pp. 10–13. ISSN: 00036951. DOI: `10.1063/1.3573870`.

[105] Sebastian Knauer, John P. Hadden, and John G. Rarity. "In-situ measurements of fabrication induced strain in diamond photonic-structures using intrinsic colour centres". In: *npj Quantum Information* 6.1 (2020), pp. 2–7. ISSN: 20566387. DOI: `10.1038/s41534-020-0277-1`. URL: `http://dx.doi.org/10.1038/s41534-020-0277-1`.

[106] P. Siyushev et al. "Monolithic diamond optics for single photon detection". In: *Applied Physics Letters* 97.24 (2010), pp. 1–4. ISSN: 00036951. DOI: `10.1063/1.3519849`.

[107] D. Riedel et al. "Low-Loss Broadband Antenna for Efficient Photon Collection from a Coherent Spin in Diamond". In: *Physical Review Applied* 2.6 (Dec. 2014), p. 064011. ISSN: 2331-7019. DOI: `10.1103/PhysRevApplied.2.064011`. URL: `https://link.aps.org/doi/10.1103/PhysRevApplied.2.064011`.

[108] Xingrui Cheng et al. "Additive GaN Solid Immersion Lenses for Enhanced Photon Extraction Efficiency from Diamond Color Centers". In: *ACS Photonics* 10.9 (2023), pp. 3374–3383. ISSN: 23304022. DOI: `10.1021/acsphotonics.3c00854`.

[109] Motoyoshi Baba et al. "Aberrations and allowances for errors in a hemisphere solid immersion lens for submicron-resolution photoluminescence microscopy". In: *Journal of Applied Physics* 85.9 (May 1999), pp. 6923–6925. ISSN: 0021-8979. DOI: `10.1063/`

1.370107. URL: https://pubs.aip.org/jap/article/85/9/6923/690650/Aberrations-and-allowances-for-errors-in-a.

[110] Matthew Lang, Eric Aspnes, and Tom D. Milster. “Geometrical analysis of third-order aberrations for a solid immersion lens”. In: *Optics Express* 16.24 (Nov. 2008), p. 20008. ISSN: 1094-4087. DOI: 10.1364/OE.16.020008. URL: https://opg.optica.org/oe/abstract.cfm?uri=oe-16-24-20008.

[111] Yang Lu et al. “Aberration compensation in aplanatic solid immersion lens microscopy”. In: *Optics Express* 21.23 (Nov. 2013), p. 28189. ISSN: 10944087. DOI: 10.1364/oe.21.028189.

[112] Geoffrey Brooker. *Modern classical optics*. eng. Oxford master series in physics. Atomic, optical, and laser physics ; 8. Oxford: Oxford Univeristy Press, July 2003. ISBN: 9780198599647 (hardback).

[113] Martin J Booth. “Adaptive Optics for Confocal Microscopy”. PhD thesis. Univeristy of Oxford, 2001.

[114] *Deformable Mirrors for Wavefront Control - Boston Micromachines Corp*. URL: https://bostonmicromachines.com/products/deformable-mirrors/standard-deformable-mirrors/.

[115] Dorian Gangloff et al. “Preventing and Reversing Vacuum-Induced Optical Losses in High-Finesse Tantalum (V) Oxide Mirror Coatings”. In: *Optics Express* 23.14 (May 2015), p. 18014. ISSN: 10944087. DOI: 10.1364/OE.23.018014. URL: http://dx.doi.org/10.1364/OE.23.018014.

[116] H. Demiryont, James R. Sites, and Kent Geib. “Effects of oxygen content on the optical properties of tantalum oxide films deposited by ion-beam sputtering”. In: *Applied Optics* 24.4 (Feb. 1985), p. 490. ISSN: 0003-6935. DOI: 10.1364/AO.24.000490. URL: https://opg.optica.org/abstract.cfm?URI=ao-24-4-490.

[117] Christian Kurtsiefer et al. “Stable Solid-State Source of Single Photons”. In: (2000).

[118] J L O'brien et al. "Observation of 1.2-GHz linewidth of zero-phonon-line in photoluminescence spectra of nitrogen vacancy centers in nanodiamonds using a Fabry-Perot interferometer". In: *Optics Express, Vol. 21, Issue 24, pp. 29679-29686* 21.24 (Dec. 2013), pp. 29679–29686. ISSN: 1094-4087. DOI: `10.1364/OE.21.029679`. URL: `https://opg.optica.org/viewmedia.cfm?uri=oe-21-24-29679&seq=0&html=true`.

[119] Matthew Newville et al. *LMFIT: Non-Linear Least-Square Minimization and Curve-Fitting for Python*. DOI: `10.5281/ZENODO.11813`. URL: `https://zenodo.org/records/11813`.

[120] Laura Orphal-Kobin et al. "Optically Coherent Nitrogen-Vacancy Defect Centers in Diamond Nanostructures". In: *Physical Review X* 13.1 (Mar. 2023), p. 011042. ISSN: 2160-3308. DOI: `10.1103/PhysRevX.13.011042`. URL: `https://link.aps.org/doi/10.1103/PhysRevX.13.011042`.

[121] Gilbert Grynberg et al. *Introduction to Quantum Optics*. Cambridge University Press, Sept. 2010, pp. 84–85. ISBN: 9780521551120. DOI: `10.1017/CBO9780511778261`. URL: `https://www.cambridge.org/core/product/identifier/9780511778261/type/book`.

[122] M. W. Doherty et al. "Theory of the ground-state spin of the NV - center in diamond". In: *Physical Review B - Condensed Matter and Materials Physics* 85.20 (May 2012). ISSN: 10980121. DOI: `10.1103/PHYSREVB.85.205203`.

[123] A. Dréau et al. "Avoiding power broadening in optically detected magnetic resonance of single NV defects for enhanced dc magnetic field sensitivity". In: *Physical Review B - Condensed Matter and Materials Physics* 84.19 (Nov. 2011), p. 195204. ISSN: 1550235X. DOI: `10.1103/PHYSREVB.84.195204/FIGURES/6/MEDIUM`. URL: `https://journals.aps.org/prb/abstract/10.1103/PhysRevB.84.195204`.

[124] Toyofumi Ishikawa et al. "Optical and spin coherence properties of nitrogen-vacancy centers placed in a 100 nm thick isotopically purified diamond layer". In: *Nano Letters* 12.4

(Apr. 2012), pp. 2083–2087. ISSN: 15306984. DOI: `10.1021/NL300350R/SUPPL{\_}FILE/NL300350R{\_}SI{\_}001.PDF`. URL: `https://pubs.acs.org/doi/full/10.1021/nl300350r`.

[125] Yushi Nishimura et al. "Wide-field fluorescent nanodiamond spin measurements toward real-time large-area intracellular thermometry". In: 11.1 (). ISSN: 2045-2322. DOI: `10.1038/s41598-021-83285-y`. URL: `https://www.nature.com/articles/s41598-021-83285-y%20https://doi.org/10.1038/s41598-021-83285-y`.

[126] Jan M. Binder et al. "Qudi: A modular python suite for experiment control and data processing". In: *SoftwareX* 6 (Jan. 2017), pp. 85–90. ISSN: 2352-7110. DOI: `10.1016/J.SOFTX.2017.02.001`.

[127] Eric D Black. "An introduction to Pound-Drever-Hall laser frequency stabilization". In: (2001). DOI: `10.1119/1.1286663`. URL: `http://scitation.aip.org/termsconditions..`

[128] Lukas Greuter et al. "A small mode volume tunable microcavity: Development and characterization". In: *Applied Physics Letters* 105.12 (Sept. 2014), p. 121105. ISSN: 00036951. DOI: `10.1063/1.4896415/1019379`. URL: `/aip/apl/article/105/12/121105/1019379/A-small-mode-volume-tunable-microcavity`.

[129] Daniel Najer et al. "A gated quantum dot strongly coupled to an optical microcavity". In: *Nature 2019 575:7784* 575.7784 (Oct. 2019), pp. 622–627. ISSN: 1476-4687. DOI: `10.1038/s41586-019-1709-y`. URL: `https://www.nature.com/articles/s41586-019-1709-y`.

[130] *Understanding ray vs wave optics with a simple example – Ansys Optics*. URL: `https://optics.ansys.com/hc/en-us/articles/360034394214-Understanding-ray-vs-wave-optics-with-a-simple-example`.

[131] Ansys®. *Lumerical*.

[132] Karen Mary Hampson et al. "Sensorless Adaptive Optics". In: (). DOI: `10.5281/ZENODO.4271425`. URL: `https://zenodo.org/records/4271425`.

[133] Matthew R. Foreman and Peter Török. "Computational methods in vectorial imaging". In: *https://doi.org/10.1080/09500340.2010.525668* 58.5-6 (Mar. 2010), pp. 339–364. ISSN: 09500340. DOI: `10.1080/09500340.2010.525668`. URL: `https://www.tandfonline.com/doi/abs/10.1080/09500340.2010.525668`.

[134] Szu Huat Goh and Colin J.R. Sheppard. "High aperture focusing through a spherical interface: Application to refractive solid immersion lens (RSIL) for subsurface imaging". In: *Optics Communications* 282.5 (Mar. 2009), pp. 1036–1041. ISSN: 00304018. DOI: `10.1016/j.optcom.2008.11.032`. URL: `https://linkinghub.elsevier.com/retrieve/pii/S0030401808011644`.